ON ACCELERATING ROAD VEHICLE AERODYNAMICS

by

Brett Peters

A dissertation submitted to the faculty of
The University of North Carolina at Charlotte
in partial fulfillment of the requirements
for the degree of Doctor of Philosophy in
Mechanical Engineering

Charlotte

2018

Approved by:

Mesbah Uddin

Maciej Noras

Donald Jacobs

Stuart Smith

Peter Tkacik

ABSTRACT

BRETT PETERS. On Accelerating Road Vehicle Aerodynamics. (Under the direction of MESBAH UDDIN)

Road vehicle aerodynamics are primarily focused on developing and modeling performance at steady-state conditions, although this does not fully encompass the entire operating envelope. Considerable vehicle acceleration and deceleration occurs during operation, either because of driver input or from transient weather phenomenon such as wind gusting. With this considered, high performance road vehicles experience body acceleration rates well beyond ±1G to navigate courses during efficient transition in and out of corners, accelerating from maximum straight-line speed to manageable cornering speeds, and then back to maximum straight-line speed. This dissertation aims to answer if longitudinal acceleration is important for road vehicle aerodynamics with the use of transient Computational Fluid Dynamics (CFD) to develop a method for obtaining ensemble averages of forces and flow field variables. This method was developed on a simplified bluff body, a channel mounted square cylinder, achieving acceleration through periodic forcing of far field velocity conditions. Then, the method was applied to an open-source road vehicle geometry, the DrivAer model, and a high performance model which was created for this dissertation, the DrivAer-GrandTouringRacing (GTR) variant, as a test model that generates considerable downforce with low ground proximity. Each test body experienced drag force variations greater than ±10% at the tested velocities and acceleration rates with considerable variations to flow field distributions. Finally, an empirical formulation was used to obtain non-dimensional coefficients for each body from their simulated force data, allowing for force comparison between geometries and modeling of aerodynamic force response to accelerating vehicle conditions.

ACKNOWLEDGMENTS

First, I must acknowledge Dr. Mesbah Uddin, my advisor, for introducing me to the field of automotive aerodynamics and computational fluid dynamics. Before entering his course on the fundamentals of road vehicle aerodynamics I was not certain of what my future or contribution to the field of mechanical engineering would be. I must also thank him not only for his knowledge of the field, but also his experience, enabling our research group to work with ”the big three” automotive manufacturers and several motor sports organizations, inevitably providing the frame work for my professional and academic career. I choose to work with Mesbah knowing that the work would be difficult, but it would be valid and we would both strive to make our mark in the field. It has been a long journey but I would not change any step even if I had the opportunity.

Second, I must thank my professors and committee members I have had the privilege of working with during my tenure as a student. Their commitments to the field build the next generation of scientists and engineers.

I would also like to thank the UNC Charlotte High Performance Computing group for supporting my research and work over the past 6 years, Jon, Mike and Mike probably know me only by my username from the queue and ticket list at this point.

All of this would have never been possible without the support of my family, especially my father for generating my interest in motor sport at a young age and maturing it through till adulthood by traveling the country every weekend from racetrack to racetrack. Without my family, I could have never started this journey.

Of course, at my side through this entire dissertation with unwavering support has been my beautiful wife, Jordan who has yet to learn of what I am like with access to free time away from a terminal window.

Additionally, my friends have been extremely supportive and anxious for the completion of this dissertation, which is proof that I really have been working on something all along.

And finally, I have worked with many outstanding people, in the lab, within race teams, small businesses and corporations who have taken chances on me and my abilities, helping me to grow as an engineer and challenging me every day.

TABLE OF CONTENTS

LIST OF FIGURES

LIST OF TABLES

CHAPTER 1: INTRODUCTION

The study of bluff bodies in fluid dynamics primarily focuses on a steady mean free stream flow velocity. While this may encompass majority of operating conditions, the effects of the fluid on the body due to an accelerating free stream condition are often ignored. Road vehicle aerodynamic engineers focus primarily on reducing over all drag of a vehicle, as it is a direct relation to fuel economy and top speed by tuning the drag coefficient with Equation 1 [5] and depends on the fluid density, ρ, vehicle cross sectional area, A, and vehicle velocity, V.

$$C_D = \frac{Drag}{\frac{1}{2}\rho A V^2} \tag{1}$$

Aerodynamic engineers do of course focus on other quantities such as aerodynamic lift, thermal controls and acoustics to reduce wind noise, to name a few areas. The question proposed by this dissertation: “is longitudinal acceleration important for road vehicle aerodynamics?”, which aims to explore the relevancy of unsteady mean flow for road vehicles with focus towards engineering tools. Literature review supports that accelerating flow investigations are not new, but have not been applied with significant detail to road vehicle aerodynamics.

While majority of aerodynamic testing and development of road vehicles focus on the steady state condition, this test envelope does not cover the entire operating condition for a road vehicle. Large forced body accelerations of 1G and greater occur from driver input or during collision avoidance maneuvers while weather conditions also induce far field accelerations. Analytical solutions for streamlined bodies can be obtained with potential flow field analysis, but cannot be applied to bluff bodies due to separated flow regimes (see Panton [48]). The accelerating case for bluff bodies is increasingly important for engineering applications where large accelerations occur, such as an automobile attempting to avoid a collision, high performance road vehicles traversing a course, missiles, and aircraft maneuverability, all of which experience transient weather phenomenon such as gusting and wind shear. Steady mean free stream flow experiments are inherently expensive to perform, especially at higher fluid speeds due to the power required to move the fluid. Additionally, wind tunnels create controlled test environments which are favored over field testing due to weather in the Earth's atmosphere causing non-repeatable test conditions. With this in mind, testing acceleration would require another order of complexity, lending to the advantages of computational fluid dynamics as a tool to investigate this case.

1.1 Dissertation Outline

This dissertation is organized in the following manner: Chapter 2 discusses the background of acceleration aerodynamics and relevant work that has already been compiled to date. Chapter 3 focuses on turbulence modeling and its significance for carrying out simulations in this dissertation. Chapter 4 details the numerical methods and grid creation for each simulation. This chapter is a necessary detail for any CFD study, but is not a required section for a reader who is interested in acceleration aerodynamics. Chapter 5 is the first investigation and development of investigating both the ensemble averaged body forces and flow field for an accelerating bluff body. Chapter 6 applies the process developed in Chapter 5 to a realistic road vehicle, the DrivAer model. Chapter 7 mimics Chapter 6 but includes the development of a model with a focus on high performance road vehicles in motor sport and investigates the impact of longitudinal acceleration on both drag and down force. Chapter 8 alludes to the potential for applying lessons learned from this dissertation to several areas of the road vehicle aerodynamics field, including dynamic modeling. Chapter 9 concludes the dissertation with a summary and outlines future explorations of the field.

CHAPTER 2: BACKGROUND

Additional forces resulting from accelerating a body through a fluid is not a new idea, Du Baut [9] proposed adding an additional mass to spheres accelerating in air and water after his experiments in 1786 failed to agree with Newtons second law of motion, Bessel[62] also proposed an added mass in 1828 while investigating the motion of pendulums. Bessel found that an added inertia was required to complete the reduction to a vacuum for his pendulum experiments where he deduced a value k, to be multiplied by the displaced mass of fluid for both air and water. Morison in 1953 [45] experimentally measured the force distribution of surface waves on cylindrical piles, determining a coefficient (the inertia coefficient) of $C_M = 1.96$ representing the added fluid forces for a round cylinder undergoing periodic acceleration in time. The inertia coefficient was determined through Equation 2 (the Morison Equation) where the total instantaneous force can be broken down into two components; part 1 representing the inertial force and part 2 representing the drag force. Equation 2 consists of: ρ, $\not{V}$, C_M, $\dot{V}_x$, A, C_D and V_x which represent: density of the fluid, volume of the test body, coefficient of mass, acceleration rate of the fluid or test body, frontal area of the test body, coefficient of drag and the velocity of the fluid or test body. A fundamental change of the Morison Equation and applying it as a function of velocity instead of time, could allow for the characterization of a road vehicle's dynamic force response to accelerating conditions, which will be explored further later on.

$$Fx(t) = \rho \forall C_M \dot{V} + \frac{1}{2}\rho A C_D V^2 \tag{2}$$

Several more recent papers have also explored acceleration of lifting devices as well as bluff bodies. Fackrell[15] investigated free falling spheres and cylinders with both experiments and numerical simulations, finding that the potential flow theory was sufficient for calculating the added-mass at initial onset of acceleration, not the total added acceleration force during sustained acceleration when separation was present. Fernando et al.[16] while investigating the acceleration of a sphere from both rest and steady-state velocity, concluded that the adverse pressure gradient at the rear of the sphere could be reduced significantly through body acceleration. Lee[38] experimentally measured the additional drag on circular and square wall mounted cylinders due to acceleration, concluding that the square cylinder would always see an increased value of drag for all Reynolds numbers tested, while other shapes may see variations depending on the location of flow separation onset. Roohani[53] while investigating the acceleration of 2D objects at both sonic and subsonic conditions, observed that, for subsonic flows over a NACA 2412 airfoil, there exists differences not only in body forces between non-accelerating and accelerating conditions but also that the stall angle of the airfoil varied ±4 deg. Zhang[68] experimentally measured the velocity front that occurs during the acceleration of spreading jets which was found to drastically reduce the overall entrainment, leading to a decreased decay of the center-line velocity and, as well as, the overall jet spreading rate.

Road vehicles undergoing unsteady mean free stream conditions have been investigated previously, yet none have focused on the fundamentals of pure longitudinal acceleration. Further yet, to the best of the authors knowledge none have implemented an ensemble averaging technique in an attempt to obtain averaged flow field conditions for a single velocity undergoing longitudinal acceleration. Forbes et al. [17] while simulating coupled vehicle handling and cross wind tests on the DrivAer model implemented gusting via cross flow input profile through a far field boundary condition. Simulating a vehicle passing through a wind gust is not equivalent to a pure body acceleration, however the Forbes et al. data set shows the gust created a large decrease in drag force while the vehicle entered into the cross-wind velocity profile, lift force did not show any discernable changes during this period. Nara et al. [29] conducted transient Large Eddy Simulation of a formula race vehicle navigating a course by matching experimental data for the trajectory of the vehicle with an Arbitrary Legrangian-Eulerian (ALE) non-inertial frame of reference to maneuver the vehicle. Their results indicated that the accelerating, decelerating and sliding of the vehicle created a discernable difference in the drag, lift and side forces compared to steady data at the same reference speeds. Aschwanden et al. [2] experimentally investigated the pitching and heaving of a scale model prototype race vehicle and application to vehicle dynamic simulation [3]. While this experiment was not done to investigate longitudinal acceleration, their conclusion was that motion aerodynamics must be considered for the simulation of the overall performance of the vehicle. The additional effect of this longitudinal acceleration can be included in high-fidelity race-vehicle dynamics models like the one proposed by Mohrfeld-Halterman and Uddin [44] for an improved prediction of vehicle handling characteristics. Computational

Fluid Dynamics (CFD) is already used to complement steady mean flow experiments, reducing design overhead, and has the potential for applications testing accelerating conditions as well.

Vortex lock-on (otherwise known as wake resonance) is another example of unsteady free-stream conditions, where a forced oscillation induces specific harmonics between the forcing frequency and the natural vortex shedding of the body. Bearman, Konstantinidis and coworkers have produced several in-depth studies [6, 32, 31, 33, 35, 34] (both numerical and experimental) on square and circular cylinders in vortex lock-on regimes. These studies all demonstrated considerable variations in mean drag force, root mean squared (rms) lift force, wake size, vorticity, and reynolds stresses due to their unsteady free-stream conditions. These works are similar to this paper but do not explore the same phenomenon and are included to provide insight and draw similarities in flow physics.

CHAPTER 3: TURBULENCE MODELING

In an ideal design process, physical testing of prototypes would be surpassed altogether and performed entirely in the digital domain. This would be done not out of necessity for reduction in costs or time, but due to extreme accuracy of simulation predictions. The ideal design process presented has not been observed by the author at the time of this dissertation and is a topic of debate for scientists and engineers in the automotive community. Several aspects must be considered in order to achieve an ideal simulation of a road vehicle at highway speeds, starting with a mathematical representation of fluid flow and then the means for solving said mathematical expressions for a road vehicle.

The Navier-Stokes equations are mathematical expressions for the fundamentals of viscous Newtonian fluid flows, derived from Newton's second law by Claude-Louis Navier and George Gabriel Stokes. While these equations do correctly represent the physics of fluids, they unfortunately do not have an explicit analytical solution beyond simplified flow regimes, thus we require numerical methods for their solution. Equation 3 represents conservation of mass while Equation 4 is the conservation of momentum, and Equation 5 represents the viscous stresses, τ_{ij} [49]. The incompressible variations are presented here due to low mach numbers experienced by road vehicles not requiring compressibility calculations.

$$\frac{\partial u_i}{\partial x_i} = 0 \tag{3}$$

$$\frac{\partial u_i}{\partial t} + u_j \frac{\partial u_i}{\partial x_j} = -\frac{1}{\rho}\frac{\partial p}{\partial x_i} + \frac{\partial \tau_{ij}}{\partial x_j} \tag{4}$$

$$\tau_{ij} = \mu\left(\frac{\partial u_i}{\partial x_j} + \frac{\partial u_j}{\partial x_i}\right) \tag{5}$$

3.1 Direct Numerical Simulation

To solve the Navier Stokes Equations directly without modeling would require the resolution of the smallest length and time scales of turbulence, through the Kolmogorov microscales. The Length, time and velocity scales are represented as Equation 6, Equation 7 and Equation 8 [63] respectively, where ϵ is the dissipation rate per unit mass ($\mathrm{m^2\,s^{-3}}$) and ν is the kinematic viscosity ($\mathrm{m^2\,s^{-1}}$). The Reynolds number that is formed by η and υ ($\frac{\eta\upsilon}{\nu}$) is equal to one, indicating that these small scales are dominated by viscous forces.

$$\eta \equiv \left(\frac{\nu^3}{\epsilon}\right)^{\frac{1}{4}} \tag{6}$$

$$\tau \equiv \left(\frac{\nu}{\epsilon}\right)^{\frac{1}{2}} \tag{7}$$

$$\upsilon \equiv (\nu\epsilon)^{\frac{1}{4}} \tag{8}$$

For a road vehicle such as the DrivAer model (see Chapter 6 at highway speeds of 80 mph (35.75 $\mathrm{m\,s^{-1}}$) and vehicle length scale of 4.6 m has a Reynolds Number of 1.64×10^7. Order of magnitude analysis enables an approximation of the Kolmogorov length and time scale via Equation 9 and Equation 10 with the largest possible eddy as the length of the vehicle (ℓ) and u as the free stream velocity to obtain the largest eddy turn over time $\frac{\ell}{u}$, then the Kolmogorov length scale $\eta = 17.85$ µm and time scale of $\tau = 31.77$ µs.

$$\frac{\eta}{\ell} \sim \left(\frac{u\ell}{\nu}\right)^{-\frac{3}{4}} = R^{-\frac{3}{4}} \tag{9}$$

$$\frac{\tau u}{\ell} \sim \frac{\tau}{t} = \left(\frac{u\ell}{\nu}\right)^{-\frac{1}{2}} = R^{-\frac{1}{2}} \tag{10}$$

As an approximation, with numerical grid spacing of η to discritize within 50 mm of the wall of the DrivAer model (which should encompass any boundary of shear layers where the Kolmogorov scale would need to be fully resolved) of surface area 30 m^2 would require a resolved volume of 1.5 m^3. This near body mesh alone would require 264 trillion cells. Of course apriori knowledge of the flow field could be applied to resolve the flow field based on Kolmogorov length scales predicted from RANS predictions of ϵ , however the Kolmogorov time scale τ would still require 30 thousand time steps to simulate 1 s of real time. The existence of a CFD simulation with more than a billion or two finite volume cells is unknown to the author, thus a Direct Numerical Simulation cannot currently be used for road vehicle aerodynamics.

3.2 Large Eddy Simulation

To reduce the computational requirements of a Direct Numerical Simulation, modeling must be employed to reduce complexity of the problem. Large Eddy Simulation (LES) segregates the Navier Stokes Equations into resolved and unresolved portions, allowing for coarser grid resolutions overall. For an accurate simulation, this must be done properly to capture the largest anisotropic energy carrying eddies, leaving only the smallest scales of isotropic turbulence to be modeled. Pope [49] outlines modeling for LES simulation and is added here for modeling discussion.

LES segregates the scales of turbulence with a filter into the resolved and unresolved "residual" portions as done in Equation 11.

$$u(x,t) = \hat{U}(x,t) + u'(x,t) \tag{11}$$

Then, after filtering is applied to the momentum equation and adjustments are made realizing that filtered velocity products are not equivalent to filtering the product of velocities, there is an extra term as seen in Equation 12 which must be modeled.

$$\frac{\partial \hat{U}_i}{\partial t} + \frac{\partial \widehat{U_i U_j}}{\partial x_i} = -\frac{1}{\rho}\frac{\partial \hat{p}}{\partial x_i} + \frac{\partial \hat{\tau}_{ij}}{\partial x_j} - \widehat{u_i' u_j'} \tag{12}$$

Smagorinsky [56] proposed Kolmogorov's Bousinessq approximation to close the anisotropic residual stresses τ_{ij}^r with unfiltered velocity data via Equation 13 where $\tau_{ij}^r = 2\nu_r \widehat{S_{ij}}$ and κ_r is the residual energy.

$$-\widehat{u_i' u_j'} = 2\nu_r \widehat{S_{ij}} - \frac{2}{3}\kappa_r \delta_{ij} \tag{13}$$

Residual eddy viscosity ν_r is modeled with the mixing-length hypotheses in Equation 14 where $\widehat{\mathcal{S}}$ is the filtered rate of strain, ℓ_S is the Smagorinsky length scale and *Delta* is the filter width. The Smagorinsky coefficient, C_S, can be derived for high Reynolds number flows through several different methods, Lilly [39] first did this by focusing on the inertial subrange and the integral length scale setting Δ to ℓ_{EI} equal to $\frac{1}{6}L_{11}$ the integral length scale (this way 80% of the energy carrying scales are resolved) determining a C_S value of 0.17. Unfortunately this is an area of weakness for LES simulations, as the choice of filter type will effect the calculation of C_S and the transfer of energy to the residual scales. More information is available in Pope [49] where he notes that if the filter width (and numerical grid size) are small enough in relationship to the Kolmogorov scale ($\frac{\Delta}{\eta}$)) then the value of C_S should not be a concern.

$$\nu_r = \ell_S^2 \widehat{\mathcal{S}} = (C_S \Delta)^2 \widehat{\mathcal{S}} \tag{14}$$

Assuming that LES with sufficient near wall resolution (NWR) is employed for a road vehicle and 80% of energy is resolved everywhere, what would the computational overhead be at highway speeds? Fröhlich [18] while investigating LES of separated channel flow determined that a filter width 12 times larger than the Kolmogorov length scale was ideal. Citing the previously mentioned full scale DrivAer Kolmogorov length scale of $\eta = 17.85$ µm and time scale of $\tau = 31.77$ µs, this would enable a CFD simulation to resolve only down to a length scale of 0.21 mm and time scale of 0.38 ms. This would be a significant improvement over a DNS grid, only requiring 152 billion cells to resolve the 50 mm volume near the body, a 4 orders of magnitude improvement, but still out of reach for even the best HPC systems today. An additional improvement would be from the time scale only requiring 2630 time steps to simulate 1 s of real time. This is still not suitable for current computational resources, however there are also variants of LES with near-wall modeling (NWM) which could reduce grid spacing requirements near the wall, but I digress that this is still 4 orders of magnitude away from a feasible solution.

3.3 RANS Turbulence Modeling

In CFD Simulation, the lowest computationally intensive type of turbulent flow simulation is to employ Reynolds Averaging to the Navier-Stokes equations, while this method is efficient due to the relaxation of grid spacing requirements, it also has the most physics modeling which are a potential source for error. To achieve this, Reynolds Decomposition is employed assuming that turbulence is statistically stationary or that fluctuations are about a mean value. The result are the Reynolds-Averaged Navier-Stokes (RANS) equations represented as Equation 15 and Equation 16.

$$\frac{\partial U_i}{\partial x_i} = 0 \tag{15}$$

$$\frac{\partial U_i}{\partial t} + U_j \frac{\partial U_i}{\partial x_j} = -\frac{1}{\rho}\frac{\partial P}{\partial x_i} + \frac{1}{\rho}\frac{\partial \tau_{ij}}{\partial x_j} - \frac{\partial \overline{u_i' u_j'}}{\partial x_j} \tag{16}$$

Noticeably, there is an additional component, $\overline{u_i' u_j'}$, known as the Reynolds Stress tensor, which governs the effect of fluctuating turbulence to the mean flow. The Reynolds Stress tensor is one bane of RANS modeling, either the additional 6 transport equations must be solved independently or the Boussinesq [8] approximation can be applied. Boussinesq proposed the use of turbulent-viscosity (ν_t or eddy-viscosity) which is mathematically analogous to the stress-rate-of-strain relation for a Newtonian fluid [49]. The use of turbulent-viscosity seems illogical at first, as the quantity is a result of the local flow field, not the molecular properties of the fluid itself, nonetheless the hypothesis is sufficient as the backbone for many successful RANS turbulence models employed for years by scientists and engineers to design cars, airplanes, ships, rockets and medical equipment. Equation 17 below is the result of the Boussinesq approximation, allowing for the simple calculation of Reynolds stresses based on turbulent energy κ, eddy viscosity υ_t and mean rate of strain.

$$\overline{u_i'u_j'} = \frac{2}{3}\kappa\delta_{ij} - \nu_t\left(\frac{\partial \bar{U}_i}{\partial x_j} + \frac{\partial \bar{U}_j}{\partial x_i}\right) \tag{17}$$

Another bane of RANS models is the need to calculate eddy-viscosity, a calculation that has been the focus of copious research and deliberation, resulting in dozens of models of which 15 are cataloged by NASA on their turbulence modeling verification website (https://turbmodels.larc.nasa.gov), this is not the focus of my research, nor is it a part of my contribution to the field. I will however give a short background of this area ending with the turbulence model used in my simulations.

The simplest eddy-viscosity model, the mixing length model for a two-dimensional boundary layer, υ_t, can be calculated with Equation 18.

$$\nu_t = \ell_m^2\left|\frac{\partial U}{\partial y}\right| \tag{18}$$

In the previous section, Smagorinsky [56] proposed Equation 14 on the basis of the mean rate of strain. This can also be applied here, however there is a shortcoming where the mixing length, ℓ_m, has to be specified and requires apriori knowledge of the flow field, this does enable this simple model to predict flows quite well and is explored in Wilcox's book [65]. As simple as this model is, predicting the mixing length for complicated geometries eliminates this algebraic formulation for road vehicles. Additionally, the mixing length model would predict the eddy viscosity is zero when $\frac{\partial U}{\partial y} = 0$ which we know to not always be true, such as the center of a round jet or in decaying grid turbulence [49]. Interestingly, both Kolmogorov [30] and Prandtl [50] independently suggested using turbulent kinetic energy instead of mixing length to get the velocity scale. This lead to their conclusion of the necessity of a transport equation to solve for κ (the turbulent-kinetic energy), thus a one-equation model, which unfortunately still required the definition of the mixing length. Spalart and Allmaras [59], with a focus on industrial aircraft aerodynamics, created a one equation model that has a transport equation for eddy viscosity where eddy viscosity is defined as in Equation 19.

$$\nu_t = \tilde{\nu} f_{\nu 1} \tag{19}$$

And the eddy viscosity transport equation:

$$\frac{\partial \tilde{\nu}}{\partial t} + U_j \frac{\partial \tilde{\nu}}{\partial x_j} = c_{b1} \tilde{S} \tilde{\nu} - c_{w1} f_w \left(\frac{\tilde{\nu}}{d} \right)^2 + \frac{1}{\sigma} \frac{\partial}{\partial x_\kappa} \left[(\nu + \tilde{\nu}) \frac{\partial \tilde{\nu}}{\partial x_\kappa} \right] + \frac{c_{b2}}{\sigma} \frac{\partial \tilde{\nu}}{\partial x_\kappa} \frac{\partial \tilde{\nu}}{\partial x_\kappa} \tag{20}$$

Where:

$$f_{\nu 1} = \frac{\chi^3}{\chi^3 + c_{\nu 1}^3}, \; f_{\nu 2} = 1 - \frac{\chi}{1 + \chi f_{\nu 1}}, \; f_w = g \left[\frac{1 + c_{w3}^6}{g^6 + c_{w3}^6} \right]^{\left[\frac{1}{6}\right]} \tag{21}$$

c_{b1}	c_{b2}	$c_{\nu 1}$	σ	c_{w2}	c_{w2}	c_{w3}	κ
0.1355	0.622	7.1	$\frac{2}{3}$	$c_{w1} = \frac{c_{b1}}{\kappa^2} + \frac{1+c_{b2}}{\sigma}$	0.3	2.0	0.41

Table 1: Modeling coefficients for the Spalart-Allmaras one-equation RANS turbulence model

$$\chi = \frac{\tilde{\nu}}{\nu},\ g = r + c_{w2}(r^6 - r),\ r = \frac{\tilde{\nu}}{\tilde{S}\kappa^2 d^2} \tag{22}$$

$$\tilde{S} = S + \frac{\tilde{\nu}}{\kappa^2 d^2} f_{\nu 2},\ S = \sqrt{2\Omega_{ij}\Omega_{ij}} \tag{23}$$

Noting that S is vorticity magnitude, d is the distance to the wall which enables eddy viscosity to be present away from the wall. The one-equation Spalart-Allmaras model is complete, meaning that turbulent length scales are automatically defined and there is no included adjustable closure coefficient and is the simplest complete model. Modeling coefficients are presented in Table 1. Note that the model even includes a transition correction, but is not presented here.

Note that if accuracy were the only criteria for choosing the level of turbulence modeling, the choice would tend towards a model with more complexity at a higher computational cost. The Spallart-Allmaras model is the least complex yet complete model and has been widely used (and still is used), however the model performs poorly for separated flow cases [65] and will not be employed in this dissertation. This leaves a higher accuracy model to be desired for automotive aerodynamics due to their large variation of complex bluff body geometries resulting in different separation and wake patterns.

Kolmogorov was the first to propose a two-equation model for turbulence, choosing a second parameter of dissipation per unit turbulence kinetic energy ω. His model that he proposed with a transport equation for ω was based purely on order of magnitude analysis, and has been modified by other researchers to address shortcomings. The $k-\epsilon$ of Jones and Launder [27] and $k-\omega$ of Wilcox [65] two equation models are widely popular and both solve for the velocity scale through turbulent kinetic energy with a second transport equation to solve for the turbulent length scale. Where these two models are different, is that $k-\epsilon$ uses a turbulent energy dissipation rate, while $k-\omega$ uses a specific dissipation rate. Each model does however have shortcomings, the $k-\epsilon$ model trends towards higher eddy-viscosity near the wall as k tends towards zero near the wall $\nu_t = \frac{\epsilon^2}{k}$ is in a divide by zero situation, which requires additional damping functions for $k-\epsilon$. The $k-\omega$ model suffers from sensitivities of free stream ω, causing undesired changes to ν_t. Both of these shortcomings were addressed by Menter [42] who combined both the $k-\epsilon$ and $k-\omega$ models together into the Shear Stress Transport (SST) model, using $k-\epsilon$ in the outer wake region and $k-\omega$ in the near wall regions. This model does however increase significantly in complexity, but is considered to be a robust two-equation RANS model, as it addresses shortcomings of stand alone two-equation models. The $k-\omega$ SST Menter model is presented in Equation 24 and Equation 25 to demonstrate the level of complexity that RANS models can quickly take on. Note that the blending function F1 in Equation 25 blends between the near wall ω based and ϵ models with several nested logical functions to ensure proper transfer. The details of this model will not be discussed here, a curious reader is encouraged to again visit the NASA turbulence modeling verification website (https://turbmodels.larc.nasa.gov).

$$\frac{\partial k}{\partial t} + \frac{\partial u_j k}{\partial x_j} = P - \beta \omega k + \frac{\partial}{\partial x_j}\left[(\mu + \sigma k \mu_t)\frac{\partial k}{\partial x_j}\right] \tag{24}$$

$$\frac{\partial \omega}{\partial t} + \frac{\partial u_j \omega}{\partial x_j} = \frac{\gamma}{\nu_t}P - \beta \omega^2 + \frac{\partial}{\partial x_j}\left[(\mu + \sigma_\omega \mu_t)\frac{\partial \omega}{\partial x_j}\right] + 2(1 - F_1)\frac{\sigma_\omega 2}{\omega}\frac{\partial k}{\partial x_j}\frac{\partial \omega}{\partial x_j} \tag{25}$$

Even with all of the complexities present in the Menter SST model, it fails to accurately predict automotive flow fields due to their inability to resolve large scale unsteadiness, resulting in errors for shear layers, inevitably failing to predict separation lengths [23]. Thus, another approach was desired for this dissertation to avoid unforeseen errors from turbulence modeling effecting acceleration physics.

RANS grid requirements do not require the resolution of turbulent scales and only require enough resolution to capture velocity gradients and underlying geometry. Even the requirement to capture velocity gradients becomes smaller when wall functions are used at no-slip wall boundary conditions, allowing for larger wall normal growth rates of near wall cells. For example, Ashton et al. [4] performed mesh sensitivity studies for the DrivAer model with several RANS turbulence models (Menter-SST, Realizable $k - \epsilon$, Spalart-Allmaras, and other non-linear eddy viscosity models) during steady simulation, sweeping mesh counts from 18, 36 and 90 million. Their results varied for different variants of the DrivAer, but for the fastback configuration (used in Chapter 6) the CD value reduced 14% from 18 to 36 million but only 2.5% from 36 to 80 million cells. For these reasons, RANS turbulence modeling has been extremely popular since their development has allowed a sufficient engineering solution for road vehicles over the last 20 years while computer performance has steadily been improving.

3.4 IDDES

As a compromise between efficiency and accuracy, it would be beneficial to implement RANS turbulence modeling near the wall while still using LES simulation to capture the largest energy carrying scales of turbulence outside of the boundary layer. This type of simulation has already been developed and is known as a class of simulations as Wall-modeled LES. Shur et al. [55] proposed this type of LES simulation in 2008 where the near wall regions within the boundary layer are solved as a RANS model and is known as Improved Delayed Detached-Eddy simulation (IDDES). But first, we should discuss earlier techniques such as Detached Eddy Simulation (DES).

Detached Eddy Simtulation (DES), first proposed by Spalart et al. [60], pioneered the idea to divide the computational domain up into unresolved RANS regions and resolved LES regions simultaneously in 1997. This was done by coupling Spalart-Allmaras RANS model with LES through the turbulent length scale, effectively replacing the LES sub grid model with RANS depending on grid resolution. For DES, the LES turbulent length scale takes on the form:

$$L_{LES} = C_{DES}\Delta \tag{26}$$

Where C_{DES} is a constant which is generally tuned for each CFD code depending on numerics and underlying RANS model to calculate the appropriate amount of dissipation, and is set to a value of 0.6 in the original Spalart paper. Δ is the LES filter width and relies on the local mesh resolution. The DES length scale, L_{DES} takes on the smallest local value for length scale, which in the near all regions, the RANS length scale is utilized. Unfortunately for road vehicle simulations, the grid resolution alone cannot be used to as the only filter and DES suffers from mesh resolution sensitivities. For example, if a mesh dependency study is performed, an increase of resolution in the near wall region can cause LES mode to be triggered near the wall in the boundary layer, causing inaccurate predictions for separation. This inaccuracy was determined by Menter and Kuntz [43] in 2004 as grid induced separation (GIS). Due to this discovery, DES was modified by Spalart et al. again in 2006 [61] to force the RANS region near the wall in the same manner that the RANS SST model does with a switching function based on wall distance. This however has not solved all issues and has been modified several times since Spalart's 2006 modification.

This leads us forward/back to IDDES, which will switch between DDES and wall modelled LES depending on the amount of grid resolution near the wall and the amount of local turbulence. IDDES consists of several filters and switching functions that do require tuning, but are often handled by commercial CFD codes. A curious reader is encouraged to read Shur et al. [55] for further details. At the time of this dissertation IDDES is an efficient balance to simulate acceleration for road vehicles, allowing for the resolution of the highest energy containing eddies without the necessity of high near wall mesh resolution and the lowest sensitivity to near wall mesh resolution.

To review our mesh requirement for an IDDES simulation, we could assume that for a full scale DrivAer model with surface area equal to thirty square meters, if we only had to resolve the volume within the first 25 mm of the wall and resolve only seventy times the Kolmogorov scale to resolve the Taylor scale, our scale resolved portion of the mesh would only require 385 million cells (a three order of magnitude improvement over LES). Recall that this requirement is many orders of magnitude smaller than the original DNS mesh presented earlier (6 orders of magnitude), but still one order of magnitude greater than the RANS meshes used by Ashton et al. [4].

Later on in Chapter 6, the 40% scale model of the DrivAer is used, which has a significantly smaller surface area and should also have a similar shear layer requirements, would only require 24.6 million cells near the body for IDDES simulation.

CHAPTER 4: NUMERICAL SETUP

This chapter contains significant detail relating to the numerical setup of each simulation and the finite volume grids created. Also in this section, the details of the acceleration process are documented for each geometry. Settings for each simulation do change during the course of this dissertation due to the conglomeration of knowledge steadily increasing with each successive simulation. Even the version of CFD code used changed during this dissertation, as more than a year passed from the first set of simulations to the final set. The Square Cylinder study was carried out with commercial finitive volume CFD code, STAR-CCM+ v11.04 and the DrivAer studies used STAR-CCM+ v12.06. All simulations were performed as Improved Delayed Detached Eddy Simulations (IDDES) [55, 22], with Menter shear stress transport (SST) k-ω [42] turbulence modeling for the Reynolds Averaging Navier Stokes (RANS) region. As discussed in Chapter 3 IDDES is an efficient solution between LES and RANS, resolving the most relevant scales of turbulence for high Reynolds number transient flows with available computational resources. IDDES has been a popular tool in computational fluid dynamics research since it was proposed [24]. Literature suggests that IDDES approach has the following advantages over the standard DES model: (a) it provides shielding against Grid Induced Separation (GIS), similar to the DDES model, (b) allows the model to run in WMLES mode in case of unsteady inlet/free-stream conditions, (c) allows the LES simulation of wall boundary layers at much higher Reynolds numbers than standard LES models, and (d) it is self-adaptive in such a way that it reverts to DDES when the requirements/demands for WMLES are not satisfied. However, the model formulation is relatively complex and beyond the scope of the current paper, and, as such, an interested reader is referred to the original publications of Shur et al. [55] and Gritskevich et al. [22]. Previous studies have demonstrated that fully resolving all scales of turbulence may not be required for predicting major quantities of engineering interest, like force and moment coefficients and the mean flow field, with reasonable accuracy. For example Trias [64] performed DNS on the same channel mounted cylinder in this dissertation for a Reynolds number of 2.2×10^4 and achieved results near experimental values, while the current study demonstrates in Chapter 5 that IDDES also achieves results well within acceptable accuracy with less computational overhead. There is also an unavoidable increase in simulated time to obtain ensemble averaged flow fields that smooth out turbulent noise (33 acceleration-deceleration samples in the Square Cylinder Study). Steady mean flow transient simulations average over vortex-shedding cycles such as Sohankar et al. [58] time-averaging over 20 cycles, and Rodi et al. over 10 cycles [51].

4.1 Common Numerical Grid Settings

A number of techniques have been suggested in the past for *a priori* estimates of the minimum sufficient grid resolutions for LES. These can be grouped into four major classes: rules of thumb, techniques based on prior RANS results, single-grid estimators and multi-grid estimators (see Celik et al. [12]). According to Gant [19], various single-grid estimators include: (a) ratio of the SGS to the laminar viscosity (ν_t/ν),

(b) relative effective viscosity index, (c) ratio of the cell size to the Taylor microscale, (d) the Subgrid activity parameter, (e) ratio of the resolved to total turbulent kinetic energy, and (f) analysis of power spectra. Gant [19] also discussed recommended values of these parameters and examples of their use as seen in literature. Additionally, Kuczaj et al. [36] suggested that in order to obtain numerical solutions close to the experimental ones, for a the turbulent mixing flow in a T-junction, one must resolve the Taylor microscale length; they suggested that for an optimal simulation the finest mesh should be of the order of the Taylor microscale obtained from the RANS simulations. However, based off of their simulations, they cautioned that finer meshes must be used in order to accurately capture fluctuations in the shear layer close to the center of the mixing zone. In this paper, the Taylor microscale (λ) was first estimated using Equation 27 as given by Tennekes and Lumley [63], where A_1 is an undetermined constant set to 0.5, Re is the Reynolds number and L is the length scale. This value of λ was then used as a guide to set the grid spacing required to resolve majority of the inertia driven eddies; Wilcox[65] indicated that λ is approximately 70 times greater than the Kolmogorov scale, thus this IDDES simulation should leave only the smallest eddies to be modeled.

$$\lambda = \sqrt{15}\frac{1}{\sqrt{A_1}}\frac{1}{\sqrt{Re}}L \tag{27}$$

For each simulation in this dissertation, the approximated Taylor microscale was resolved near the body, with surface resolutions set to finer than this scale and the wake regions set to double this scale. The reasoning for this distribution is to promote efficient mesh distribution, being that the smallest resolved scales should be near the shear layers near the body and then increase further away from the body in size.

4.2 Square Cylinder Numerical Setup

For the range of velocities investigated in this study, the Reynolds number spanned from 3.2×10^4 to 3.6×10^5 which was centered around the target Reynolds number of 1.9×10^5 based on the length scale of $H = 0.5$ m and mean $V_{inlet} = 6\ \mathrm{m\,s^{-1}}$. The square cylinder with dimension $H \times H \times 6H$, was mounted inside a $39H \times 15H \times 6H$ channel which serves as the computational domain as can be seen in Figure 1. This figure also shows the coordinate system used in this study where x,y, and z represent the streamwise, vertical and lateral directions respectively. The origin of the coordinates system lies at the center of the cylinder on the center xy plane of the channel. Note that all length scales in this paper will by normalized by H and will be denoted by a superscript *; the subscripts x, y, and z will correspond to the stream-wise, wall-normal and span-wise component of a vector quantity. All statistics presented in this study are presented in the center plane ($H_z^* = 0$), which per Rodi et al. [52], for a $6H$ wide channel, should be independent of span-wise extent.

A velocity inlet is specified upstream of the cylinder, the domain outlet was held at constant pressure, top and bottom walls were set as zero-gradient boundaries while the channel side walls were set as periodic; all surfaces of the cylinder were treated as viscous wall boundaries. The reference velocity V_{ref} is the average of velocities recorted at $(0, 7H, 0)$ and $(0, -7H, 0)$; the locations of these two points are marked in Figure 1 as well. Varying the inlet velocity, while keeping the object stationary, is dynamically equivalent to a body moving with non-uniform velocity in a still fluid as determined by Wong et al.[66]. The former is a simpler method and provides an easier numerical implementation for CFD simulations. The domain $V_{inlet}(t)$ was controlled through a field function driven by the linear interpolation of a file table containing the periodic signal shown in Figure 2. This table was generated from a short python code that allowed the specification of the acceleration rate, the min/max velocity, and a coast time to aid in smoothing the turn around from acceleration to deceleration. These inputs were then concatenated together for many periods (this signal seen in black) and then smoothed via a Savitzky-Golay filter[54] within the python signal library. A zoomed plot of $V_{inlet}(t)$ in Figure 2, demonstrates that majority of the signal is consumed in changing acceleration rate, where the primary focus was to obtain constant rate of $\pm 20\ \mathrm{m\,s^{-2}}$ at $\pm 6\ \mathrm{m\,s^{-1}}$. . The entire simulation required 520 hours on 144×2.4 GHZ Intel Xeon E5-2665 processors (74,880 CPU Hours) to run through a total of 33 acceleration-deceleration periods.

4.2.1 Square Cylinder Numerical Grid

The simulation domain was discretized with hexahedral cells of varying sizes which are summarized in Table 2. The upper bound on grid spacing was set to $\frac{H}{2}$ and can be seen in Figure 4 denoted as region A. Region C was set to $\frac{H}{16}$ within ±3H of the cylinder in the cross stream direction to support SEM length scale advection applied at the velocity inlet. The near field region depicted as D in Figure 5 was set to a spacing of $\frac{H}{32}$ which is nearly twice the calculated value of the Taylor microscale from Equation 27 and spans a region from 2H upstream and 6H downstream of the cylinder

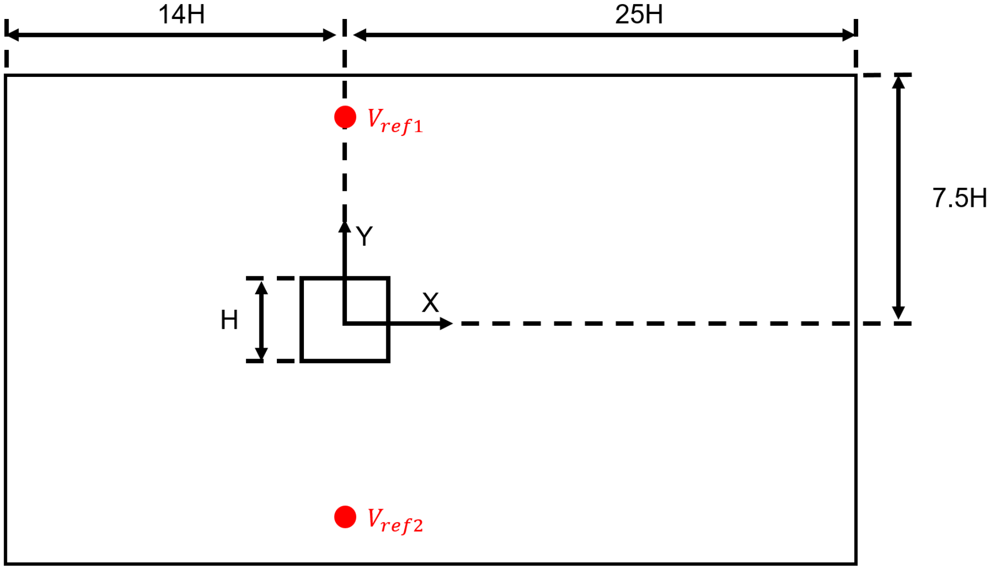

Figure 1: Overall channel dimensions (not to scale)

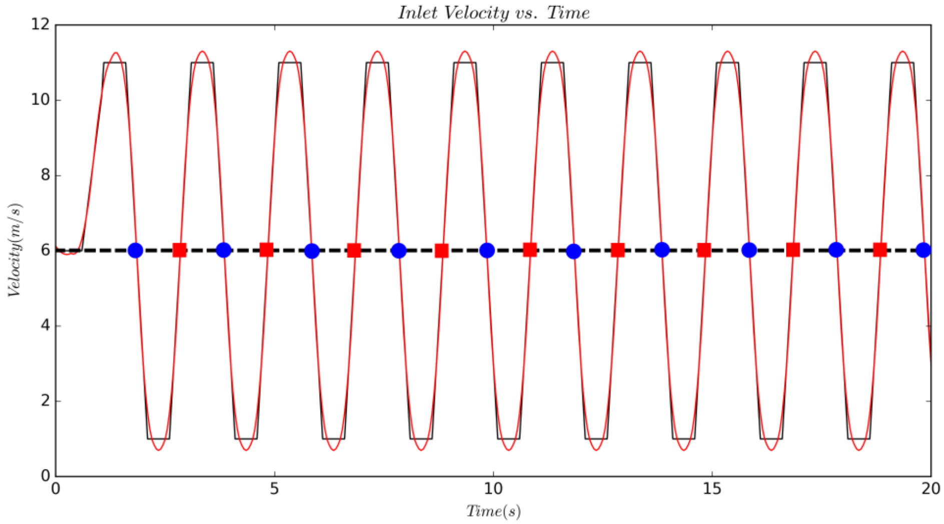

Figure 2: The periodic signal for $V_{inlet}(t)$ over 20 seconds. Black and red lines represent the raw user input signal and smoothed signal respectively. The blue circles and red squares along the dotted black line indicate instances of recorded deceleration and acceleration events respectively.

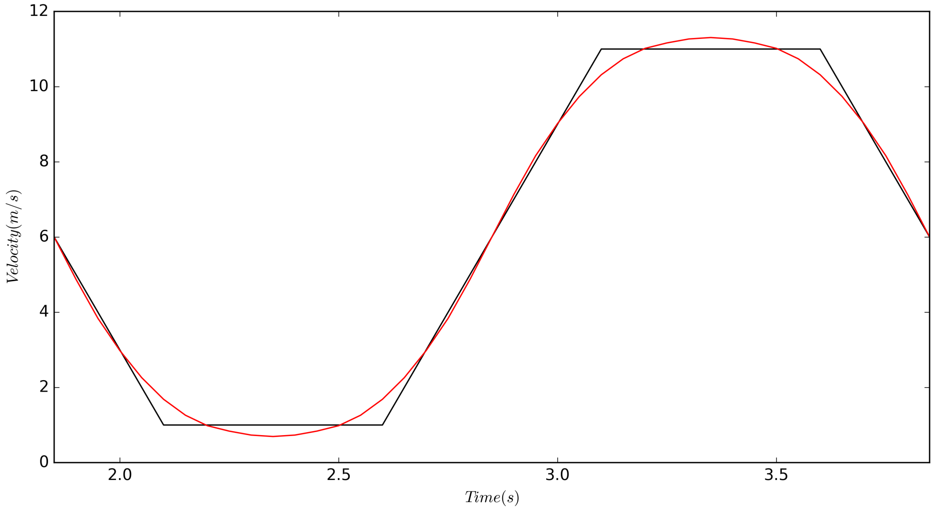

Figure 3: A zoomed plot of the periodic signal for $V_{inlet}(t)$ during one period. Black and red lines represent the raw user input signal and smoothed signal respectively.

Table 2: Grid spacing values non-dimensionalized by cylinder height H

Mesh Region	A	B	C	D	E	F
Grid Spacing	$\frac{H}{2}$	$\frac{H}{4}$	$\frac{H}{16}$	$\frac{H}{32}$	$\frac{H}{128}$	$\frac{H}{256}$

and ±2H about the cylinder in the cross-flow direction. Region E seen in Figure 6 encompasses the volume within 0.17H of the cylinder and is held to a maximum size of $\frac{H}{128}$. Region F was created by growing 2 wall normal layers of equal height equal to $\frac{H}{256}$ as shown in Figure 6.

Note that the first acceleration-deceleration period was included in ensemble averaging due to initialization from a previous steady V_{inlet} solution.

4.3 DrivAer CFD Model

For this study the 40% scale fastback DrivAer model was utilized with a smooth floor, mirrors and smooth wheels. A simplified tire contact patch was created of which the details can be seen in Figure 8. Overall domain dimensions can be seen in Figure

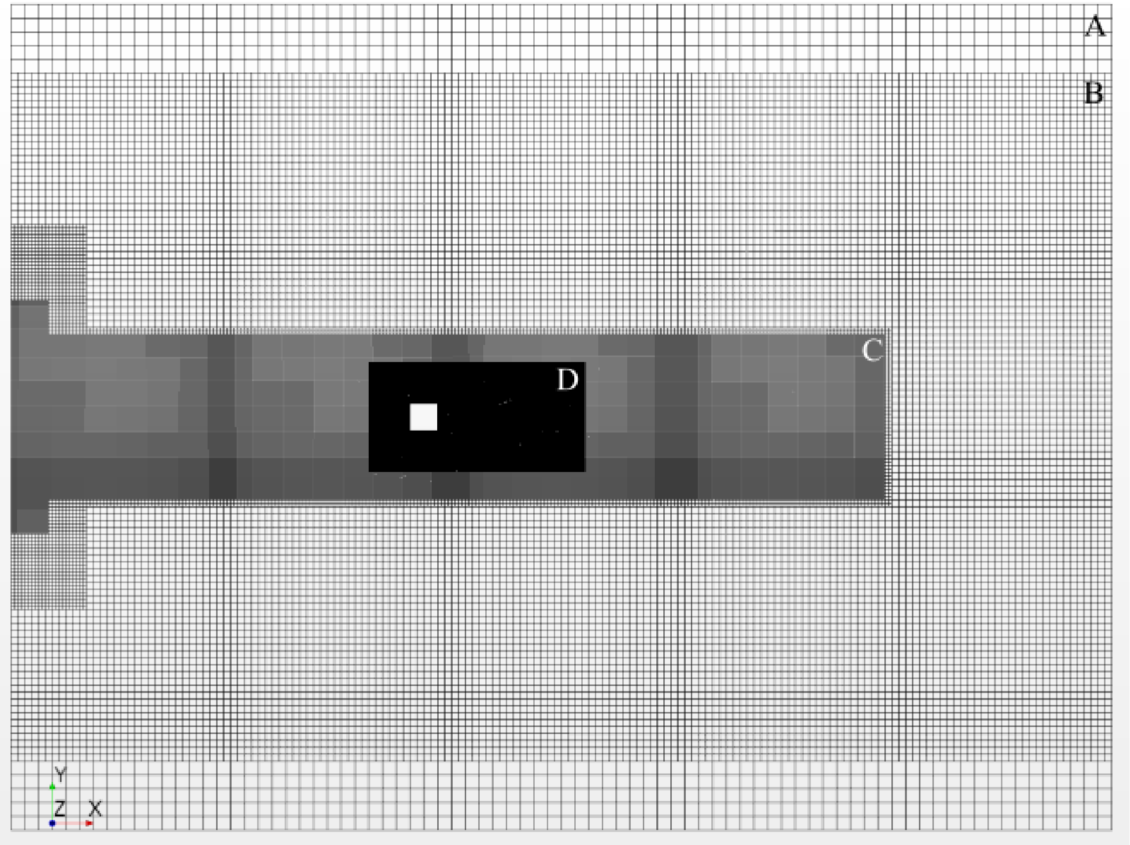

Figure 4: Overall mesh viewed at cylinder centerline

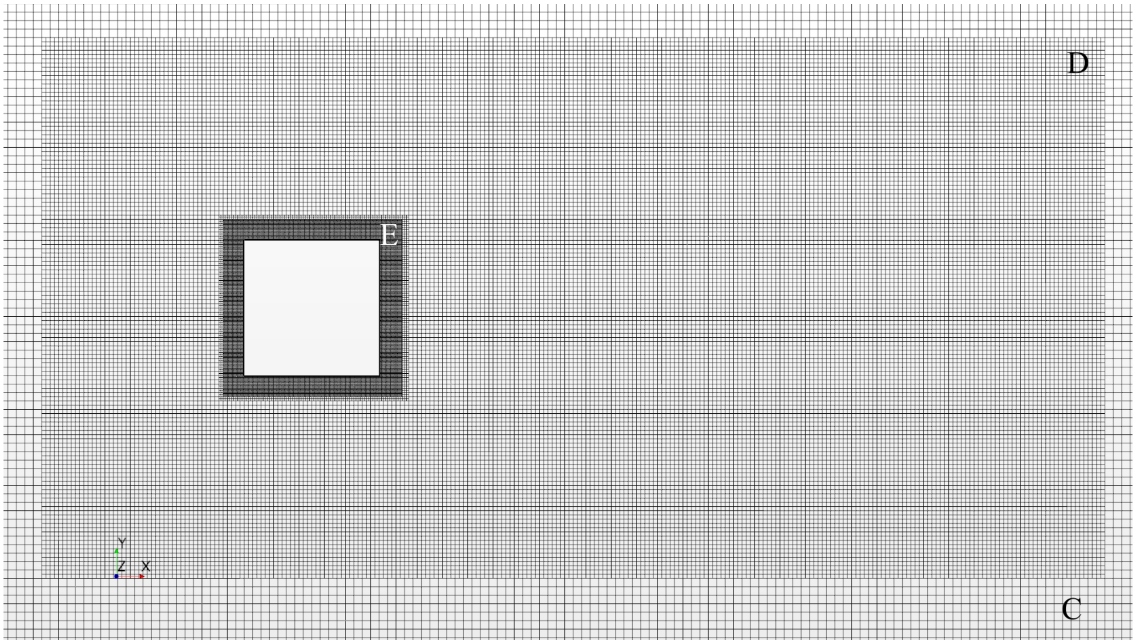

Figure 5: Near body mesh viewed at cylinder centerline

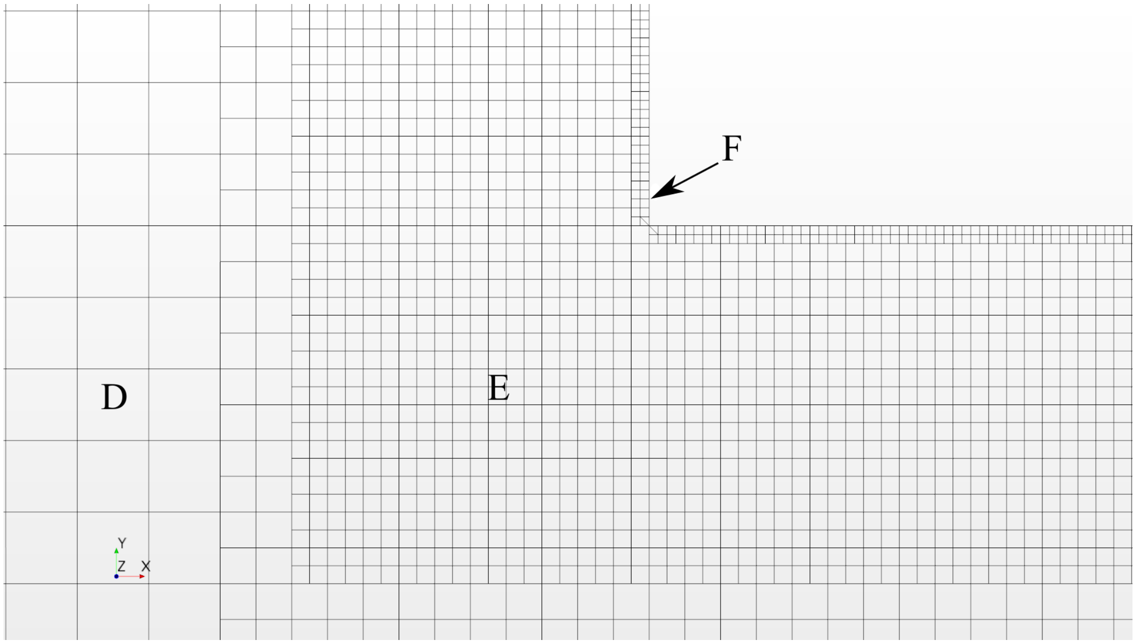

Figure 6: Cylinder corner mesh viewed at cylinder centerline

7 where all quantities are non-dimensional based on the vehicle wheel base length L =1.114 m. A velocity inlet was specified upstream of the vehicle where the velocity signal is a function of time and is discussed in more detail in the following section. Due the inlet velocity varying with time, $V_{ref}(t)$ was calculated as the average of two reference velocities taken at $X = 0.5L$. The side walls of the domain were specified as slip walls and the floor was specified as a wall velocity which was equal to $V_{ref}(t)$ as well as the wheel rotation rates which were also scaled with $V_{ref}(t)$ on a rotating wall condition, while the outlet downstream of the vehicle was set as constant pressure.

Using Equation 27, the Taylor Scale was calculated to be $\lambda = 2.5$ mm based on the height of the DrivAer for this acceleration study. Due to computational and time resources, the wake grid size (labeled as size ”D” in Table 3 and Figure 10)was held to 5 mm which is well within an order of magnitude to ideal grid spacing. As previously done in the cylinder simulation, the synthetic eddy method (SEM) of Jarrin et al. [26]

Table 3: DrivAer Grid spacing values non-dimensionalized by wheel base length $L = 1.114\,\mathrm{m}$ and exact values

Mesh Region	A	B	C	D	E	F
Grid Spacing/L	0.144	0.036	0.009	0.0045	0.0023	0.0011
Grid Spacing (mm)	160	40	10	5	2.5	1.25

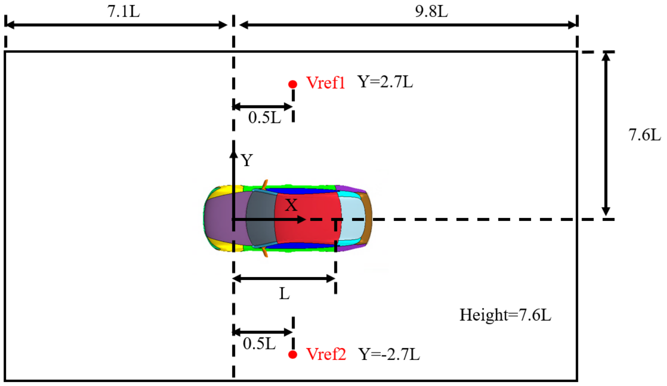

Figure 7: Overall numerical domain layout and critical dimensions represented in characteristic lengths. Note that the diagram is not to scale.

was implemented at the inlet and supported by a path of 40 mm volume cells labeled as size ”B” in Table 3 and Figure 9. Closer to the body where the smallest resolved scales occur, grid sizing was held to the calculated Taylor scale of 2.5 mm and is labeled as ”E” in in Table 3 and Figure 11. Four wall normal prism layers were grown with first layer thickness equal to 0.5 mm and total layer thickness equal to 2 mm. Additional details of the grid distribution can be seen in the following figures, noting that an ideal grid distribution would hold the Taylor scale throughout the nearbody region, but is unachievable with available computational resources. The final grid count for this DrivAer study was 42 million unstructured finite volume cells.

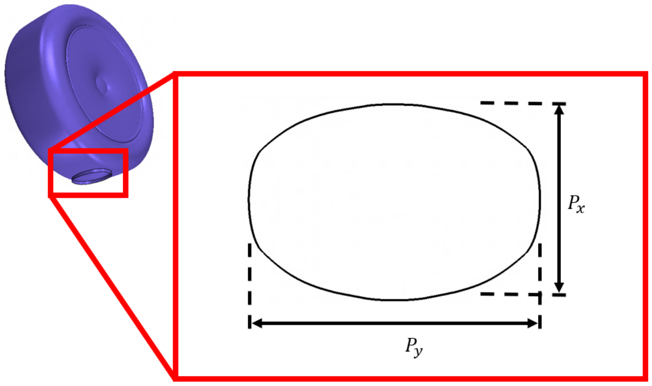

Figure 8: Detailed tire contact patch profile viewed normal to the xy plane. The width,length and height of the contact patch was set to $P_x = 0.087L$, $P_y = 0.128L$ and $P_z = 0.009L$.

4.4 DrivAer Acceleration Setup

Velocities ranged from $25\,\mathrm{m\,s^{-1}}$ to $55\,\mathrm{m\,s^{-1}}$resulting in a Reynolds number range (based on wheelbase length L =1.114 m) from 1.78×10^6 to 3.92×10^6, centered around the target velocity of $40\,\mathrm{m\,s^{-1}}$ and a Reynolds number of 2.85×10^6. The frontal reference area (including wheels) Aref=$0.3457\,\mathrm{m\,s^{-2}}$ was used to calculate force coefficients along with Vref(t).The inlet turbulence was specified with a non-dimensional turbulence intensity of 0.01 and a synthetic eddy length scale of 40 mm. The inlet velocity was held to $55\,\mathrm{m\,s^{-1}}$ for 2 s of simulated time before beginning acceleration periods.When the inlet velocity was equal to $40\,\mathrm{m\,s^{-1}}$ the timestep was set to 0.0001 s and is increased or decreased with respect to the inlet velocity. This was done to maintain a constant CFL value throughout the entire simulated time. Simulations were carried out with constant density air, neglecting compressibility due to the largest free stream mach number being equal to 0.16. The Reynolds Averaged Navier Stokes (RANS) and Large-Eddy-Simulation (LES) regions utilize bounded

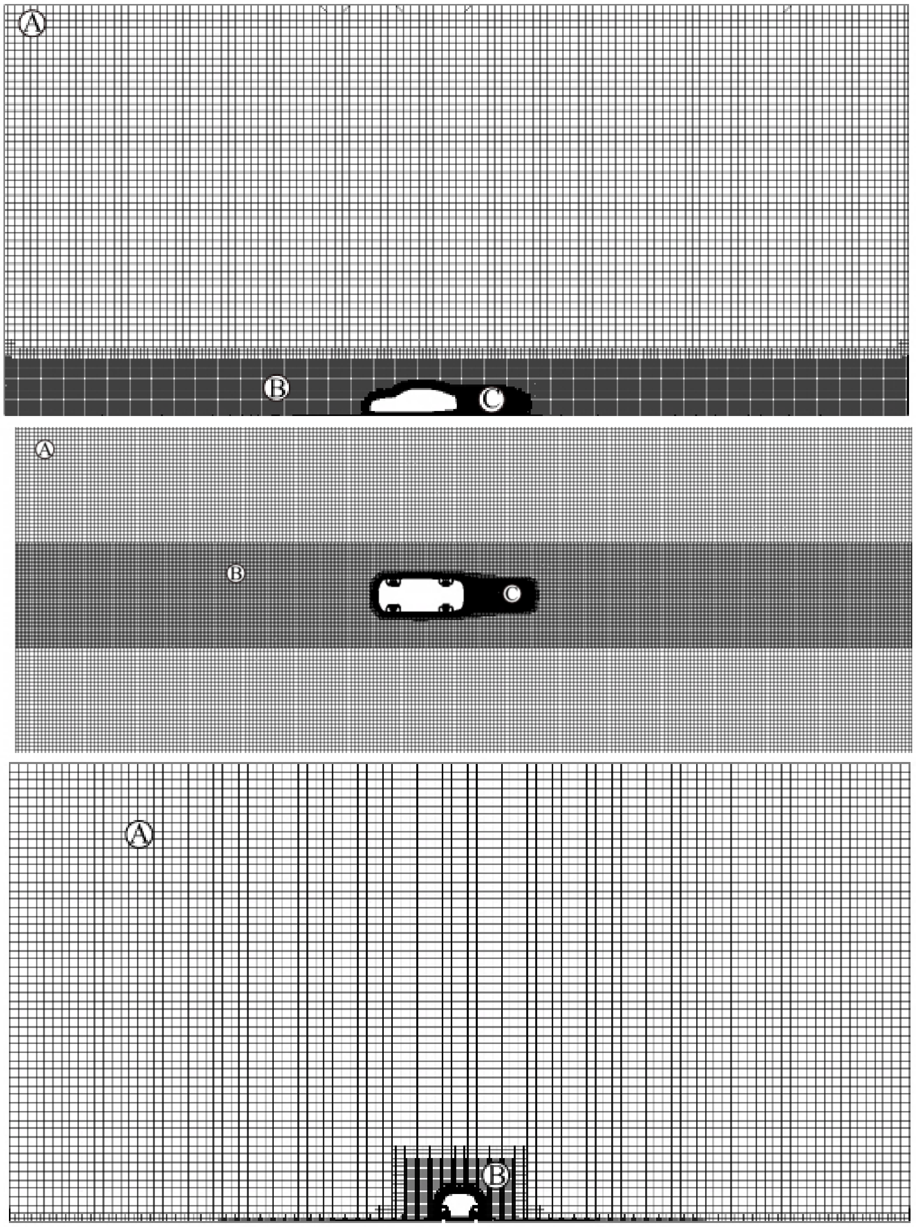

Figure 9: Near body slices of mesh for top: $Y = 0L$, middle:$Z = 0L$, bottom:$X = 0L$.

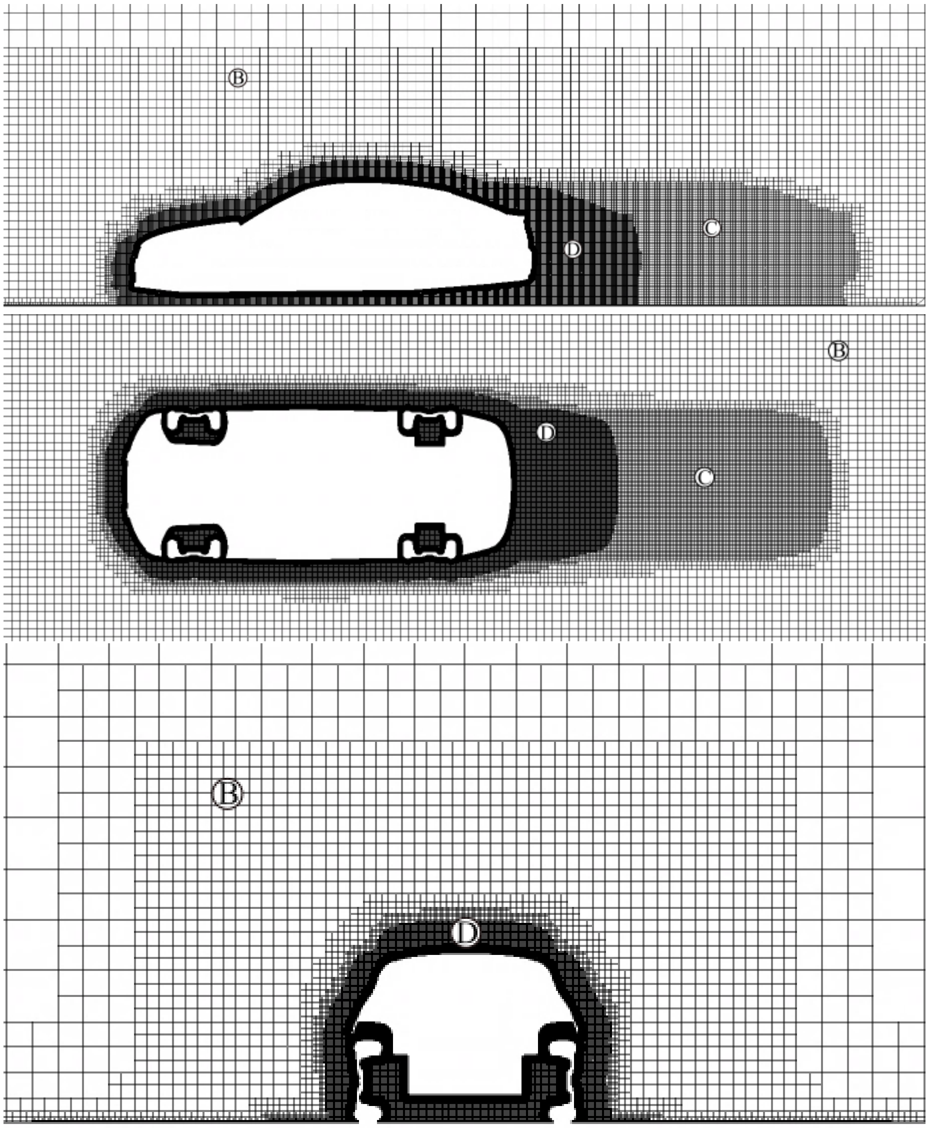

Figure 10: Near body slices of mesh for top: $Y = 0L$, middle:$Z = 0L$, bottom:$X = 0L$.

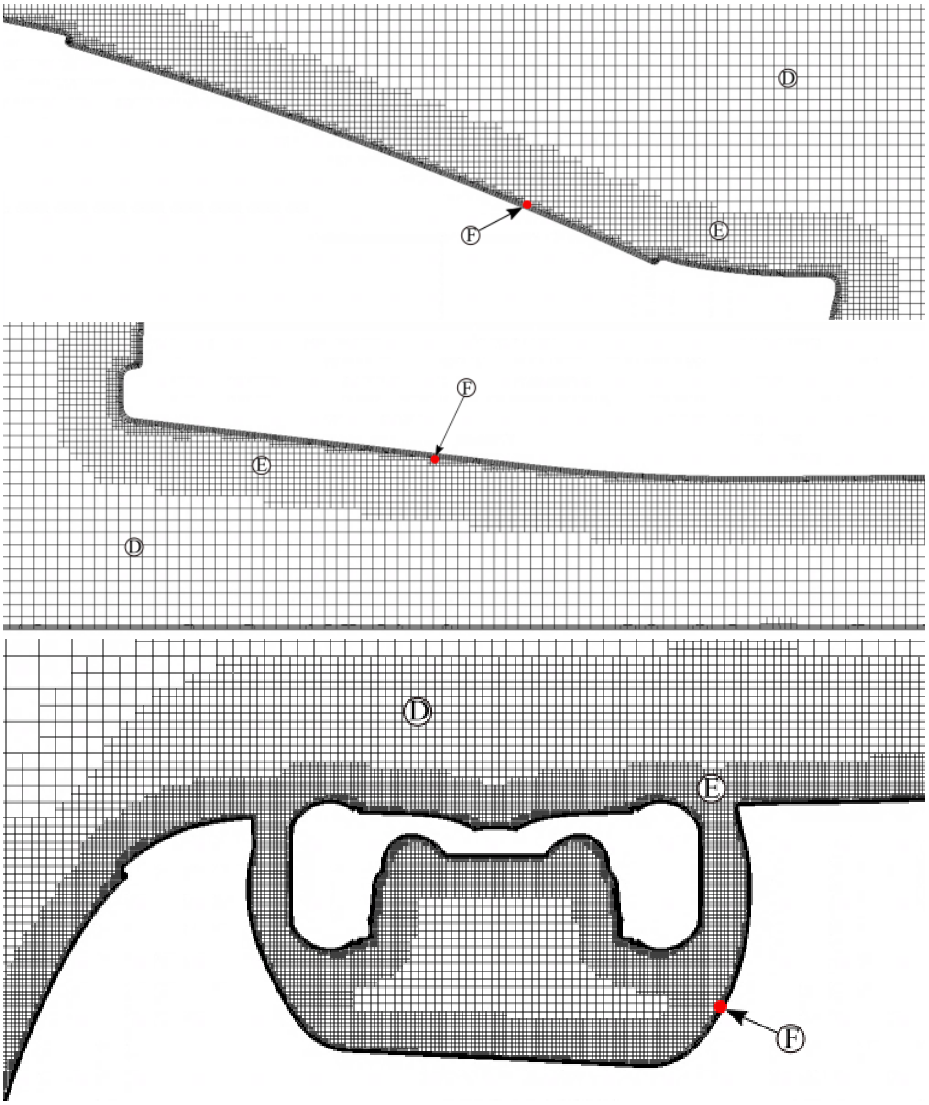

Figure 11: Detail slices of mesh for top: $Y = 0L$ over the rear glass and decklid, middle:$Y = 0L$ under the bottom edge of the front fascia above the road, bottom:$Z = 0L$ at front wheel.

central differencing/coupled hybrid second-order upwind spatial schemes respectively with a first-order implicit unsteady temporal solver. During each time step, one inner iteration was used primarily to facilitate simulation throughput and save computational resources, this was also implemented during the model validation phase which concluded that overall body forces were within good agreement to experiments. The Shear Stress Transport (SST) k-ω Menter (Menter 1994) DES turbulence model was used with the IDDES transfer function to determine the LES and RANS regions. A total of 6 acceleration deceleration periods were computed on 144x2.4 GHZ Intel Xeon E5-2665 processors in 838.5 hours (120,744 CPU Hours).

4.5 DrivAer-GTR CFD Model

Once the full scale DrivAer-GTR model was created, it was scaled down to 40% of full scale. This was done for two reasons, the first being that the original DrivAer model was a 40% scale model and second, the scale model allows for a more efficient allocation of mesh for an IDDES simulation due to a smaller Reynolds number, relaxing the requirements of the Taylor microscale and less of a volume has to be occupied. Unfortunately, we would also expect this to scale down acceleration impacts, looking at the Morison Equation 2 the result of the accelerating force is likely to be directly impacted by the scale model.

Overall, the settings were equivalent to the DrivAer model acceleration explored in the previous section with a few key differences to focus on simulation efficiency. This was done primarily to take advantage of a specialized high performance computer available with 3 × 24 Intel Xeon E5-2697 processors operating at 2.7 GHz clock

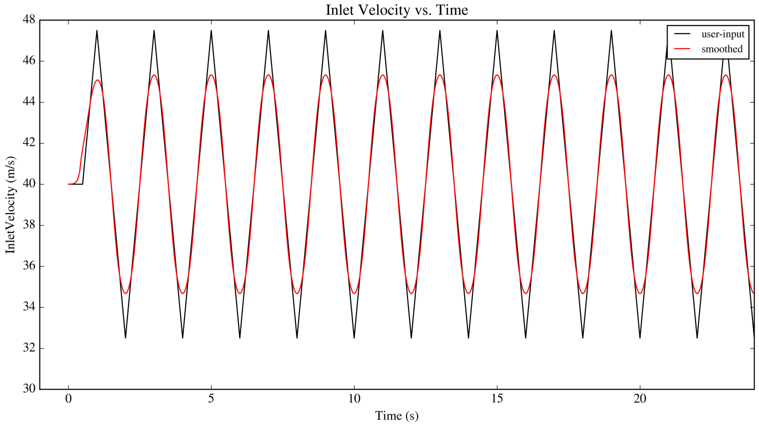

Figure 12: The DrivAer-GTR velocity inlet signal over several periods.

speed which was allocated for this dissertation. Due to the computational resource available and a targeted run time of 2 weeks, the total accel-decel periods needed to be maximized. At the time of writing this dissertation, high performance road cars and motor sports vehicles are reportedly capable of $14\,\mathrm{m\,s^{-2}}$, which is likely to be near the traction limit of the tires. Because the focus of this particular study is to investigate acceleration aerodynamics of high performance road vehicles and for the sake of simulation efficiency, an acceleration and deceleration rate of $\pm 15\ \mathrm{m\,s^{-2}}$ was selected. The rate of acceleration saves overall simulation time due to the time span of a period consuming less time. The inlet signal for the DrivAer-GTR is presented in Figure 12, where the red signal is the smoothed input generated by a Smagorinsky filter, as done in the previous two studies.

Another key difference for this simulation was the decision to increase the time step from 1×10^{-4} s to 2.5×10^{-4} s at the cost of numerical accuracy for simulation throughput. The goal was to hold the volume mesh size to under 40 million finite volume cells and was achieved at approximately 37 million. These factors resulted in

Table 4: DrivAer-GTR Grid spacing values non-dimensionalized by wheel base length L=1.114 m and exact values

Mesh Region	A	B	C	D	E
Grid Spacing/L	0.18	0.0225	0.0056	0.0028	0.0014
Grid Spacing (mm)	200	25	6.25	3.125	1.5625

an acceleration-deceleration period of 2 s which resulted in a simulated period time of approximately 28 hours.

A tunnel volume was created around the DrivAer-GTR centered at the half length between the front and rear axles with dimensions of $\pm 10 \times \pm 8 \times 5$ m with a velocity inlet upstream of the body, a floor with non-slip tangential road velocity set equal to V_{ref}, slip walls and a pressure outlet downstream of the body. All other boundaries of the DrivAer-GTR were set as non-slip walls. The same SEM model was implemented at the inlet as in the previous two studies.

The same meshing practices from the previous studies were applied by first calculating the Taylor Length scale for the 40% scale DrivAer using the wheel base length for a inlet velocity of 40 $\mathrm{m\,s^{-1}}$. This indicated that a length scale of 3 mm should be resolved to properly simulate 80% of the energy carrying eddies in the LES region. Figure 15 is a slice plane of the volume mesh at Y=0, where a volume for advecting SEM eddies from the inlet with intensity of 0.1 and length scale of 25 mm (marked as B) runs the entire length of the simulation domain with height and width of $1.25 \times \pm 1.5$ m. The primary volume to resolve bulk flow features is marked as C with mesh size of 6.25 mm and is nearly double the Taylor Length scale and occupies a smaller volume around the vehicle from -1.1X to 2.5X with a width and height of

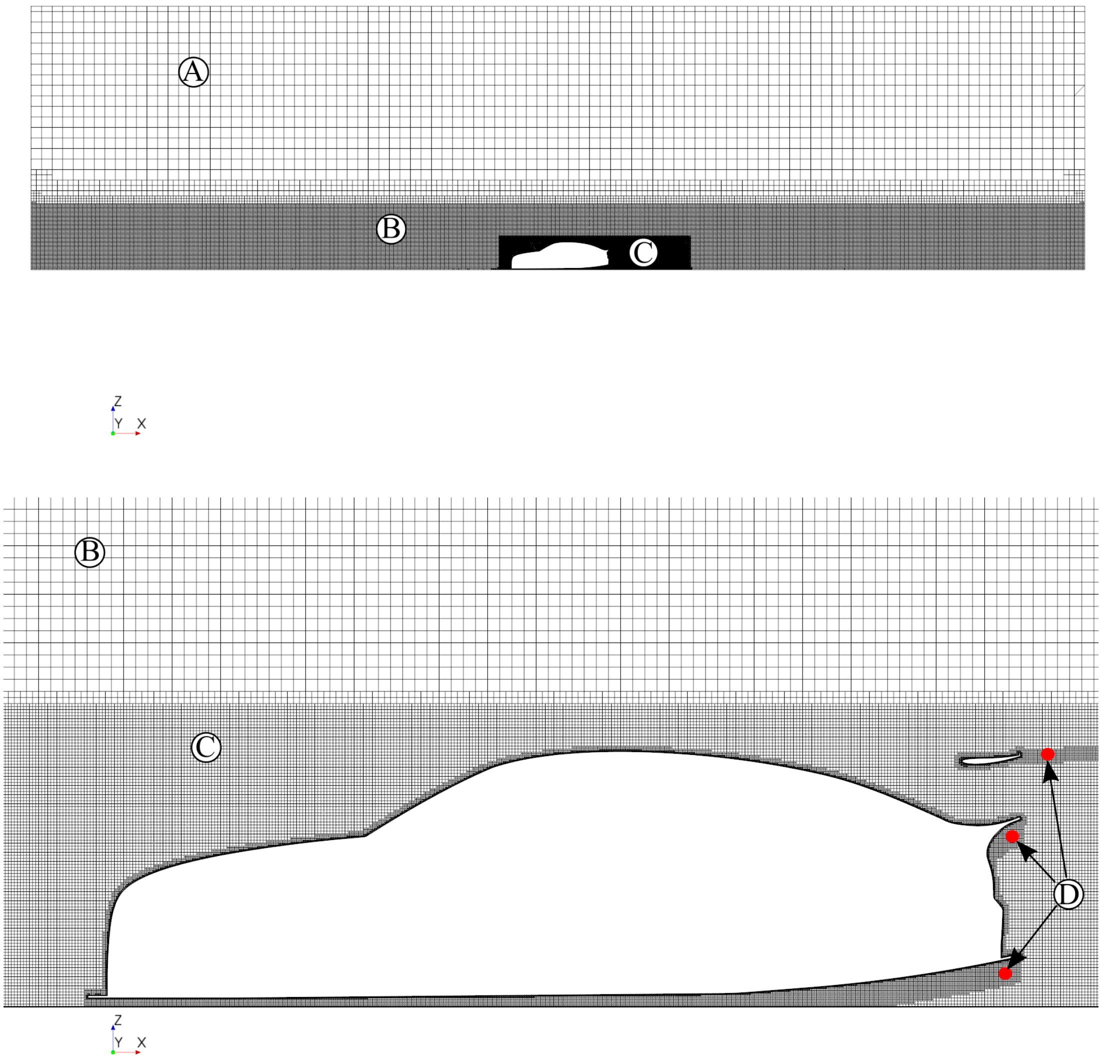

Figure 13: Overall view of the numerical grid for Y=0 (top) and Z=0.200 (bottom).

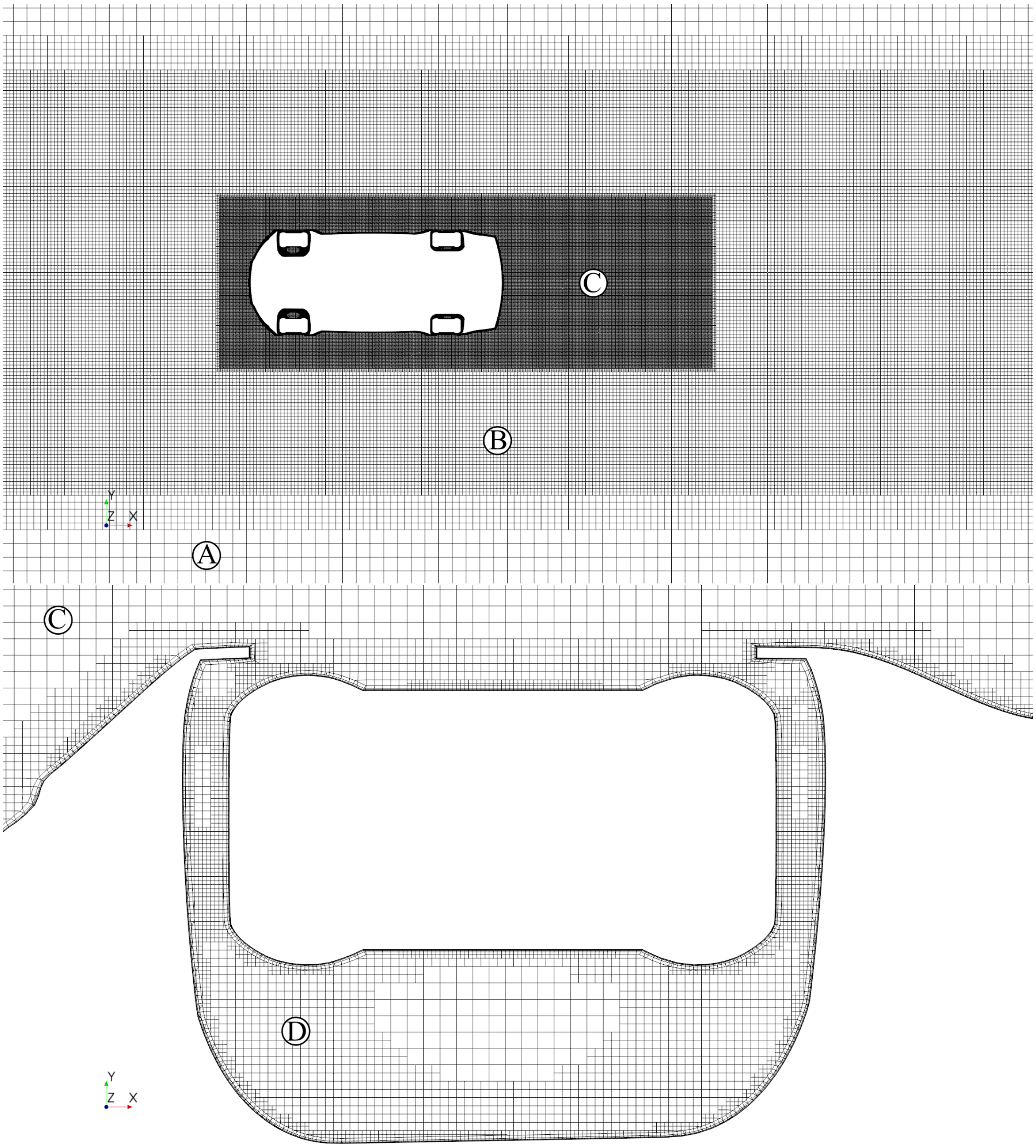

Figure 14: Overall view of the numerical grid for Y=0 (top) and Z=0.200 (bottom).

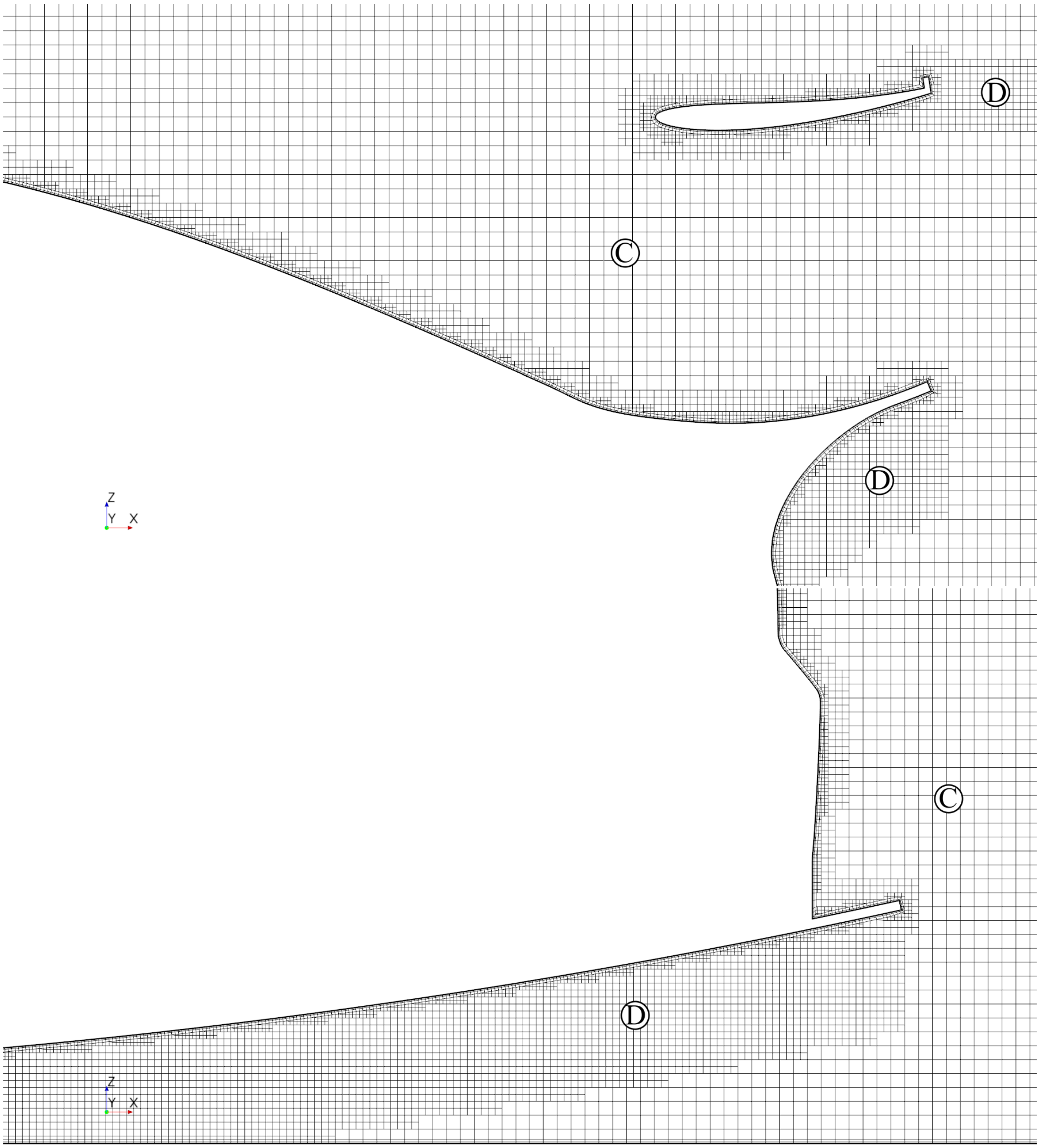

Figure 15: Overall view of the numerical grid for Y=0 at the back of the vehicle underneath the wing (top) and near the rear diffuser (bottom).

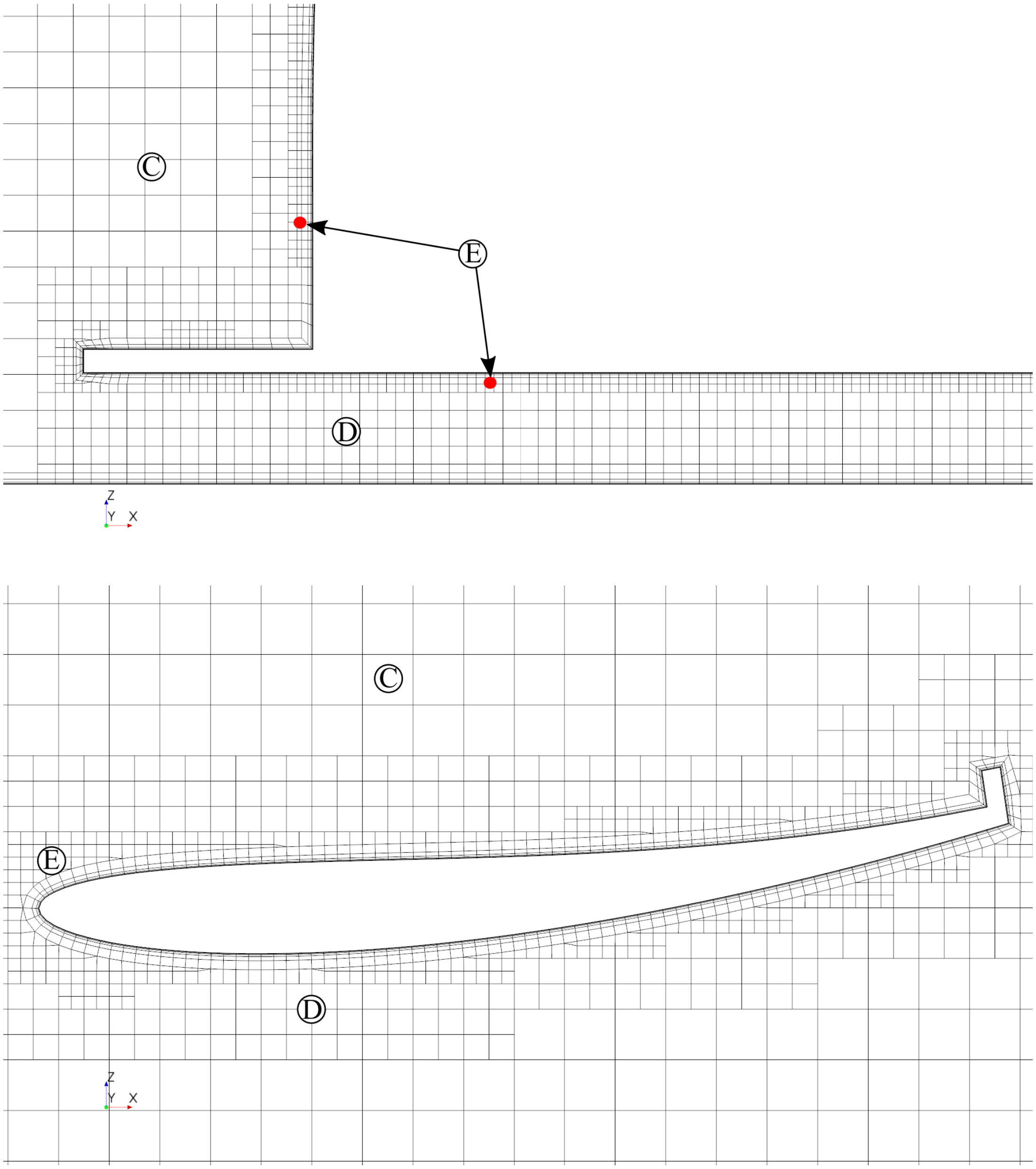

Figure 16: The numerical grid surrounding the front splitter and rear wing at Y=0.

±0.625 × 0.625 m respectively.

Figure 14 details the previously mentioned mesh regions as viewed from the top of the vehicle at a height of Z=200mm pointing out that majority of nearbody areas are surrounded by C and D mesh sizes.

Figure 15 details areas around the rear wing/spoiler area and the rear diffuser, noting that areas of anticipated smaller Taylor microscales are resolved at a D mesh level.

Figure 16 details the finest mesh levels around the front splitter and rear wing, areas where high amounts of downforce are produced. Areas resolved at level E closest to the body are set to blend between the wall normal prism layer mesh and the surrounding background mesh level of D.

Six total prism layers were used on all vehicle surfaces and the road with a first cell height of 0.02 mm and a total layer thickness of 2 mm which blended the final layer height of 1.11 mm well with the surrounding near surface background mesh is 1.56 mm.

CHAPTER 5: BLUFF BODY ACCELERATION

5.1 Introduction

Herein we focus on the differences between decelerating, constant and accelerating conditions for a square cylinder in channel flow which is achieved by periodically forcing the inlet to drive constant acceleration and deceleration rates. We choose the square cylinder as our test article due to the simplified shape creating constant separation points, eliminating unforeseen complexities in the flow field. Data was carefully ensemble averaged at a reference velocity of 6 $\mathrm{m\,s^{-1}}$ for each acceleration phase to extract flow fields and forces for comparison with steady free-stream results. This process is the critical first step to investigate unsteady race vehicle aerodynamics for development of advanced dynamic handling models.

5.1.1 Model Validation

Before attempting to simulate acceleration, a validation study was performed to replicate Lyn and Rodi[41] experimental results of constant-velocity flow past a square cylinder at $R_e = 2.1 \times 10^4$. The previously described IDDES simulation methodology, boundary conditions and mesh specifications were first implemented for model validation which predicted C_D and C_L^{rms} to be 2.22 and 1.33 respectively (drag force herein was calculated from integration of both the pressure and viscous forces). Lyn and Rodi experimentally reported $C_D = 2.1$, which they obtained through the momentum integral of laser-doppler velocimetry measured mean wake velocity profiles. The computed value of C_D from the current validation study also agrees well with reported values compiled by Trias et al.[64] of 10 seperate studies spaning experimental, LES and direct-numerical-simulations (DNS), where the C_D values for the square cylinder vary from 2.01 to 2.32 and C_L^{rms} range from 1.15 to 1.79. In a recent study, Cao and Tamura [11] experimented with the effect of grid-spacing for LES predictions of flow over a square cylinder, reporting C_D range from 2.19 to 2.24. In addition, Figure 17 shows surface pressure coefficients (C_P) at center plane along with the recent numerical LES results of Cao & Tamura [11], DNS results of Trias [64], and previous experimental results of Lee [37], Bearman & Obasaju [6] and Nishimura [47]; demonstrating that current IDDES results fall well within prior studies for pressure distribution. This further supports that the IDDES methodology adopted in this paper is producing results with an acceptable accuracy.

After the validation was performed, the process was then scaled up from an H=0.06 m to H=0.5 m in order to increase the volume of the test object. This was done for two reasons, (1) for ease of force measurements at lower Reynolds numbers, and (2) to approach the characteristic scale of an automobile. Note that the Taylor microscale and $V_{inlet}(t)$ were recalculated and scaled accordingly from validation to large scale.

5.2 Results and Discussion

Three specific flow cases were tested and compared with equivalent free-stream velocities while undergoing acceleration ($a_x > 0$), non-acceleration or constant-velocity ($a_x = 0$) and deceleration ($a_x < 0$). Acceleration and deceleration data reported

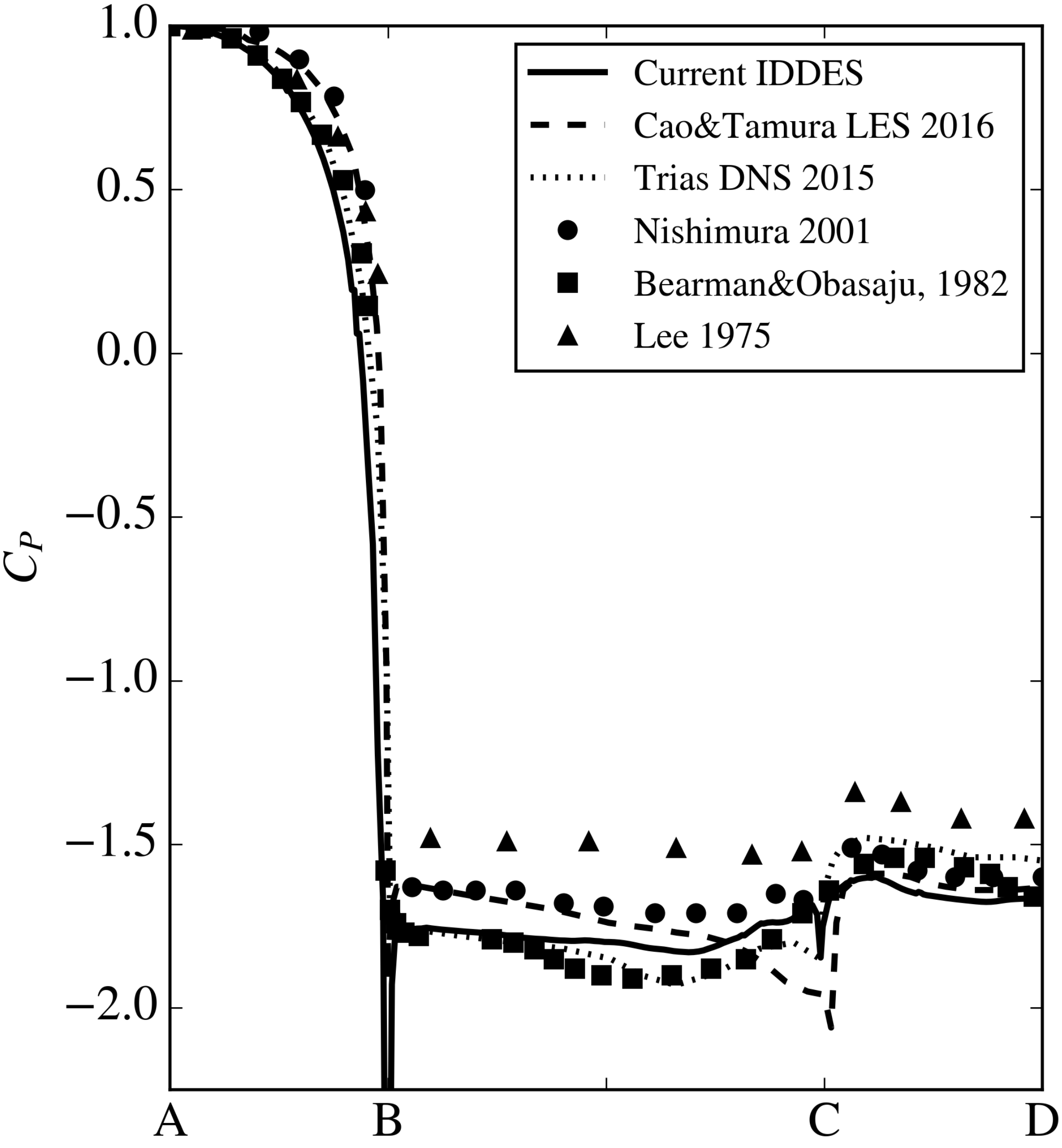

Figure 17: Surface pressure coefficient taken at center plane ($H_z^* = 0$) in comparison with highly resolved numerical computations and experiments

.

in this chapter were obtained via ensemble averaging 33 total periods while non-accelerating data was obtained by holding $V_{inlet}(t)$ constant and averaging for 18 large eddy turnover times in separate simulations; a total of three constant velocity simulations were run at 5, 6, and 7 $\mathrm{m\,s^{-1}}$. Body drag force for $a_x \neq 0$ cases was calculated by first smoothing the transient body force data and then ensemble averaging each respective accelerating or decelerating period. C_L^{rms} was obtained through segregation of C_L for each acceleration or deceleration period and then summed together across all periods and was left as the non-dimensional lift coefficient to not skew results due to $V_{ref}(t)$. Spatial ensemble averaging was utilized to obtain scalar flow field variables of Velocity (V_x^* and V_y^* non-dimensionalized by $V_{ref}(t)$) and vorticity (ω_Z^* non-dimensionalized by $\frac{V_{ref}(t)}{H}$) at $V_{ref} = 6\ \mathrm{m\,s^{-1}}$. Due to the unsteady mean free stream velocity, the overall drag force is presented as a force in Table 5, this was done intentionally as the drag coefficient C_D is reserved for steady mean velocity flow, which is apparent in Equation 2.

5.2.1 Body Forces

Figure 18 shows the variation of the drag force as a function of velocity V_{ref} for the accelerating and non-accelerating cases for $2.5 \leq V_{ref} \leq 7.5\ \mathrm{m\,s^{-1}}$. It may appear from Figure 18 that, although positive and negative accelerations have similar impacts on the drag force for $V_{ref} = 6\ \mathrm{m\,s^{-1}}$, the effect of one is more dominant than the other depending on V_{ref} larger or smaller than 6 $\mathrm{m\,s^{-1}}$; for example, the positive acceleration appears to have a larger effect on drag for $V_{ref} < 6\ \mathrm{m\,s^{-1}}$, and vice versa. This may be deceiving as this study was created to focus on the 6 $\mathrm{m\,s^{-1}}$ velocity,

Table 5: Ensemble averaged Drag Force, rms Lift Coefficient, and inertial coefficient C_M at $V_{ref} = 6\ \mathrm{m\,s^{-1}}$ for the square cylinder during $a_x = -2G$, $a_x = 0$ and $a_x = 2G$.

a_x	Drag (N)	C_L^{rms}	C_M
$-2G$	37.5	1.95	1.91
0	71.4	1.33	-
$2G$	102.9	0.52	1.77

and the inlet velocity $V_{inlet}(t)$ was forced to vary between 0.5 and 11.5 $\mathrm{m\,s^{-1}}$. The closer we get to the inflection velocity ($\partial V_{inlet}/\partial t$ changes sign) i.e. further away from the mid-point velocity, the artifacts from velocity inflection may influence the results one way or the other. In support of this, Figure 3 demonstrates that the inflection velocity occurs near 5 and 7 $\mathrm{m\,s^{-1}}$. By non-dimensionalizing the body force by V_{ref}^2 in Figure 19 the effect of the inflection velocity from the inlet signal is evident, where at $V_{ref} = 6\ \mathrm{m\,s^{-1}}$ the acceleration deceleration forces are nearly symmetrical and are skewed about the non-accelerating force at 5 and 7 $\mathrm{m\,s^{-1}}$. This further demonstrates that focus should be upon data at the intended reference velocity. Data presented in Table 5 clearly indicates drag force deviations of -47% and +44% from the $a_x = 0$ case for the $a_x = -2G$, and $a_x = 2G$ cases respectively, all at $V_{ref} = 6\ \mathrm{m\,s^{-1}}$. C_L^{rms} values are also presented in Table 5 where the decelerating C_L^{rms} value of 1.92 is 44% larger than the non-accelerating flow and nearly four times larger than the accelerating case. These are interesting phenomenon and will be discussed further in section 5.2.2.

The inertial coefficient C_M was calculated from Equation 2 by setting part 2 of the equation equal to the non-accelerating drag force, and $Fx(t)$ equal to ensemble averaged acceleration and deceleration forces, resulting in C_{Md}=1.91 and C_{Ma}=1.77 for the decelerating and accelerating conditions respectively. The discrepancy in the

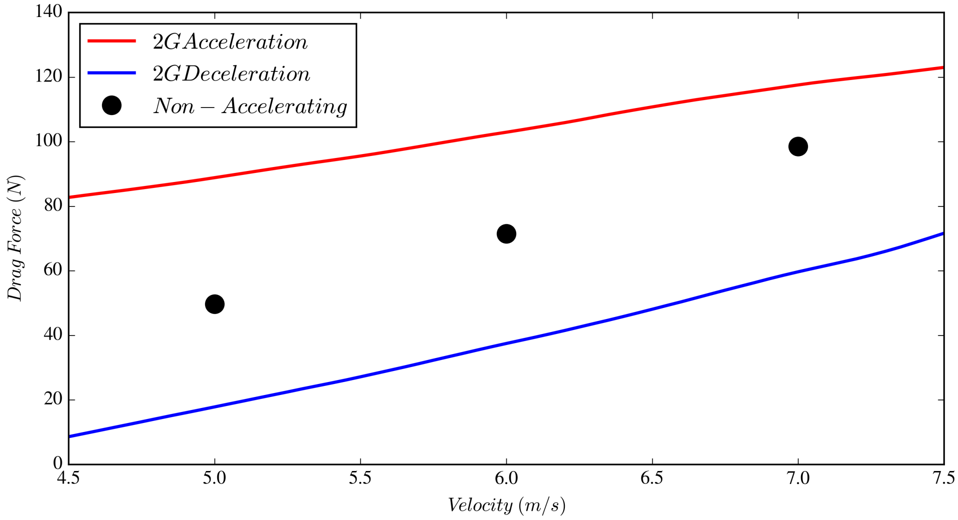

Figure 18: Drag force on the cylinder versus V_{ref} for the decelerating, non-accelerating and accelerating cases.

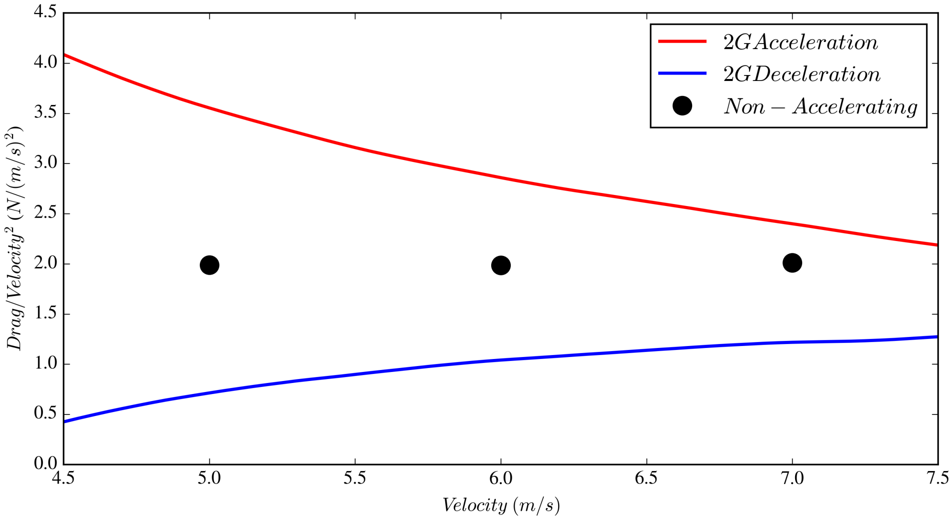

Figure 19: Drag force on the cylinder versus V_{ref}, non-dimensionalized by ${V_{ref}}^2$ for the decelerating, non-accelerating and accelerating cases.

added viscous coefficients for decelerating and accelerating flow conditions (approximately 8%) is an interesting phenomenon, yet may be small enough to approximate as equivalent for vehicle dynamics modeling purposes. These discrepancies could be attributed to the body's vorticity contribution affecting wake dynamics (vortex shedding). At this time there is no information to support whether or not this discrepancy would be present at higher reynolds numbers or different acceleration rates, insinuating that Equation 2 may require additional degrees of freedom to accurately model acceleration at varying Reynolds numbers.

5.2.2 Wake Structure

To investigate the viscous impacts of acceleration, several flow field quantities will be discussed. First, Figure 20 shows ensemble averaged streamlines bounded to the center line plane of the channel ($H_Z^* = 0$) at a reference velocity of 6 $\mathrm{m\,s^{-1}}$ corresponding to the cases $a_x > 0$, $a_x = 0$, and $a_x < 0$. Discernible differences can be observed between the accelerating (red), non-accelerating (or constant-velocity black), and decelerating (blue) cases. Obviously, the three cases exhibit starkly different wakes. Besides this, the most noticeable differences can be observed with regard to the location and size of the leading edge vortex. The accelerating case has the smallest leading edge separation bubble with its center located at $H_x^* \approx -0.25$, and the recirculation at the rear of the cylinder is contained within $H_x^* \approx 1$. In addition, this case shows a reattachment of the leading edge separation on the cylinder surface making the rear recirculation in the cylinder wake clearly detached from the one off of the leading edge. Arguably, between the top and bottom vortices, the top one seems to be more dominant than the bottom one for this ensemble, and its center is slightly further upstream than the one on bottom. Compared to the accelerating case, the constant-velocity case has a larger leading edge recirculation with the center located further downstream and, at least, the top vortex is biased more towards the trailing edge. No flow reattachment on the cylinder surface is observed. The rear wake shows the presence of two alternating vortices of almost equal strength. The decelerating case has the largest leading edge separation and unlike the other two cases, the leading edge and rear re-circulations are somewhat merged.

The asymmetry in the ensemble averaged streamlines should not be confused with phase-averaging techniques employed by Lyn and Rodi [40], Cantwell and Coles [10] and others which were done to obtain ensemble averages of discrete vortex-shedding phases. The authors propose that the asymmetry is merely due to a slight deficiency of ensemble averaging, causing a visible shift in both the decelerating and accelerating wakes. Computational resources provided 33 total periods for this study where Cantwell and Coles obtained more than 1.6×10^4 rotations at each position for their flying hotwire probe to obtain a complete phase-averaged data set. Higher C_L^{rms} values indicate that an ideal ensemble averaged flowfield for the decelerating case could require significantly more periods than the other two cases. Further yet, ensemble averaged vorticity scalars presented in Figure 28 appear as expected for a global mean (see Cantwell Coles [10] Figure21:(a)) and do not appear to be an ensemble of constant phase (see Cantwell Coles [10] Figure21:(b)). Nonetheless, the authors cannot deny the streamline asymmetries observed in Figure 20 but will carry on with further analysis and recommend this for future investigation when computational resources

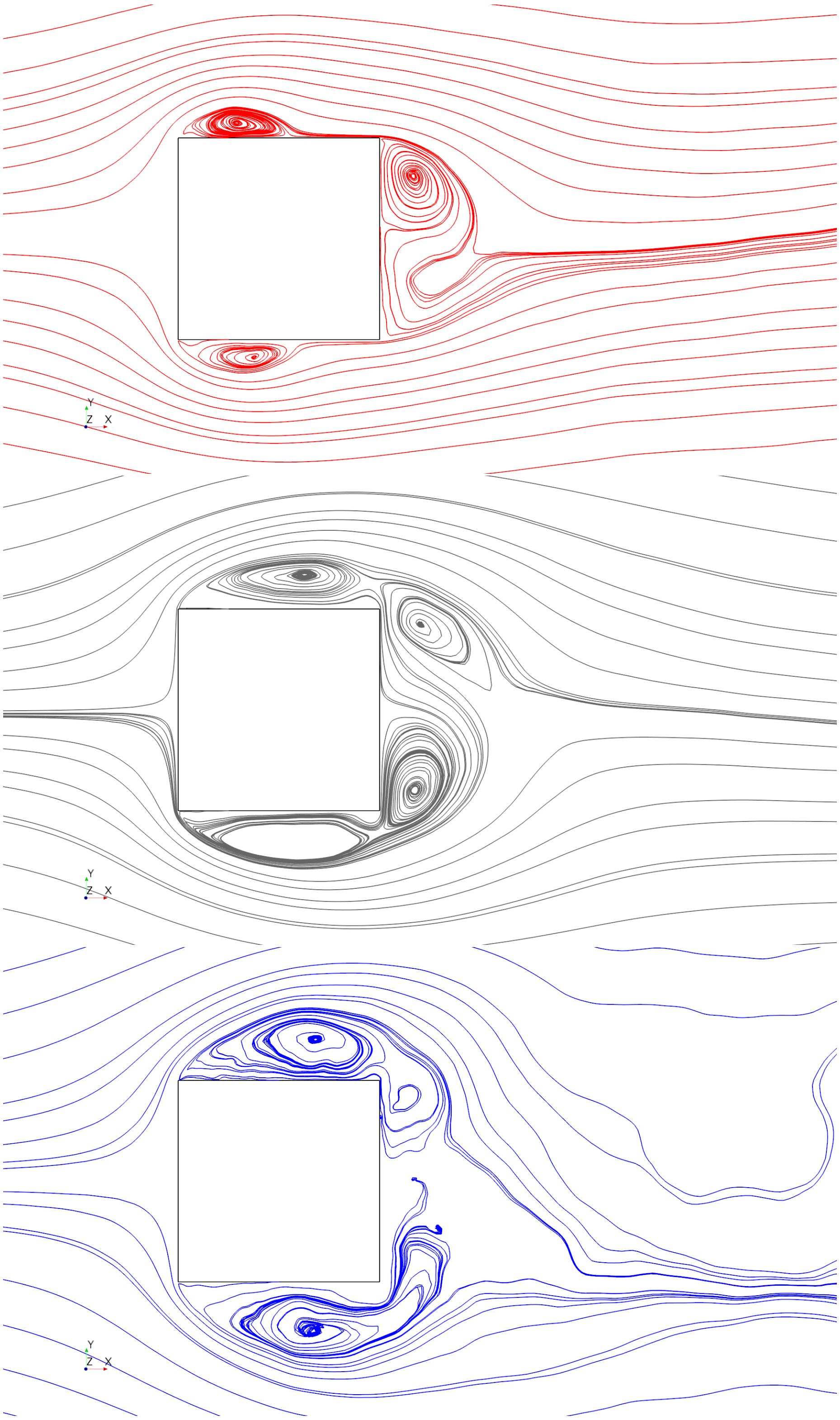

Figure 20: Streamlines at cylinder center plane for $a_x > 0$ (top), $a_x = 0$ (middle) and $a_x < 0$ (bottom).

allow such.

Another method for quantifying variations in the near body flow field is through the bow wake flow angle in the xy plane. This demonstrates the strength of the leading edge separation between the three cases and can be seen in Figure 22 where ensemble averaged data was sampled along $(-0.25H, H_y^*, 0)$ (see Figure 21) at the leading edge of the cylinder. As expected, the flow angle is orthogonal to the x-axis directly in front of the cylinder and when H_y^* is ± 1, flow angles are approximately 27°,20° and 12° for decelerating, non-accelerating and accelerating cases. The accelerating and non-accelerating cases have equivalent flow angle in the bow wake at approximately $H_y^* = 1.5$, and some asymmetry is also present in the accelerating bow wake, this is likely due to noise in the ensemble averaging process. The variations in bow and downstream wakes are also apparent in Figure 23 where V_x^* scalars and deltas clearly show that the accelerating case experiences reattachment on the sides of the cylinder and higher values of stream-wise velocity in the wake.

To complement these observations in further detail, ensemble averaged probe data was taken perpendicular to stream-wise flow at $H_x^* = [\pm 0.5, \pm 0.25, 1.00]$ and is clearly labeled in Figure 21. Wall-normal variations of V_x^* and V_y^* near the cylinder are presented in Figure 25, where a smaller bow wake is evident for the accelerating case at $H_x^* = -0.25$. In addition, V_x^* has a negative component close to the wall indicating reversed flow and V_y^* components are significantly smaller in comparison to other cases. At $H_x^* = 0.25$ the accelerating case appears to be nearly attached to the side walls of the cylinder as $V_x^* = 1$ within $H_x^* \pm 0.1$. V_y^* is small at $H_x^* = 0.25$ however the non-accelerating and decelerating cases appear to be predominately aligned with

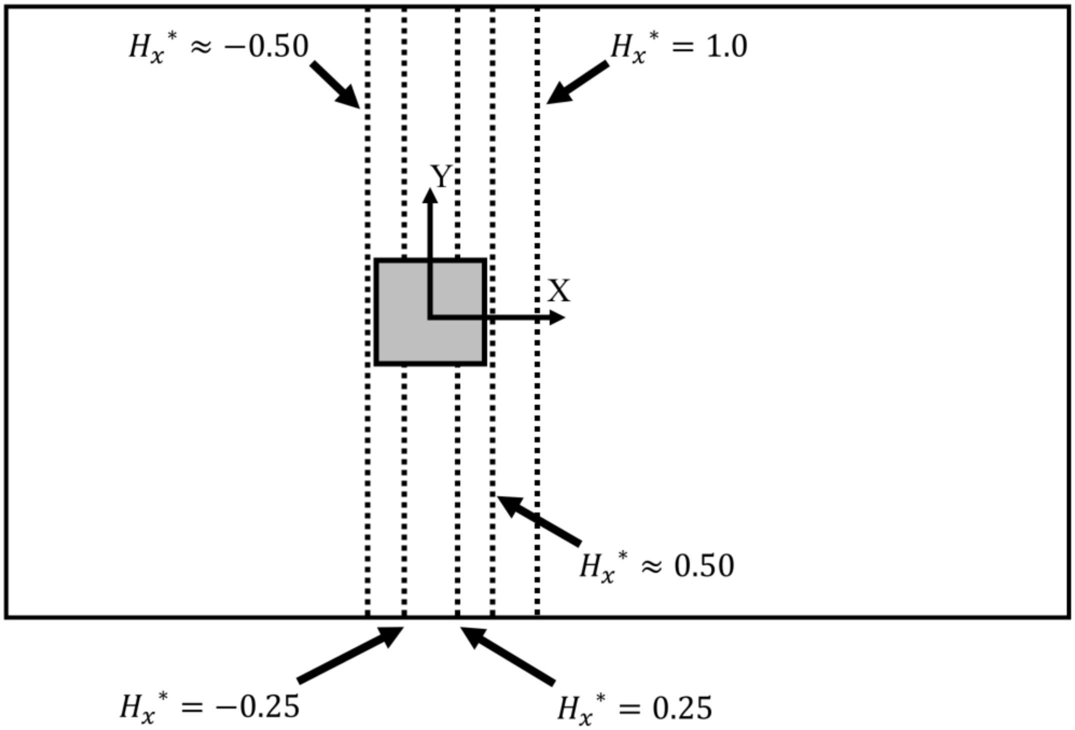

Figure 21: Locations of the three probe rakes reported. Note that dimensions are not to scale

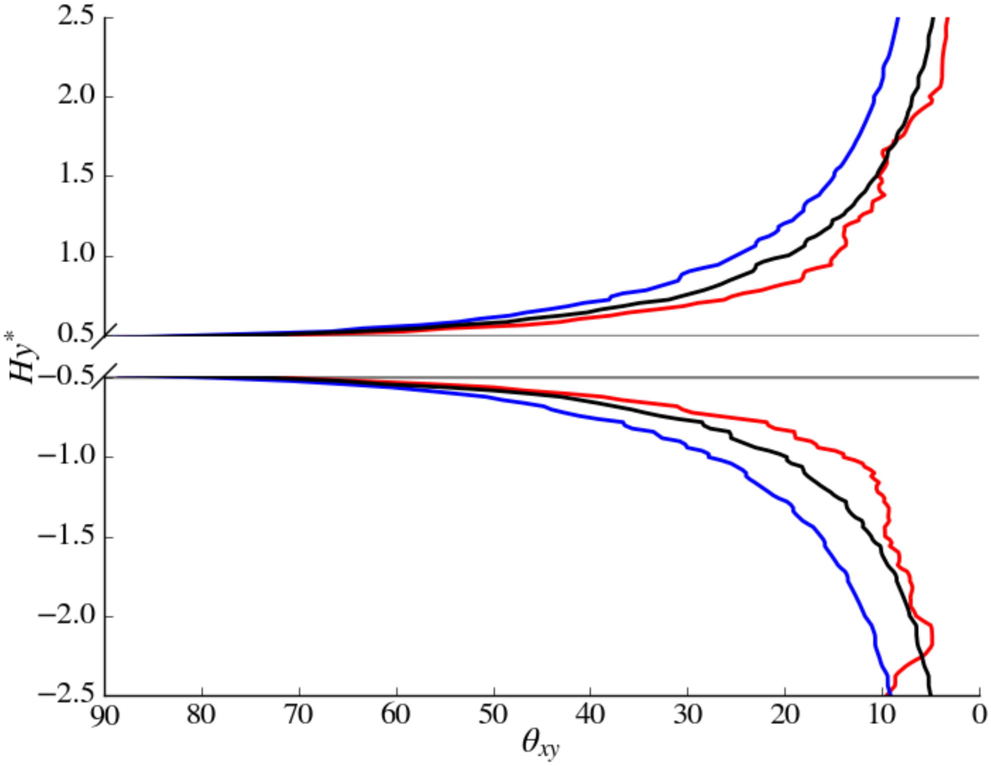

Figure 22: Ensemble averaged flow angle infront of the cylinder at $(-0.5H, H_y^*, 0)$ computed from V_x^* and V_y^*. The red, blue and black lines represent $a_x > 0$, $a_x < 0$ and $a_x = 0$ cases respectively.

the free-stream at this location while the accelerating case has a tendency towards the cylinder. In the wake behind the cylinder (see Figure 26) the smaller accelerating wake is apparent at $H_x^* = 0.5$ where values of $V_x^* = 1$ are found very close to the cylinder walls. The decelerating wake size in comparison to the non-accelerating case is more apparent further down stream of the cylinder at $H_x^* = 1$ for V_x^*. Asymmetry of the wake is present in V_y^* for both the accelerating and decelerating cases biased towards the bottom of the cylinder, although the accelerating asymmetry does appear to be smaller.

Figure 28 shows that during acceleration there is a reduction in overall vorticity, while during deceleration there is an increase. This change in overall vorticity near the cylinder can be explained through flux density of vorticity at the cylinder surface, initially demonstrated by Morton [46] and recently applied by Konstantinidis and Bouris [34] to describe vortex patterns in the wakes of oscillating cylinders via Equation 28 where; $\hat{\omega}$ is the vorticity vector, $\boldsymbol{n}$ is the surface-normal unit vector, p is the pressure, v is the kinematic viscosity and V is the relative velocity between the cylinder and the fluid.

$$-v(\boldsymbol{n} \cdot \nabla\hat{\omega}) = -\frac{(\boldsymbol{n} \times \nabla)p}{\rho} - \boldsymbol{n} \times \frac{dV}{dt} \tag{28}$$

Investigation of Equation 28 indicates that the vorticity flux density is dependent on both tangential pressure gradient and free stream acceleration. The former contribution is present for $a_x = 0$ and the latter either decreases or increases the contribution of vorticity for $0 < a_x$ and $a_x < 0$ respectively. Vorticity scalars in Figures

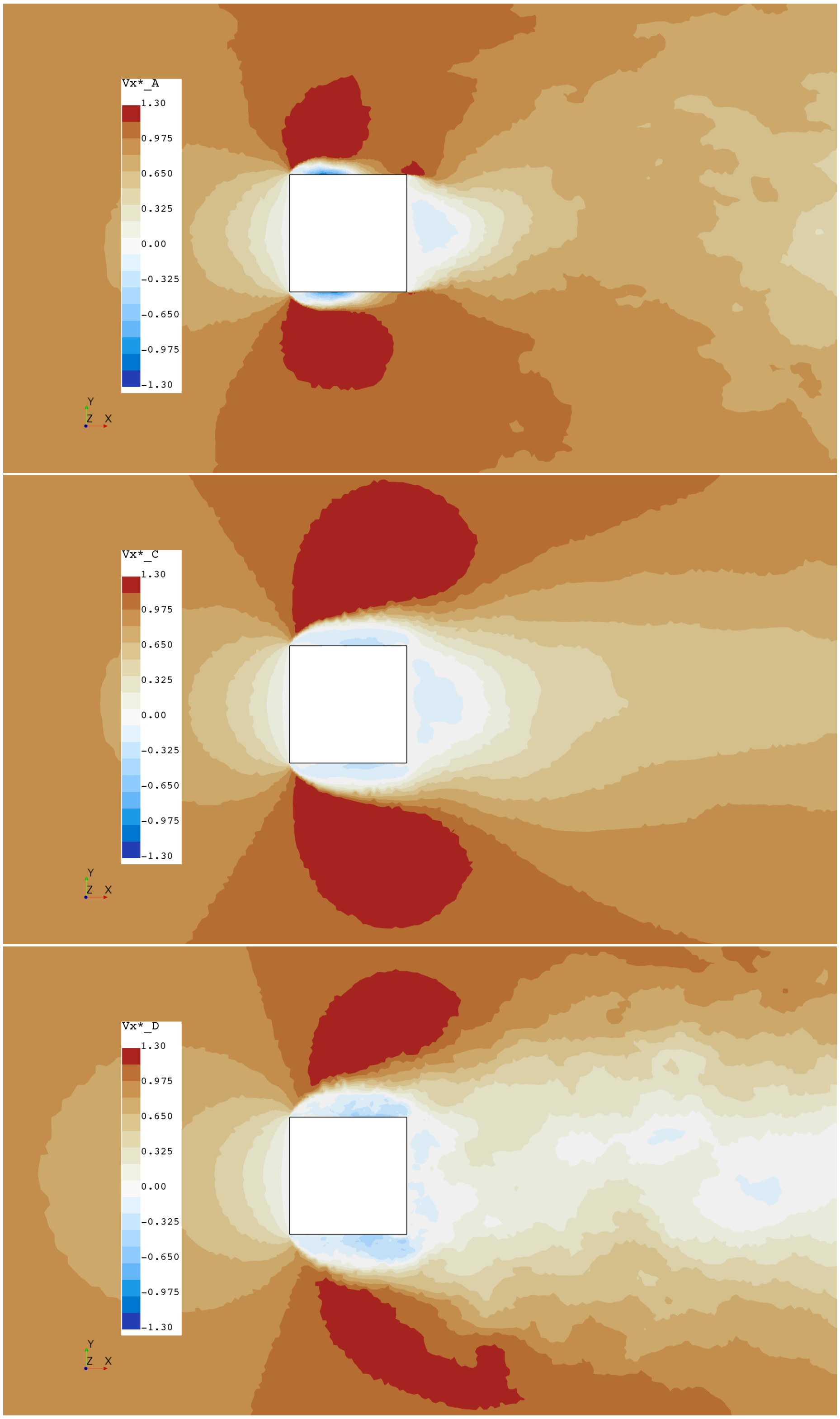

Figure 23: V_x^* scalar fields at cylinder centerline of $a_x > 0$ (top), $a_x = 0$ (middle), $a_x < 0$ (bottom).

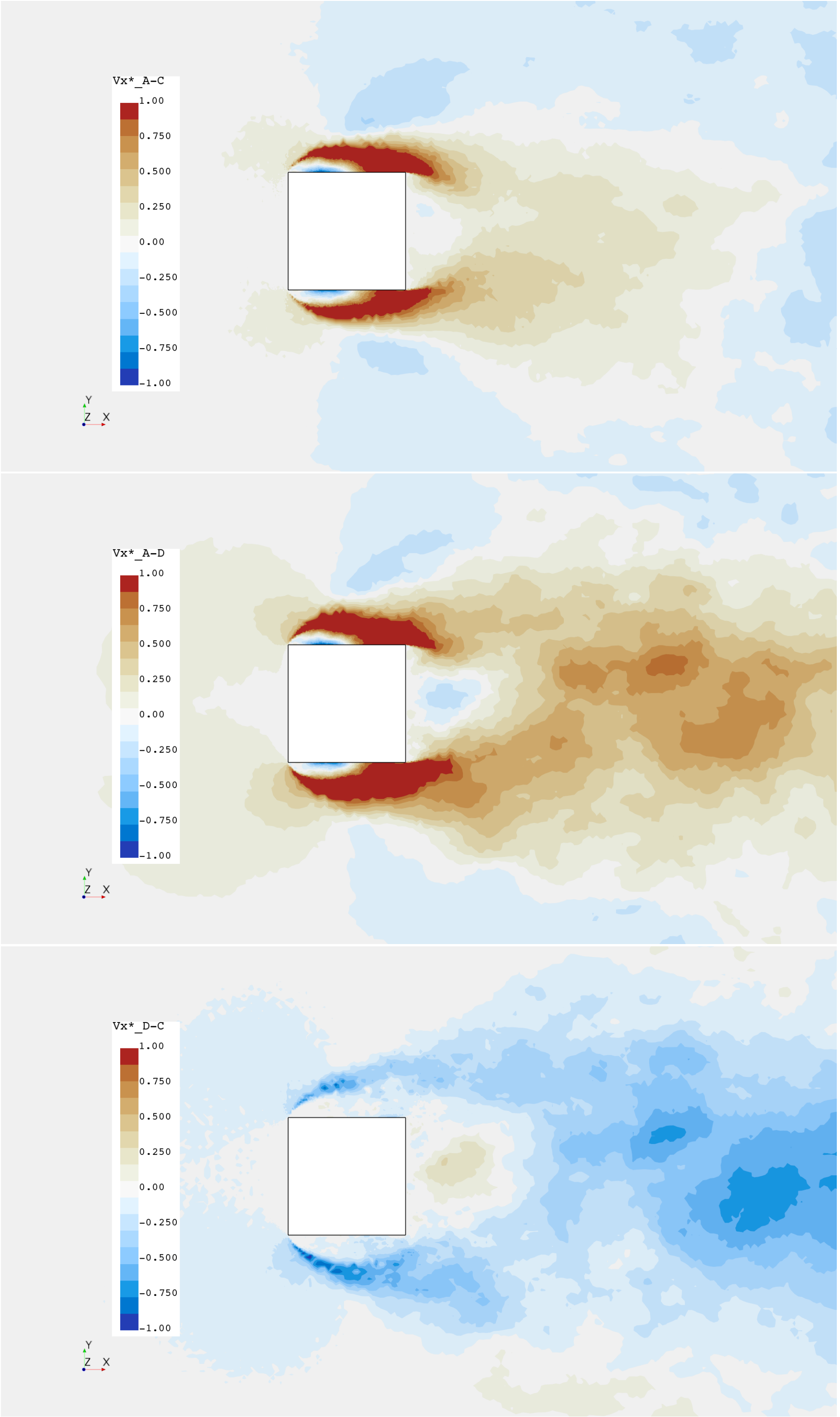

Figure 24: V_x^* deltas at cylinder centerline of $(a_x > 0) - (a_x = 0)$ (top), $(a_x > 0) - (a_x < 0)$ (middle) and $(a_x < 0) - (a_x = 0)$ (bottom)

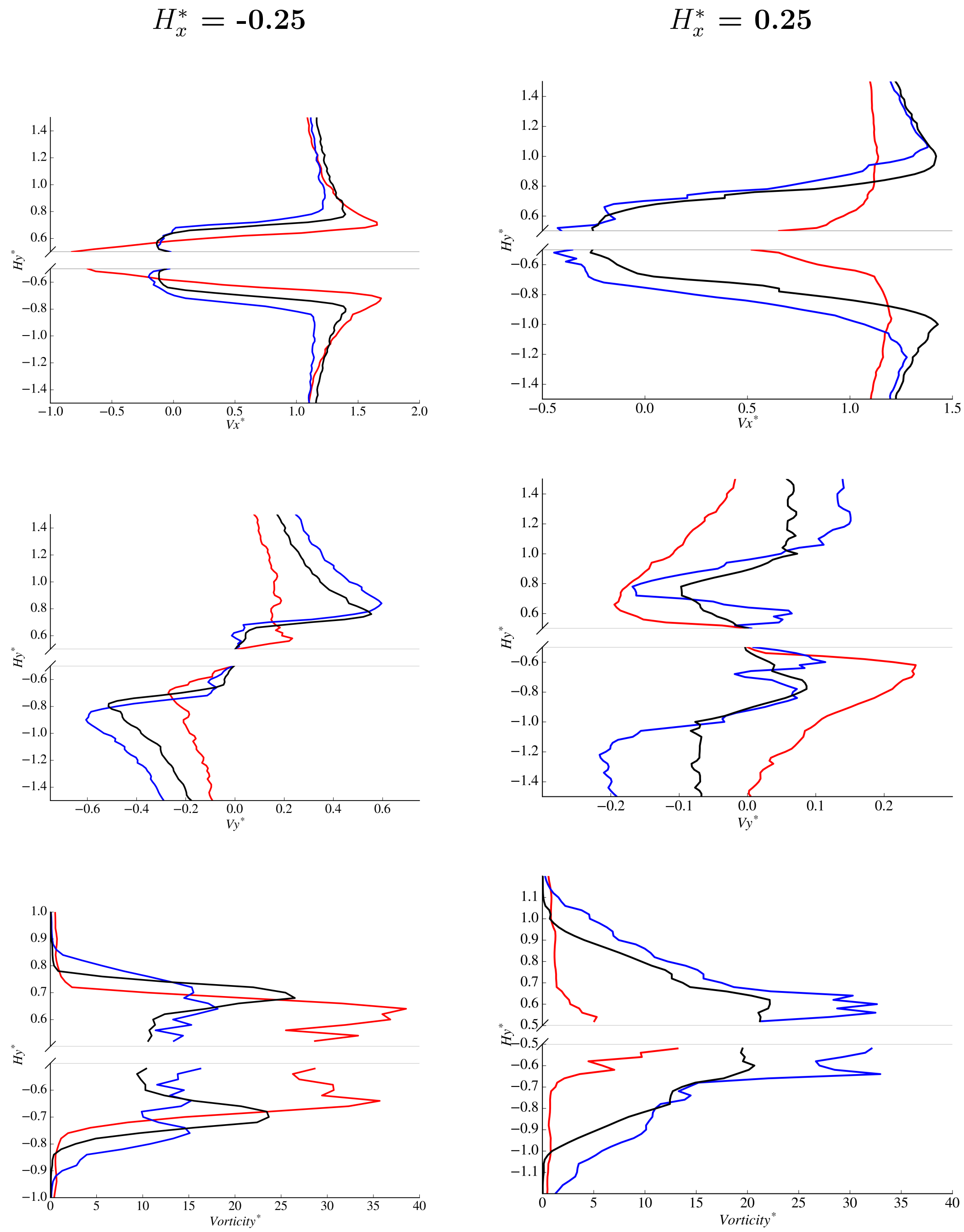
H_x^* = **-0.25**

H_x^* = **0.25**

Figure 25: Wall-normal variations of: (Top) non-dimensional streamwise velocity, V_x^*, (Middle) non-dimensional cross-stream velocity V_y^*, and (Bottom) non-dimensional vorticity magnitude $|\omega|^*$ at probe locations H_x^* = -0.25 (left), 0.25 (right). The red, blue and black lines represent $a_x > 0$, $a_x < 0$ and $a_x = 0$ cases respectively.

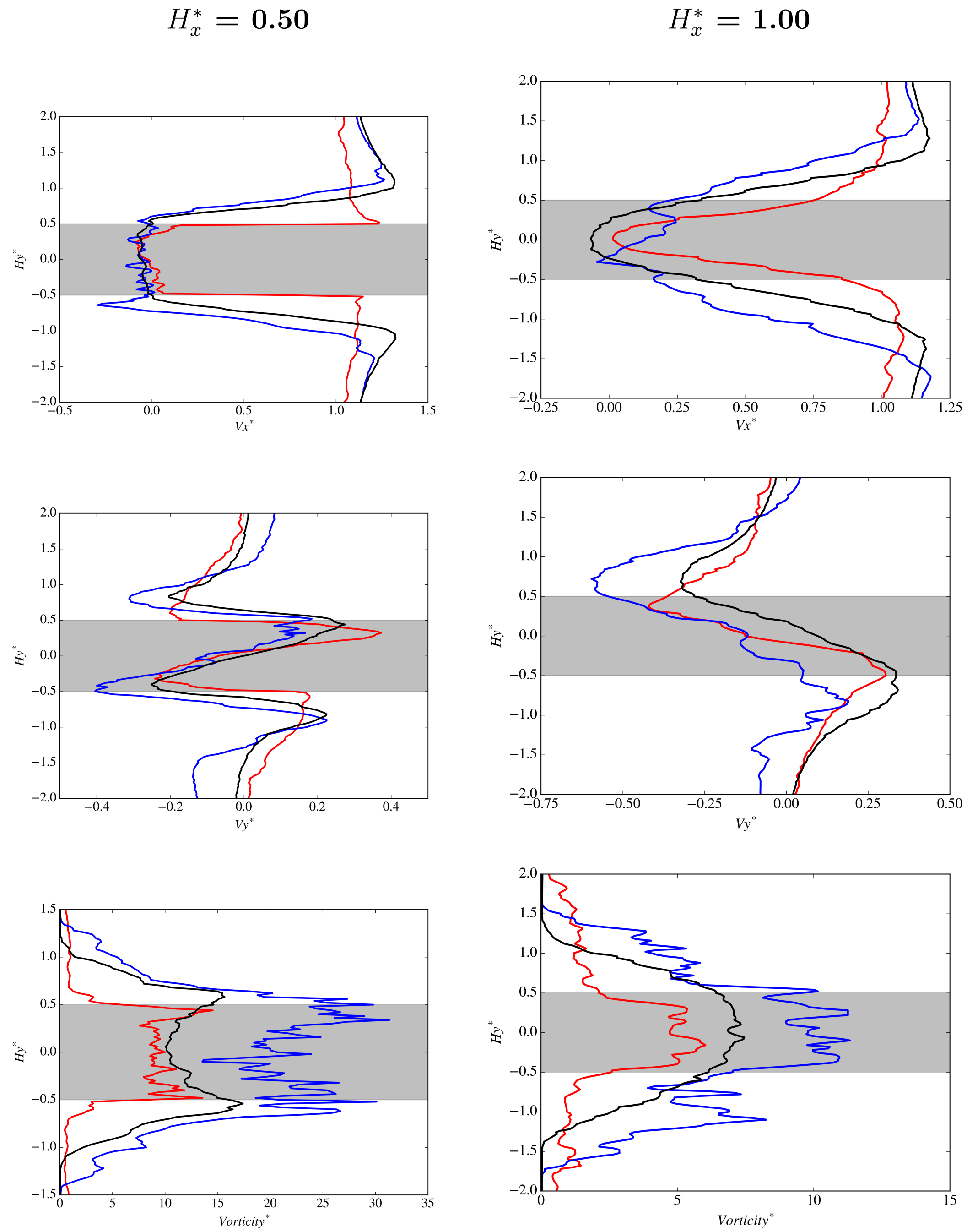

Figure 26: Wake variations of: (Top) non-dimensional streamwise velocity, V_x^*, (Middle) non-dimensional cross-stream velocity V_y^*, and (Bottom) non-dimensional vorticity magnitude $|\omega|^*$ at probe location $H_x^* = 0.50$. The red, blue and black lines represent $a_x > 0$, $a_x < 0$ and $a_x = 0$ cases respectively.

29 and Figure 28 support this notion where $0 < a_x$ has significantly less vorticity near the $\boldsymbol{n} =< 0, \pm 1, 0 >$ faces of the cylinder and $a_x < 0$ has a significant increase in vorticity. The $\boldsymbol{n} =< 1, 0, 0 >$ downstream face of the cylinder also sees changes in vorticity during each case and is linked to the first component of Equation 28 through the variation of C_L^{rms} for each respective case. During $0 < a_x$, C_L^{rms} was significantly lower, thus the magnitude of vorticity on the downstream surface is lower while $a_x < 0$ experienced the opposite effect. Only half of the vorticity generated at the wall ends up downstream in the Kármán vortices as indicated by Griffin and Ramburg[21] and Figure 28 deltas show that only $\pm|\omega|^* \approx 5$ occur downstream of the cylinder between cases.

Wall-normal variations of vorticity near the cylinder at $H_x^* = -0.25$ in Figure 25 may seem to contradict Equation 28, but the increase of vorticity in the region for the accelerating case is merely due to a stronger leading edge circulation at this location. At $H_x^* = 0.25$ wall-normal vorticity distributions support Equation 28 with a reduction of vorticity for the accelerating case and an increase for the decelerating case. In the wake, Equation 28 continues to be supported with a reduction in ensemble averaged vorticity directly behind the cylinder at $H_x^* = 0.5$ for the accelerating case and an increase for deceleration.

The formation region which was defined by Bloor [7] as the point closest to the test object at which oscillating downstream wake characteristics are still detected by hot-wire. This is also the point where flow outside of the wake first crosses the x-axis, drawn cross-stream by the formation of vortices near the cylinder. According to Gerrard [20], the size of the formation region is governed by an equilibrium of entrainment into the shear layer and reversed flow replenishing free stream fluid towards the cylinder.

Figure 30 is a cartoon of vorticity (wavy grey area), vortex core locations (depicted as circles) and entrainment (direction depicted as arrows) during a single vortex oscillation phase. This cartoon was inspired by cartoons from both Cantwell and Coles, and Gerrard; and drawn by digitally overlaying CFD results, liberties were taken to aid in explaining flow features. The lines connecting each vortex represent filament lines to visualize the growing and shrinking of shear layers between each vortex oscillation.

This leads us to apply the previously discussed formation region mechanisms to the accelerating flow case. During acceleration of the free stream velocity, vortex 1 in Figure 30 should have a higher x-component of velocity than vortex 7 compared to the non accelerating case. Each successive vortex that is created during acceleration will have a higher x-component velocity which should cause the vortices to stack up on one another along the x-axis. In addition to this, less vorticity is created by the body (see Equation 28) and lower C_L^{rms} indicates less free stream flow crossing the x-axis near the body, provoking instability downstream of the cylinder. The accelerating cylinder has a higher drag force, yet a smaller near body wake, along with lower vorticity production. This, in conjunction with different x-component velocities of vortex cores, requires higher cross stream entrainment down stream, apparently driving every other vortex core away from the x-axis as seen in Figure 29 (indicated with an arrow).

The opposite is true for the decelerating case where vortex 1 of Figure 30 would have a lower stream-wise velocity than vortex 7 and each successive vortex created near the cylinder would have even lower stream-wise components. Near body vorticity is higher which promotes a higher C_L^{rms} value, causing the formation region and wake to be larger. Due to these factors, vortex cores remain closer to the x-axis in comparison to the accelerating case.

5.3 Concluding Remarks

This study aimed to develop a simulation technique for obtaining body forces and flow fields for a bluff body undergoing longitudinal acceleration and deceleration with an end application towards dynamic handling models of road vehicles. Oscillation of the inlet velocity via a forcing function simulated constant accelerating and decelerating free-stream conditions which were ensemble averaged over 30 discrete instances of $V_{ref}(t) = 6\ \mathrm{m\,s^{-1}}$ to obtain averaged flow fields for each respective case. In comparison to steady inlet conditions, several body force and flow field variations were observed for accelerating and decelerating conditions. First, the body drag increased 44% and decreased 47% for the accelerating and decelerating cases over steady free-stream conditions. Second, the fluctuating lift force (C_L^{rms}) decreased 60% and increased 46% during acceleration and deceleration respectively in comparison to steady free-stream conditions, indicating that complicated turbulent phenomenon were present. Third, the near-body leading edge and downstream wake were both significantly smaller during acceleration, causing reattachment of flow on the top and bottom sides of the cylinder. During deceleration, the leading edge wake grew away from the cylinder in comparison to non-accelerating flow leading to a wider wake behind the cylinder.

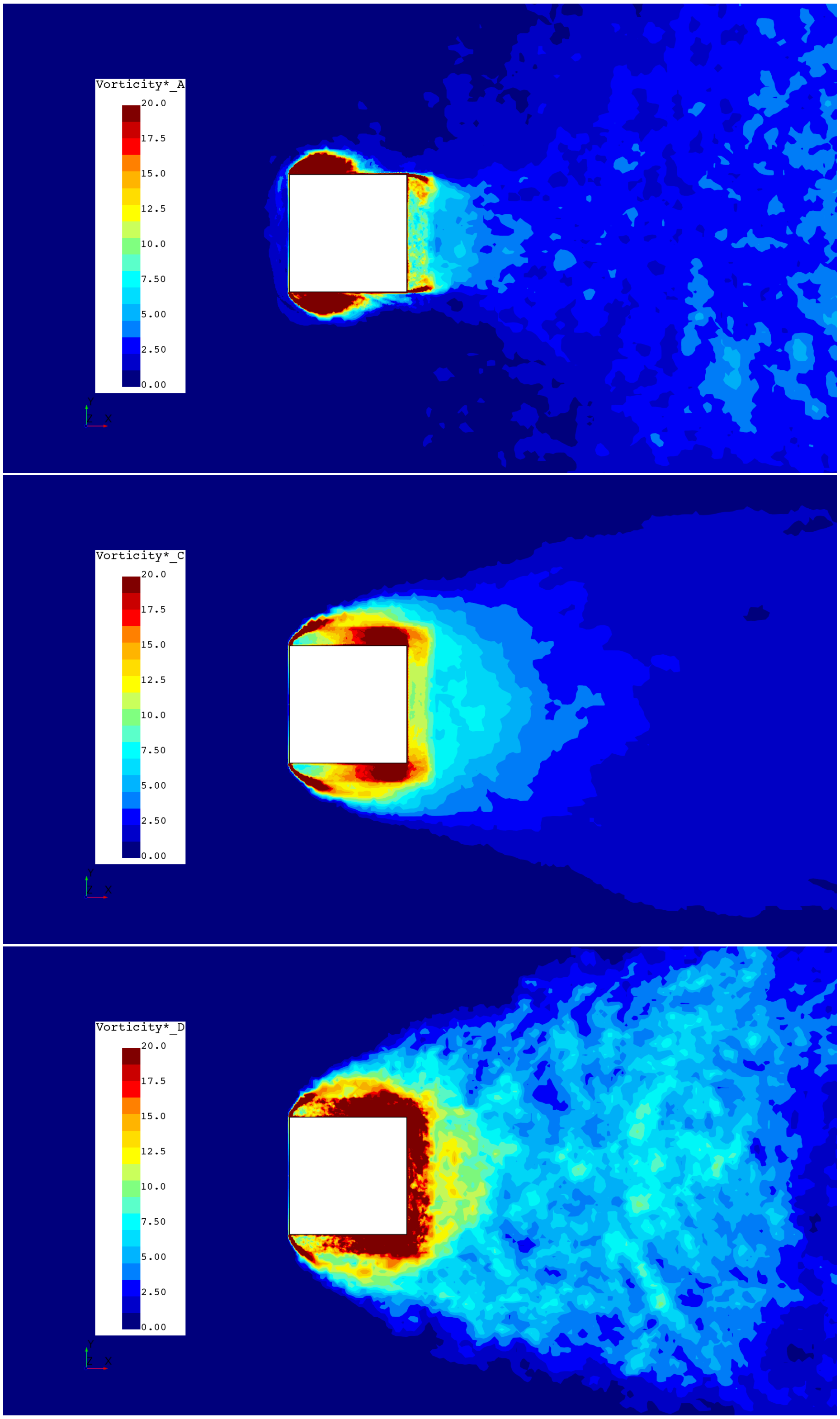

Figure 27: $|\omega^*|$ scalars at cylinder centerline of $a_x > 0$ (top), $a_x = 0$ (middle) and $a_x < 0$ (bottom)

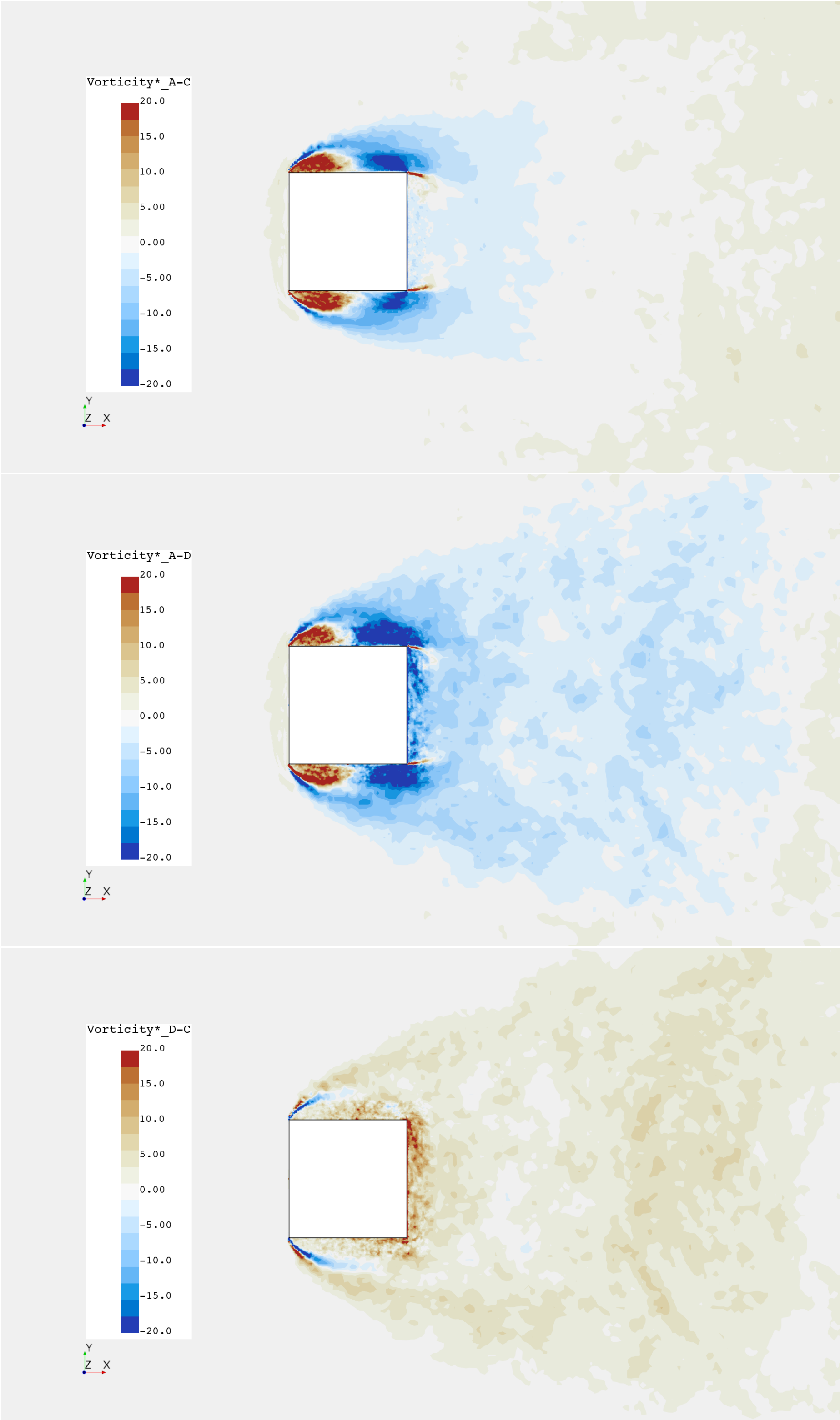

Figure 28: $|\omega^*|$ deltas at cylinder centerline of $(a_x > 0) - (a_x = 0)$ (top), $(a_x > 0) - (a_x < 0)$ (middle) and $(a_x < 0) - (a_x = 0)$ (bottom)

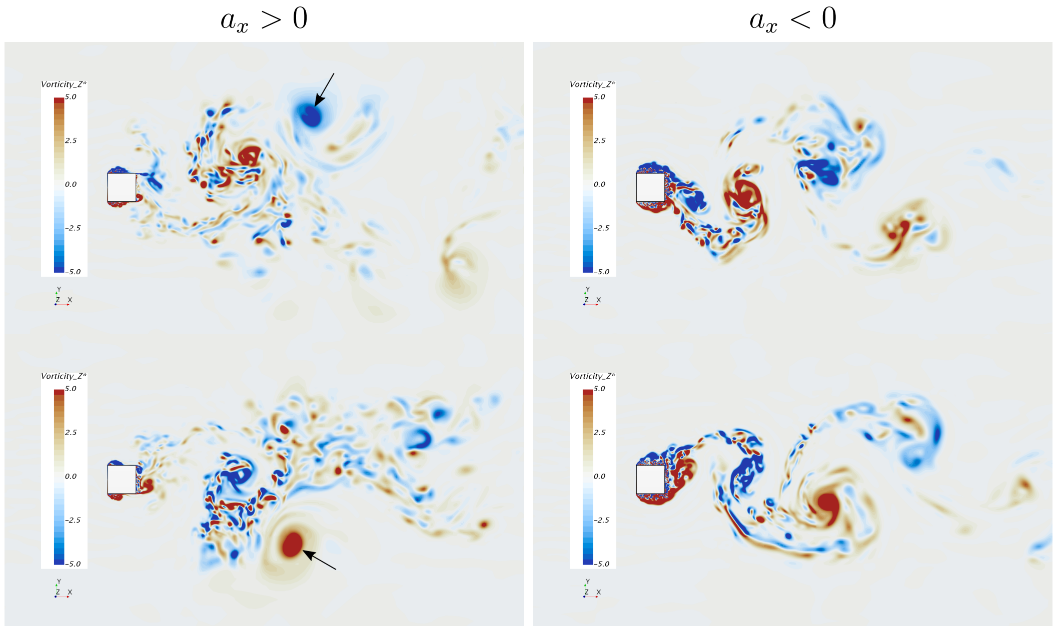

Figure 29: Instantaneous non-dimensional vorticity Z component ω_Z^* at cylinder center plane ($H_z^* = 0$) for $a_x > 0$ and $a_x < 0$ recorded at $V_{ref} = 6\ \mathrm{m\,s^{-1}}$. The top and bottom rows represent flow approximately 180° out of phase.

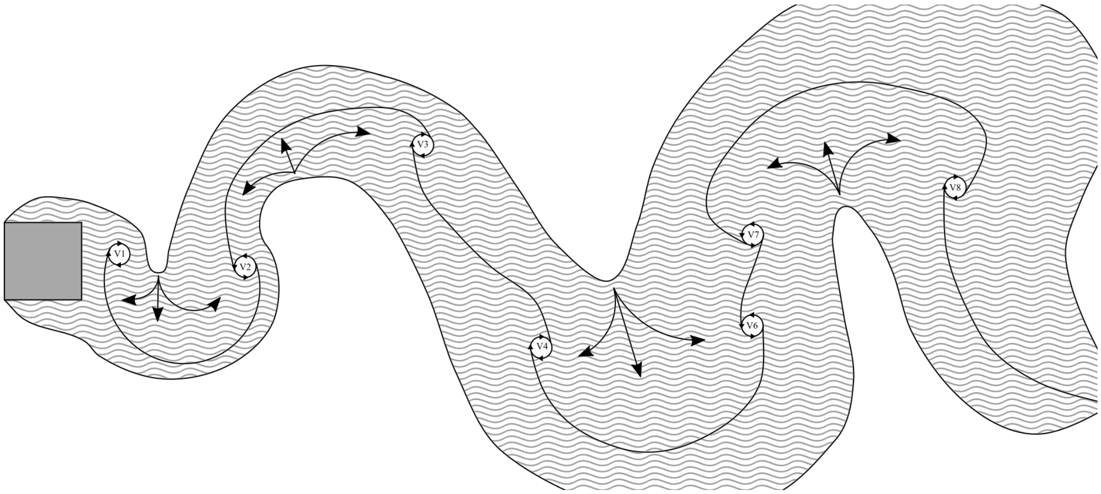

Figure 30: A simple cartoon demonstrating a single phase of vortex shedding and the region of vorticity (depicted as grey waves) surrounding the cylinder and wake.

Fourth, further investigation revealed an imbalance of vorticity, driven by tangential pressure gradients and longitudinal free-stream acceleration conditions causing a reduction in near wall vorticity for the accelerating case and an increase for the decelerating case. These changes in the leading edge separation and vorticity along with variations in free stream velocity during vortex core formation behind the cylinder caused an imbalance in the accelerating wake, displacing every other vortex core away from the x-axis. Conversely, the surplus of vorticity during deceleration and free-stream velocity variation caused vortex cores to align with the x-axis. And finally, the inertial coefficient was calculated to be used with Equation 2 for prediction of the square cylinder undergoing acceleration and deceleration.

CHAPTER 6: DRIVAER MODEL ACCELERATION

In this study, we focus on the aerodynamic effects of longitudinal acceleration and deceleration of a modern road vehicle model, the DrivAer fastback variant developed by Heft et al. [25] with lessons learned from Chapter 5. Road vehicles undergoing unsteady mean free stream conditions have been investigated previously, yet none have focused on the basics of pure longitudinal acceleration. Further yet, to the best of the authors knowledge none have implemented an ensemble averaging technique in an attempt to obtain averaged flow field conditions for a single velocity undergoing longitudinal acceleration. The DrivAer model was created by Heft et al. [25] and presented in 2012 to provide a realistic car model to close the gap between the highly researched Ahmed body, presented by Ahmed et al. in 1984 [1], SAE body presented by Cogotti in 1999 [13] and realistic car geometries on the road today. While the Ahmed and SAE bodies were state of the art for their time, the DrivAer model is the current model of choice for current researchers and is apparent at the latest conferences of FKFS-2017 (Forschungsinstitut für Kraftfahrwesen und Fahrzeugmotoren Stuttgart) where two presentations included upgrades for the DrivAer model and SAE world congress 2018 (Society of Automotive Engineers), where "DrivAer" is the focus of development in several papers in comparison to the older Ahmed and SAE bodies. While the DrivAer model originally consisted of three greenhouse variants; notchback, estateback, and fastback, the fastback variant was selected for this study due to the smooth roof/rear glass shape representing a high performance vehicle. In addition, the flat floor was implemented to reduce computational complexity with side mirrors and simplified wheels, additional details on the geometry are available in a later section. Overall dimensions and configuration as presented by Heft[25] can be observed in Figure 31, noting that a 40% scale model was used. Scale models are often used in aerodynamic development for road vehicles to reduce overall costs of both prototyping models and in wind tunnel operational costs from reduced power consumption. This is generally sufficient for most aerodynamic investigations when Reynolds numbers are within the same order of magnitude and there is not a strong dependence on the drag coefficient (C_D) over tested velocity ranges. Heft et al. [25] performed Reynolds independency tests, reporting that the drag coefficient converges at $Re = 4.96 \times 10^6$ and varies by only 2.5% from $Re = 2.5 \times 10^6$ to $Re = 4.96 \times 10^6$. For transient scale resolving CFD simulation, scale models also help to save in mesh efficiency due to reduced volume for discretization while the scales of turbulence, the Taylor microscale in this case using Equation 27, reduces by 63.25% for a Reynolds number reduction of 40%. Scale models also use restraints during tunnel testing as shown in Figure 32, are a potential source for error, which will be demonstrated in this study. In this chapter, the DrivAer CFD model will first be validated against experimental results and then a periodic 1G acceleration deceleration inlet condition will be applied for 6 periods, allowing for the calculation of inertial coefficients and flow field investigation.

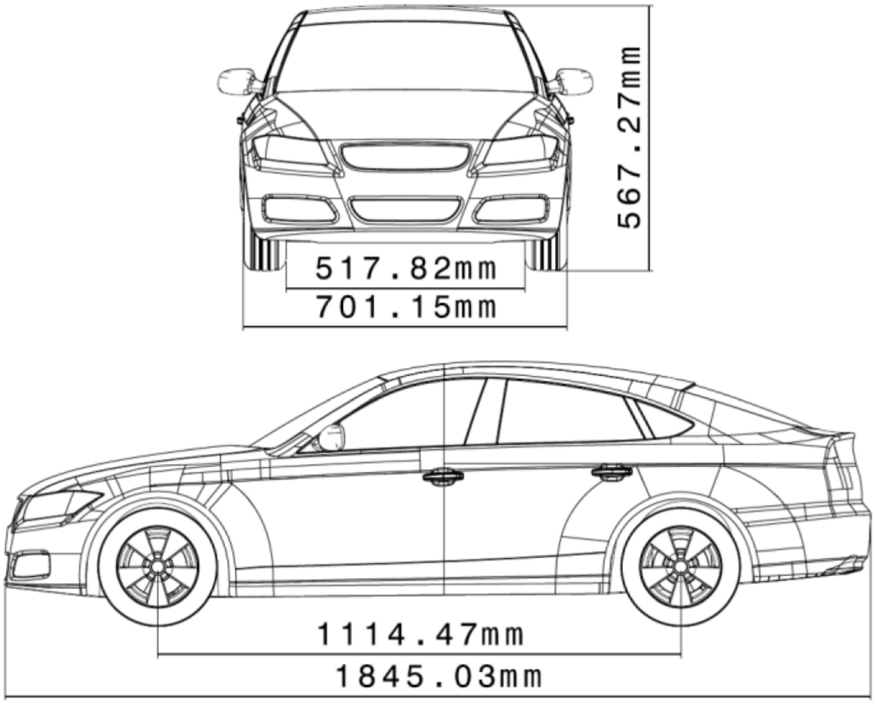

Figure 31: The original overall dimensions of the 40% DrivAer model with fastback presented by Heft[25].

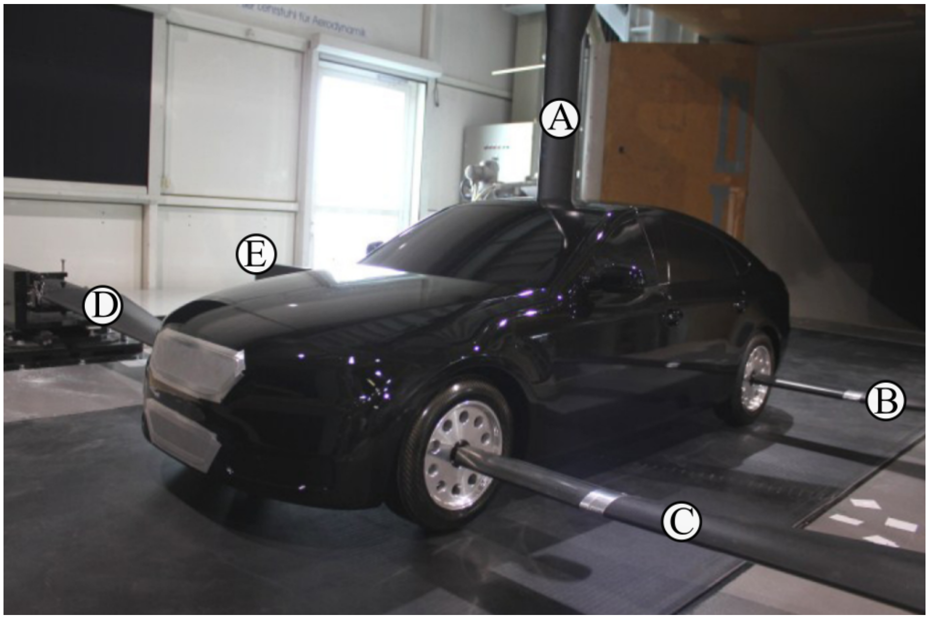

Figure 32: The tunnel configuration used by Heft[25]. Note the five restraints holding the body and the wheels.

6.1 DrivAer CFD Model Validation

Before the acceleration simulation was performed, the CFD model was validated against experimental results. This was done primarily to ensure that the model performed with good agreement to experiments and not an in-depth study of how well CFD can replicate experimental results. The validation was performed with the same underlying setup as the accelerating simulation with a constant time step of 0.0001 s, a constant inlet velocity of $40\,\mathrm{m\,s^{-1}}$ and forces were averaged from 1 to 4 s of simulated time. Overall body force coefficients can be viewed in Table 6 compared to the compiled experimental results presented by Collin et al. [14]. When comparing CFD results to wind tunnel experiments of road vehicles, several additional items must be addressed. First, the force measurement techniques and how the vehicle is constrained in the tunnel. As shown in Figure 7 there are five mounts restraining the vehicle, where A is the single restraint for the vehicle body, measuring C_D,C_L,C_{LF} of only the body. The remaining constraints hold the wheels and measure their C_D only. Note that the restraints are an obstruction to the flow field, and while they are streamlined the do still influence the flow field, the effects of which cannot be removed from measurement data. In comparison, CFD can be performed with or without restraints since they are not required to measure force or hold the car in place. For simulations in the dissertation, forces are reported through the integration of surface pressure and skin friction. Second, wind tunnels are complex experimental tools, they attempt to simulate road conditions, which according to Collin et al. [14] the two wind tunnels investigated do this quite well however the absolute value of C_D was found to vary by more than 0.010 depending on the position of the test body to the wind tunnel nozzle. Additionally, C_L values were found to vary between tunnel and road conditions by 0.024. These discrepancies are attributed to open jet wind tunnels and their ability to maintain uniform flow conditions surrounding the vehicle, as well as the ability to simulate moving road conditions. This information is important to consider for any CFD model validation, that unless the CFD model is simulating the tunnel experiment, exact results should not be expected. To draw closer comparison, the current CFD coefficients were corrected for the absence of restraints with data from Collin et al. [14] who used CFD to simulate tunnel conditions with and without restraints present. Overall, force coefficients are with good agreement of the experimental tunnel results from TUM and Audi. Total C_D is under predicted within 4%, where the source of the underprediction could be attributed to the wheels. This could be due to the contact patch geometry simplification, a lack of a moving reference frame, the simplified wheel spokes, or a discrepancy in the flow field around the fascia causing a lack of stagnation on the forward face of the wheel contact patch. The body front lift coefficient, C_{LF} was considerably over predicted, yet we must consider that two different wind tunnels in Table 6 reported drastically different C_{LF} values, indicating that the predicted CFD results herein should be accepted within delta to experimental error resulting from tunnel techniques. The body rear lift coefficient, C_{LR} was with good agreement to experiments. In addition to body forces, body center line pressure coefficient is plotted for the top and bottom portions of the vehicle in comparison to initial experimental measurements of Heft et al. [25]. Figure 33 contains C_P data for the upper portion of the vehicle over the body where current IDDES results agree well with experiment, however there are two key areas of issue which require explanation. First, at $X = 0.5\,\mathrm{m}$ at the leading edge of the roof to $X = 1.2\,\mathrm{m}$ at the rear of the roof, there is a considerable under prediction of C_P, most likely due to the lack of the tunnel sting from the experiment, marked at A in Figure 32. Second, there is a lack of positive pressure on the trunk between $X = 1.2\,\mathrm{m}$ and $X = 1.5\,\mathrm{m}$ which could also be related to the lack of the sting in the CFD model and was pointed out by [14] that the sting increased C_{LR} compared to no sting. Nonetheless, investigating this discrepancy further was not the focus of the validation, yet cannot be denied as a potential source of error for future studies. C_P on the underside of the vehicle is plotted in Figure 34 where one area of discrepancy is apparent at the front of the vehicle near $X = -0.25\,\mathrm{m}$ indicating a potential variation in the leading edge flow structure. Although there are some discrepancies between CFD and experimental data, these results were deemed sufficient for carrying out the acceleration study.

6.2 Data Processing

When this DrivAer acceleration case was originally created, the acceleration rate was reduced to 1G to better represent performance capabilities of commercial road vehicles. In addition, the time span for desired acceleration-deceleration pulls was increased due to questions arising from the previous cylinder simulation if the change of sign in acceleration rate being too close to the desired velocity reference would effect the solution. While this may be true, the impact is small, and is addressed in Chapter 7, where the resulting inertial coefficient and Morison equation predict acceleration

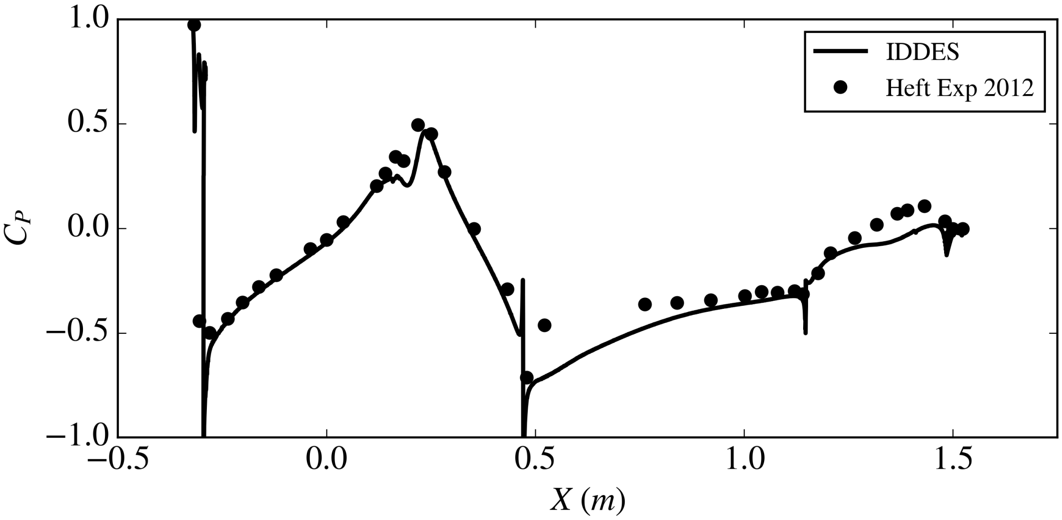

Figure 33: Pressure Coefficient over the top of the vehicle at centerline $Y = 0$ of current IDDES simulation versus experiments of Heft et al.[25]

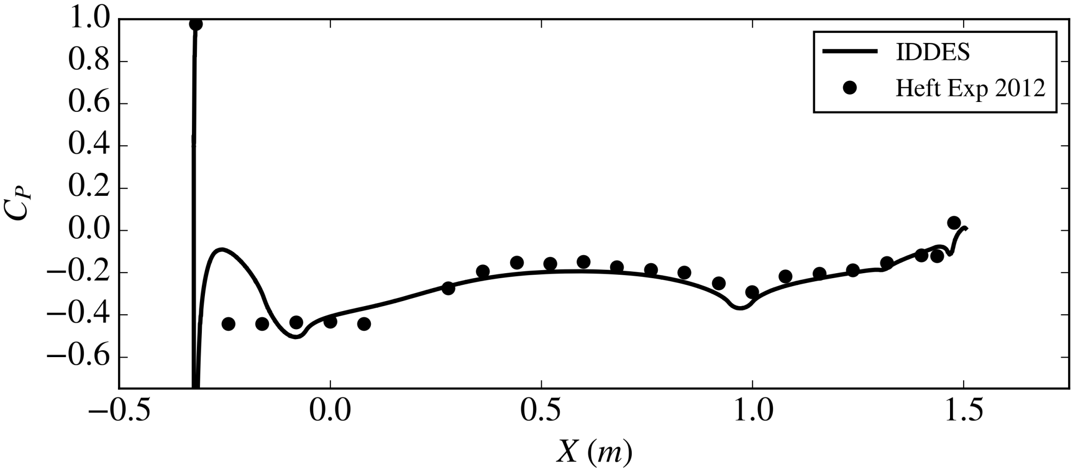

Figure 34: Pressure Coefficient over the bottom of the vehicle at centerline $Y = 0$ of current IDDES simulation versus experiments of Heft et al.[25]

	Current CFD	Restraint Correction	TUM	Audi
C_D	0.237	0.244	0.252	0.251
$C_D Body$	0.186	0.195	0.189	0.196
$C_D Wheels$	0.051	0.049	0.063	0.055
C_L	-0.078	-0.066	-	-
C_{LF}	-0.121	-0.115	-	-
C_{LR}	0.043	0.049	-	-
$C_L Body$	-0.047	-0.035	-0.008	0.024
$C_{LF} Body$	-0.107	-0.101	-0.063	0.039
$C_{LR} Body$	0.060	0.066	0.055	0.063
$C_L Wheels$	-0.031	-0.031	-	-

Table 6: Force coefficient results from validating the DrivAer fastback model to experiments compiled by Collin et al. [14].

behavior with good agreement even with a small constant acceleration span. Unfortunately, for this study of the DrivAer model, the simulated time period for acceleration-deceleration pulls became 6 s, three times longer that the cylinder simulation of 2 s, resulting in significantly less data points with given computational resources. Due to this, the DrivAer model acceleration only contains six total acceleration-deceleration periods in comparison to the thirty plus periods recorded for the cylinder simulation, requiring additional data processing for a clear representation of trends. To process the cylinder simulation data, forces during each period were ensemble averaged to determine acceleration and deceleration forces. For the DrivAer model the use of least square fitting second order polynomials to acceleration and deceleration forces will be explored as a method for obtaining inertial coefficients with less overall input periods. Figure 35 displays the instantaneous drag force for the DrivAer model while undergoing acceleration(red) and deceleration (blue) versus time. Overall, there is

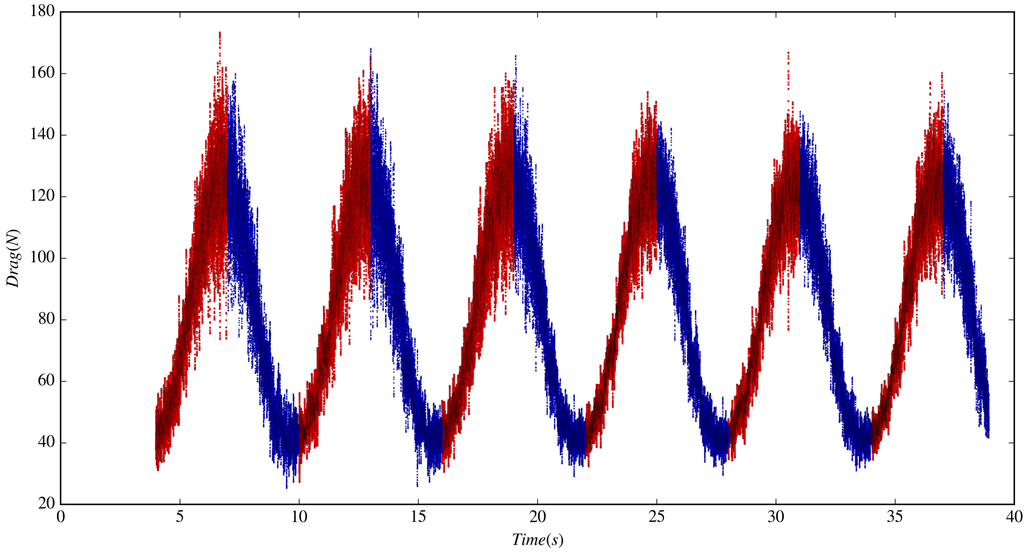

Figure 35: Total DrivAer drag force versus time.

significant noise present and to observe any trends in the forces between acceleration and deceleration, a plot versus $V_{ref}(t)$ in Figure 36 is more useful.

Note that in Figure 36 all six periods are present and the clear trend begins to be apparent that during acceleration (red) the drag force is greater than during deceleration (blue). In addition, the non-accelerating force is plotted at V_{ref}=40 m s^{-1} as the black dot and is extrapolated over the measured velocity range via the drag force coefficient, represented as the dashed black line. The three cases; accelerating, non-accelerating and decelerating are only equivalent due to noise in the drag force and when the acceleration rates are significantly lower outside of $V_{ref} = 40{\pm}7\,\mathrm{m\,s^{-1}}$. Further processing is required to determine a quantifiable trend.

Before least squares fitting a second order polynomial to drag force, data was first removed outside of $V_{ref} = 40{\pm}7\,\mathrm{m\,s^{-1}}$ as to not skew the fit as a result of changing acceleration rates outside of that zone. Second order polynomials were then fit to the accelerating and decelerating drag data respectively and can be seen in Figure 37 as

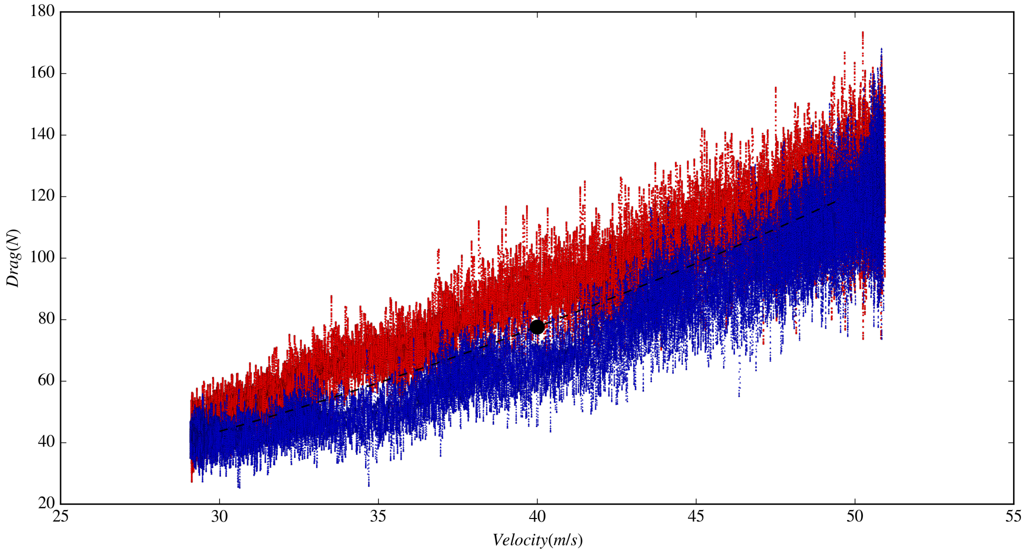

Figure 36: Total DrivAer drag force versus velocity.

the solid red (accelerating) and blue (decelerating) solid lines where the clear trend is now present between the three cases.

For analyzing lift force the same process was applied to the time varying lift force seen in Figure 38 where the lift force is noisier in comparison to the drag force. Even when the lift is plotted versus velocity in Figure 39 a discernible trend is not visible.

The trend in lift force is not present until a least-squares second order polynomial is fit in Figure 40 and in comparison to the noise of the lift signal is small, but still measurable.

To obtain the front lift percentage, the same data analysis method was applied to obtain the variation in front lift between the accelerating and decelerating cases, the result of which is presented in Figure 41.

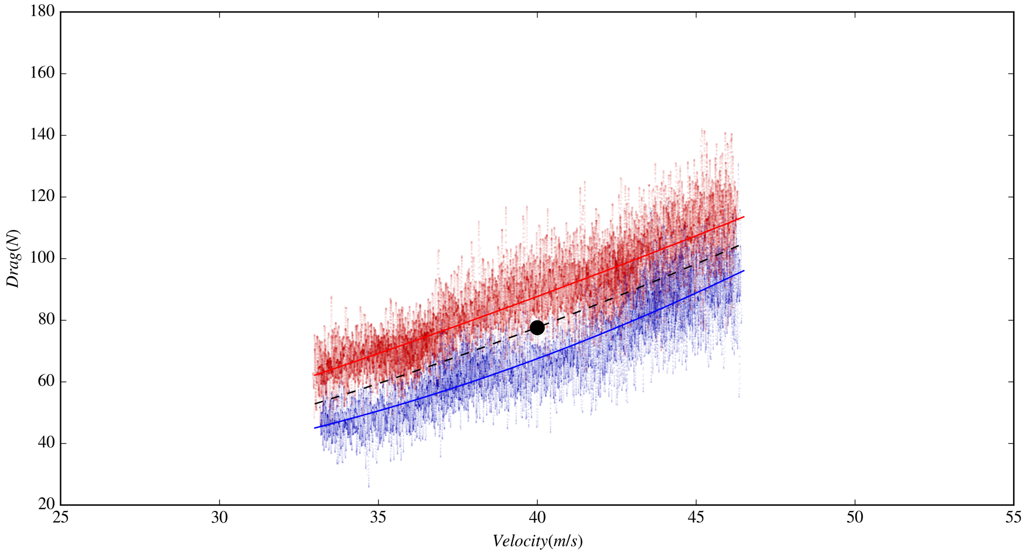

Figure 37: Total DrivAer drag force versus velocity with second-order least-squares polynomial fit.

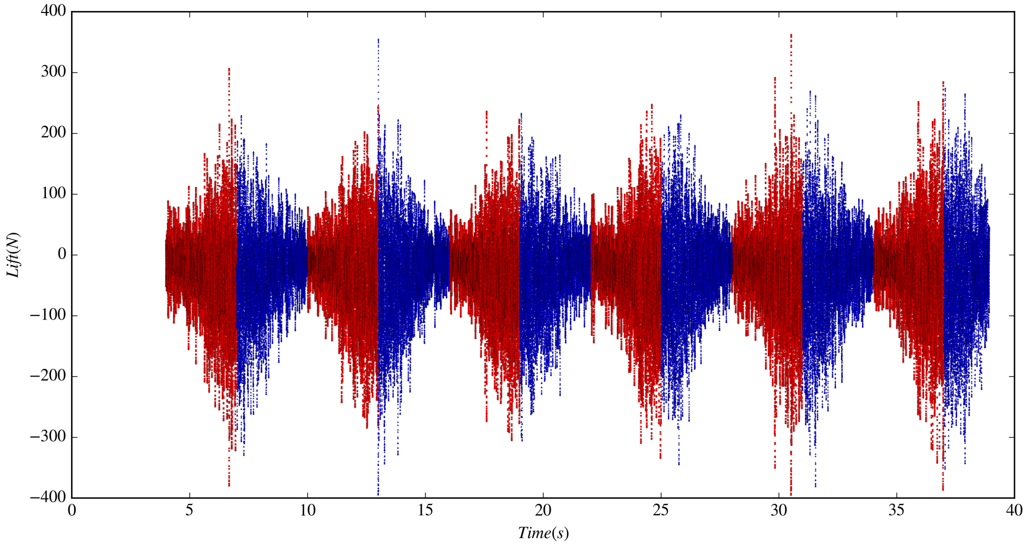

Figure 38: Total DrivAer lift force versus time.

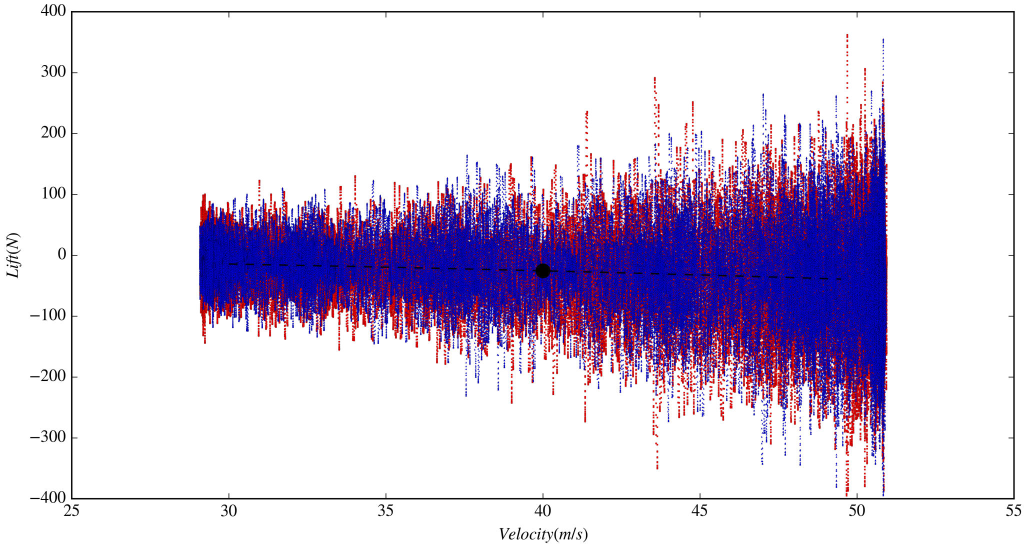

Figure 39: Total DrivAer lift force versus velocity.

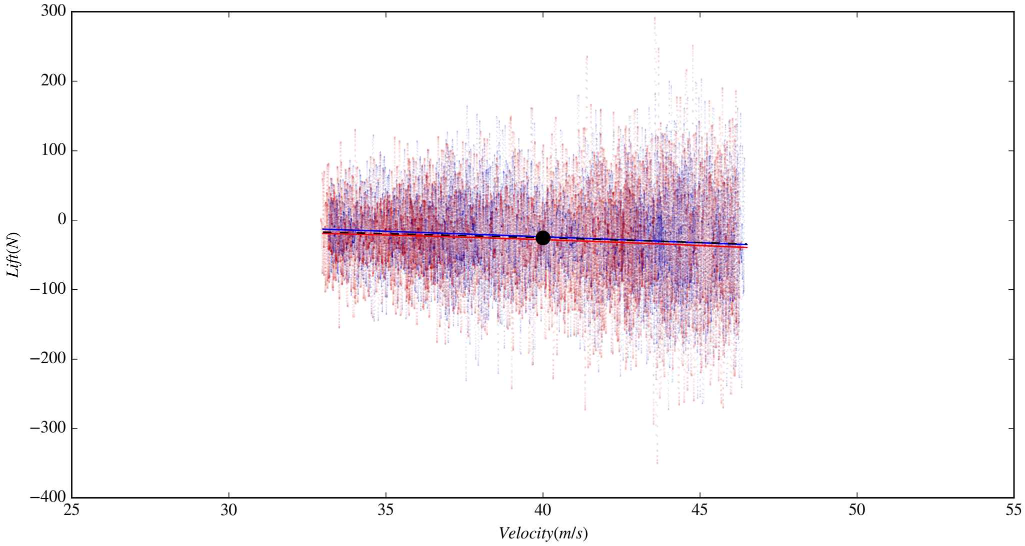

Figure 40: Total DrivAer lift force versus velocity.

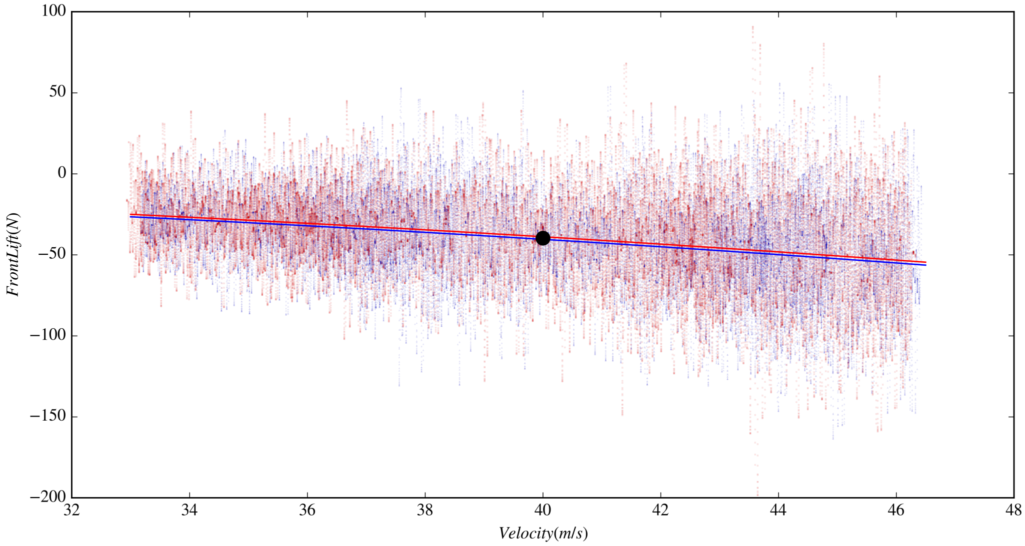

Figure 41: Total DrivAer front lift force versus velocity with second-order least-squares polynomial fit.

6.3 Results

Overall body forces and inertial coefficients (C_M) are compiled in Table 7, where non-accelerating results ($a_x = 0$) were obtained by averaging a constant V_{inlet} simulation over 2 s run time and all reported accelerating forces were obtained from least-squares polynomial fit data. The drag force for both accelerating and decelerating conditions was found to vary ±13% in comparison to the non accelerating force at $V_{ref}(t) = 40\,\mathrm{m\,s^{-1}}$, this symmetric delta yielded an inertial drag force coefficient of 2, unlike the cylinder study which had a significant asymmetry between the acceleration and deceleration cases. The cylinder had no variation in the ensemble averaged lift force due the body being suspended in a channel flow, far away from any other boundaries. The DrivAer model is in close proximity to the road and does not have a neutral lift force at normal operating conditions. Due to this and possibly due to the shape of the vehicle promoting boundary layer separation on the rear glass, during

Table 7: Ensemble averaged body forces based on second-order least-squares polynomial fitting of data,taken at V_{ref} =40 m s^{-1} for the DrivAer at $a_x = -1.5G$, $a_x = 0$ and $a_x = 1.5G$. Note that lift values were taken from the filtered results, not the poly lines.

a_x	$Drag(N)$	$Lift(N)$	$\%Front$	C_{MD}	C_{ML}
$-1G$	67.49	-24.03	168	2.02	-0.3
0	77.63	-25.55	155	-	-
$1G$	87.68	-28.03	137	2.00	-0.54

longitudinal acceleration there is an observed variation in overall lift force, indicating the need for a set of inertial lift coefficients for longitudinal acceleration. Due to the small amount of lift present for the non-accelerating baseline, a small variation in lift force will result in a considerable percentage change, -5.9% during deceleration and 9.7% during acceleration, yielding inertial lift coefficients of -0.3 and -0.54 for deceleration and acceleration. The overall lift front percentage for the non-accelerating case was found to be 155% during the validation study due to the vehicle making front downforce and rear lift. During acceleration, the vehicle's front downforce level was reduced, yet the overall downforce increased indicating a rearward balance shift which is demonstrated in the shift of front percentage of lift. Interestingly, the front percentage of lift decreased by 18% for acceleration in comparison to non-acceleration and increased 13% during deceleration.

Unfortunately due to a lack of recorded acceleration deceleration periods, the obtained ensemble averaged fields from this particular study are spatially noisy. This is due to the turbulent fluctuations of shear layers, boundary layer growths and wake oscillations not being averaged out by the insufficient ensemble averaging in this study. While this is true, some conclusions can still be drawn from available data, noting that

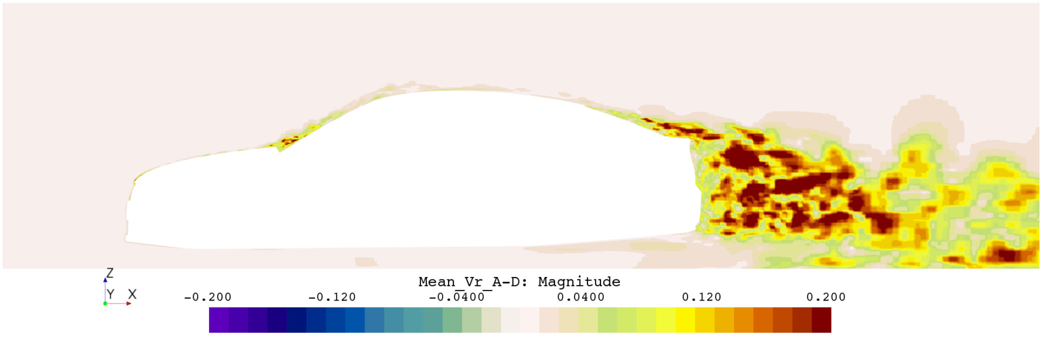

Figure 42: Delta of Vr A-D.

future investigations should aim to obtain considerably more periods for ensemble averaging. Velocity magnitude was non-dimensionalized by V_{ref} in this study as Vr, of which the Vr delta Acceleration-Deceleration at vehicle centerline $Y = 0$ is presented in Figure 42. There are several variations visible in Vr between the accelerating and decelerating cases:

- At the base of the windshield the is a surplus of Vr, indicating that the accelerating case sees higher velocity here to the magnitude of 0.2 Vr. This same observation was also true for the previous cylinder study, although the cylinder saw higher values of delta Vr in the wake.

- Higher velocity is present at the top of the rear decklid during acceleration in comparison to deceleration, indicating that the separation on the rear glass is reduced for the accelerating case and increased during deceleration.

- Higher velocity is present in the wake behind the vehicle during acceleration and lower velocity is present during deceleration

Vorticity magnitude was non-dimensionalized in this study by the ratio of $\frac{V_{ref}(t)}{L}$ as

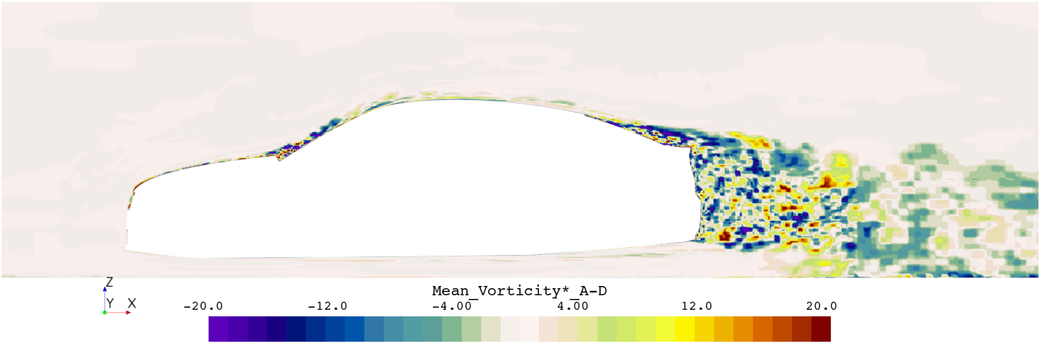

Figure 43: Delta of ω^* A-D.

ω^*. The delta of ω^* (Acceleration-Deceleration) at vehicle centerline Y=0 is presented in Figure 43 where again several variations are visible among noise:

- There is an increase in vorticity at the leading edge of the hood indicating more vorticity in this area during acceleration
- Overall, there is less vorticity near the wall on the top side of the vehicle, indicating more vorticity at the wall during deceleration. This was also observed in the cylinder study.
- Less vorticity is present over the rear glass and trunk, this is likely due to a change in separation of the rear glass changing the location of the shear layer. This was also observed in the cylinder study due to a change in the location of leading edge separation shear layers.
- Less vorticity is present in the wake of the vehicle, indicating that there is more vorticity in the wake during deceleration, which was also observed in the cylinder study.

6.4 DrivAer: Concluding Remarks

Simulating longitudinal acceleration of the 40% scale DrivAer model with only six acceleration-deceleration periods still yielded enough information to determine inertial coefficients and macro changes to velocity and vorticity flow fields. Results showed that significant drag and lift force variations do occur for the DrivAer model with drag vartions of $\pm 13\%$ while lift varied -5.9% during deceleration and 9.7% during acceleration in comparison to non-acceleration. Lift balance also varied significantly by -18% for acceleration and 13% during deceleration indicating that the vehicles design may cause shifts in aerodynamic balance from changes in acceleration, supported by flow field variations in the rear glass and trunk areas. Inertial coefficients were also obtained from simulation data and could be used in future studies to validate results against other acceleration rates and velocity speeds.

CHAPTER 7: DRIVAER-GTR ACCELERATION

Previous works in this dissertation have demonstrated the magnitude for considering acceleration aerodynamics for a bluff body with the same length scale as a road vehicle and a 40% generic road vehicle scale model, the DrivAer model. Both results showed atleast a ±10% change in drag forces for the wind speed and acceleration rates tested. The final portion of this dissertation is to investigate acceleration aerodynamics of a high performance road vehicle, a test article that generates a considerable amount of down force with small ground proximity. Unfortunately, to the knowledge of the author, such a geometry does not exist as an open source model for the scientific community, and had to be created for this dissertation. The DrivAer fastback variant with flat floor, mirrors and solid wheels (used earlier in this dissertation) was selected as a base model to build on. This included simplifying features such as removing door handles, lowering the ride height, widening the wheels, flaring out wheel openings, installing a splitter on the front fascia, a diffuser under the rear fascia, two diffusers in the front floor behind the splitter, a decklid rearward extension with "boat-tailed" quarter panels and a rear wing with goose neck mounts. Interestingly, unbeknownst to the author, another group had been developing a performance variant of the DrivAer model, with a focus towards bolt on pieces at The University of Cranfield. This paper by Soares et al. [57] and is set for publication on April 3rd 2018, which is past the date of which this dissertation has been created. This demonstrates the global desire for a high performance variant of the DrivAer model.

The goal of this exercise is to investigate the impact of acceleration on high down force generating road vehicles with a focus on lift forces.

7.1 DrivAer-GrandTouringRacing Model

The model was created with several goals in mind. First, was to create efficient down force with a C_L near -1 (recall that the fastback DrivAer model generated a C_L near 0) and a lift to drag ratio greater than 2.2. Second was to hold a considerable front balance between 40% and 50% due to the assumption of a rear wheel drive vehicle for motor sport and to not be so low as to promote vehicle blow over or take off during extreme hill cresting conditions. And third was to keep the design simple and stick to basic aerodynamic concepts.

With the intent to install a rear wing that could be easily modeled and replicated, the Joukowsky transform [28] was implemented to create an asymmetric rear wing profile with Equation 29 and Equation 30.

$$X_i = \xi_i + \varepsilon + \frac{a^2}{(\xi_i - \varepsilon)^2 + \eta_i^2}(\xi_i - \varepsilon) \tag{29}$$

$$Y_i = \eta_i \left[1 - \frac{a^2}{(\xi_i - \varepsilon)^2 + (\eta_i - \psi)^2}\right] \tag{30}$$

Where,

The rear wing was then imported into ANSA Beta and the rear trailing edge of the wing trimmed back by 11 points and a wicker installed orthogonal to the top surface of the wing. The final chord length of the wing (for the full scale DrivAer-GTR

Table 8: Joukowsky transformation coefficients to generate the DrivAer-GTR rear wing profile

i	R	ε	a	θ_i	ξ_i	η_i	χ
$0, 5..360$	2	0.12	$R - \varepsilon$	$\frac{i\pi}{180}$	$Rcos(\theta_i)$	$Rsin(\theta_i)$	0.2

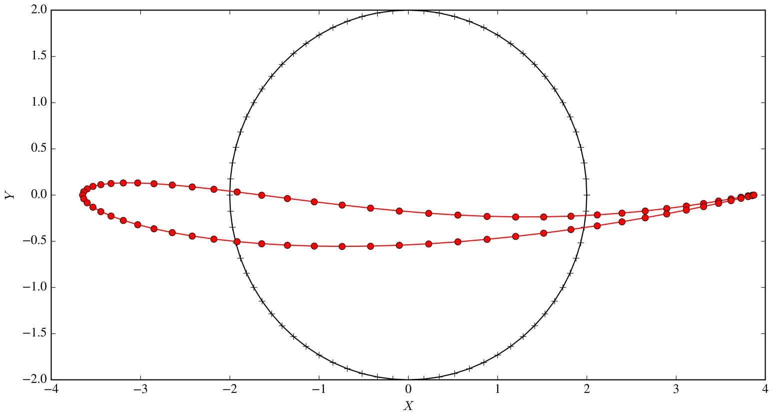

Figure 44: The calculated Joukowsky aerofoil for the DrivAer-GTR with inputs from Table 8.

model) was 300 mm, wicker height of 11.28 mm and span of 1.6 m. The wing was installed at an angle of attack (AOT) equal to 7 deg (measured with respect to the X-axis from the top of the wicker to the highest point of the wing leading edge) and set to an overall height where the wicker is equal to the highest roof point. Wing end plates were also created with overall dimensions of 312 mm × 160 mm × 6 mm and wing mounts were created to extend behind the wing in an attempt to not perturb the pressure field near the airfoil.

The vehicle was lowered 107 mm such that the lowest portion of the full scale flat floor for the original DrivAer infront of the front axle was 50 mm and all four wheels were increased in overall width by 50 mm away from vehicle centerline for a total wheel width of 250 mm and then moved inboard 5 mm. Front wheel flares were

Figure 45: The final DrivAer-GTR Joukowsky wing profile with wicker.

then added to encapsulate the wider front wheels and the fascia was simplified and extended downward in Z to intersect with the lowest floor point at the front axle. A 10 mm thick splitter was then extended forward 100 mm ±770 mm of the center line and blended back towards the wheel openings for a smooth transition. Front diffusers were also placed in front of the tires.

The original DrivAer model does not boast high down force, and the large greenhouse removes positive pressure from the top of the trunk area, thus the trunk was extended rearward 200 mm and up 45 mm to promote positive pressure.

7.2 DrivAer-GTR Baseline

Before running a transient IDDES simulation on the DrivAer-GTR, a steady RANS Menter $k-\omega$ SST simulation was performed to predict the overall aerodynamic performance. Results at that point indicated that the orginial performance goals were not met, note at this time the rear wing chord length was 250 mm, thus the rear wing chord was increased to the final 300 mm. A transient IDDES simulation was then run (with $V_{inlet}(t)$ constant) as the baseline solution. Values for the baseline solution are reported in Table 9 where, as expected, the wing drives much of the vehicle's performance with an L/D of 18.10.

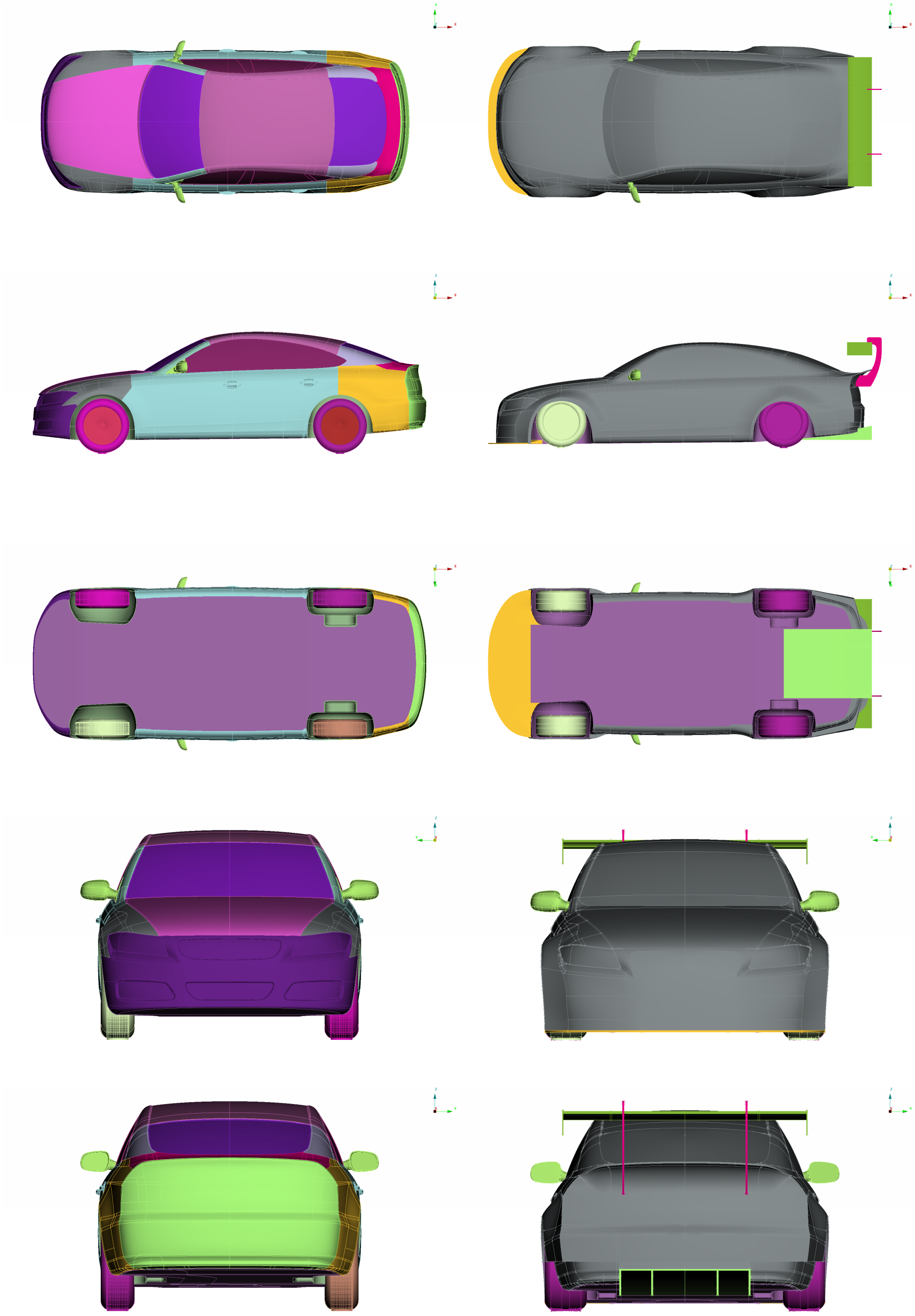

Figure 46: Comparison to the original Drivaer Fastback (left) and Drivaer-GTR (Right).

Table 9: Drivaer-GTR baseline force coefficient results.

C_D	C_L	$\%Front$	$\left\|\frac{L}{D}\right\|$	C_DWing	C_LWing	$\left\|Wing_{\frac{L}{D}}\right\|$
0.378	-0.919	42.70	2.43	0.015	-0.276	18.10

Time averaged C_p scalar views of the baseline DrivAer-GTR are presented in Figure 47 which demonstrates where aerodynamic devices are improving the vehicles overall performance. From the top iso-metric view (top) and top view (middle), the front splitter helps to project positive stagnation pressure in the Z-axis while the trunk spoiler and rear wing both increase down force at the rear of the vehicle. From the bottom iso-metric view (bottom) the splitter also creates suction due to the proximity to the road and the rear diffuser helps to lower overall under body pressure at the rear axle.

Slices of time averaged non-dimensional velocity magnitude (V_r) at the vehicle centerline in Figure 48 also demonstrate the benefits of the added aerodynamic devices. The wing is effected by the downward flow angle of the greenhouse, somewhat increasing the overall angle of attack which is visible at the rear of the vehicle. This is also demonstrated in the slices of C_P in Figure 49 where the stagnation at the leading edge of the wing is seemingly on the top surface, not the nose of the airfoil. The rear spoiler is likely not drastically effective at improving overall down force because of the flow separation on the rear glass (note that the original DriVaer greenhouse was maintained), however the device does aid in giving the exit flow an upward component. The rear diffuser also noticibly increases V_r magnitude at the rear axle and feeds a vertical component of the underbody flow up and into the wake. The front splitter, which detailed flow is visible in the bottom image of Figure 49 generates a considerable amount of down force, demonstrated by the C_P variation in the Z-axis greater than 2 at the leading edge.

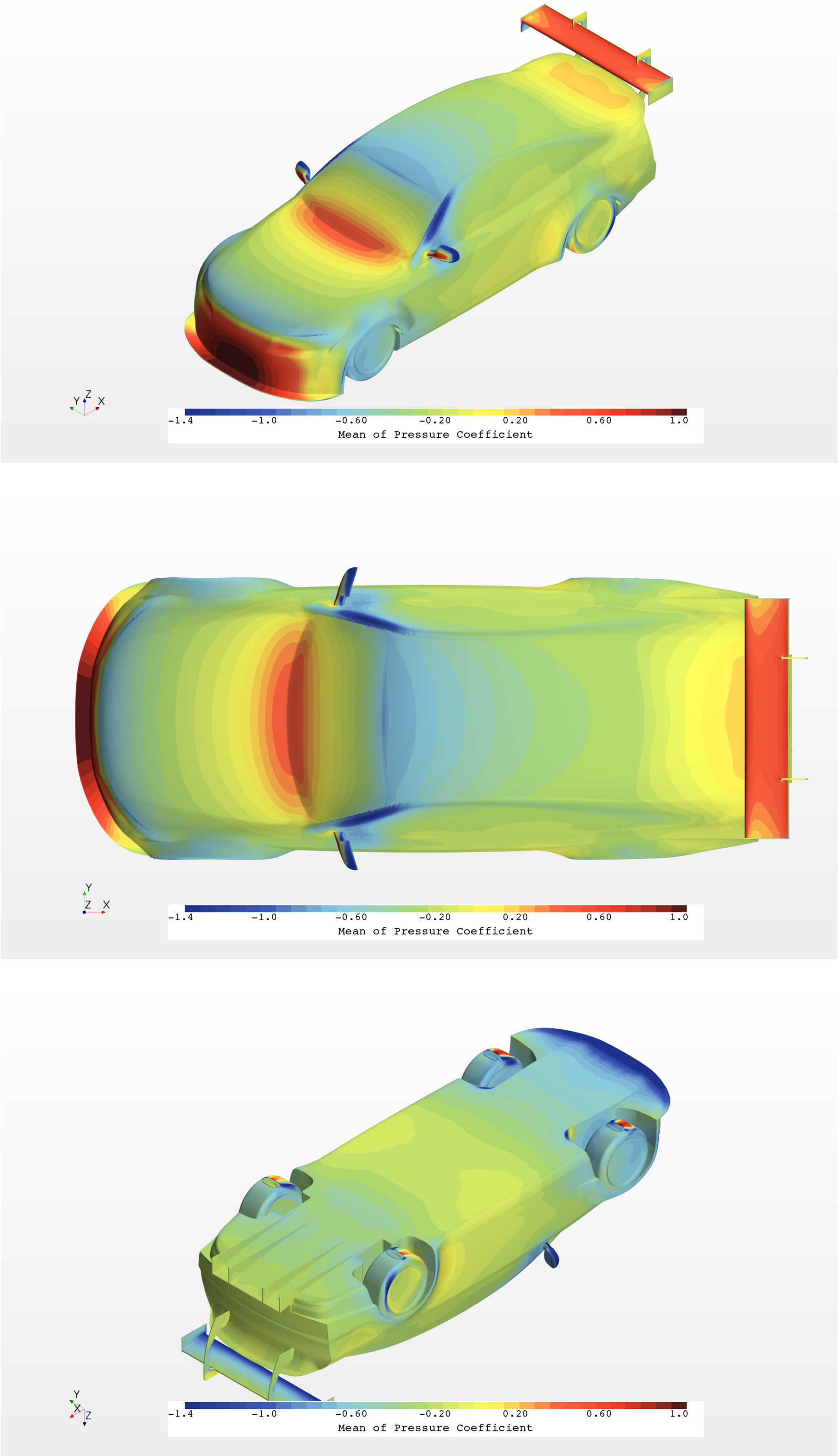

Figure 47: Isometric view of the DrivAer-GTR Baseline.

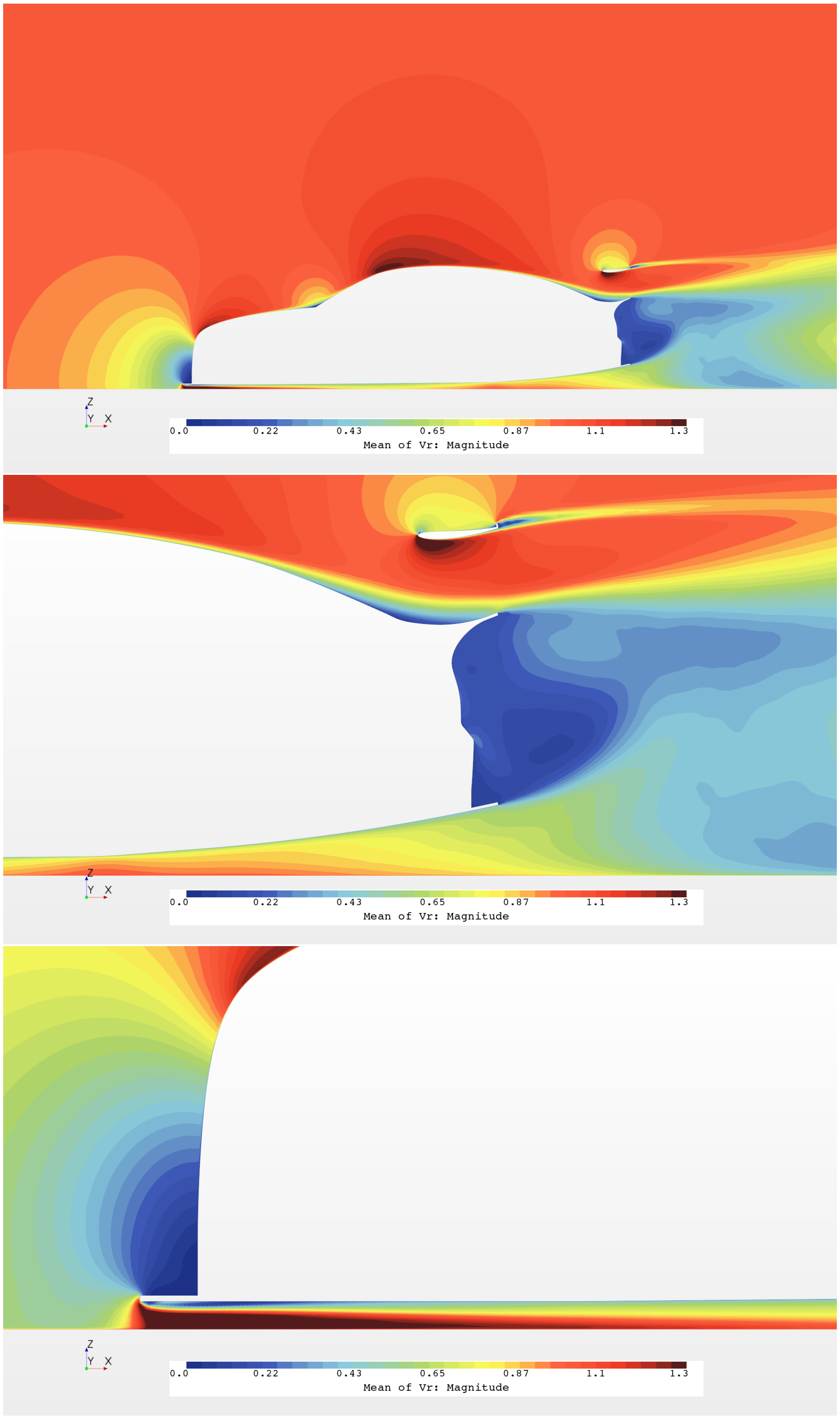

Figure 48: Y=0” V_r slice of the DrivAer-GTR Baseline.

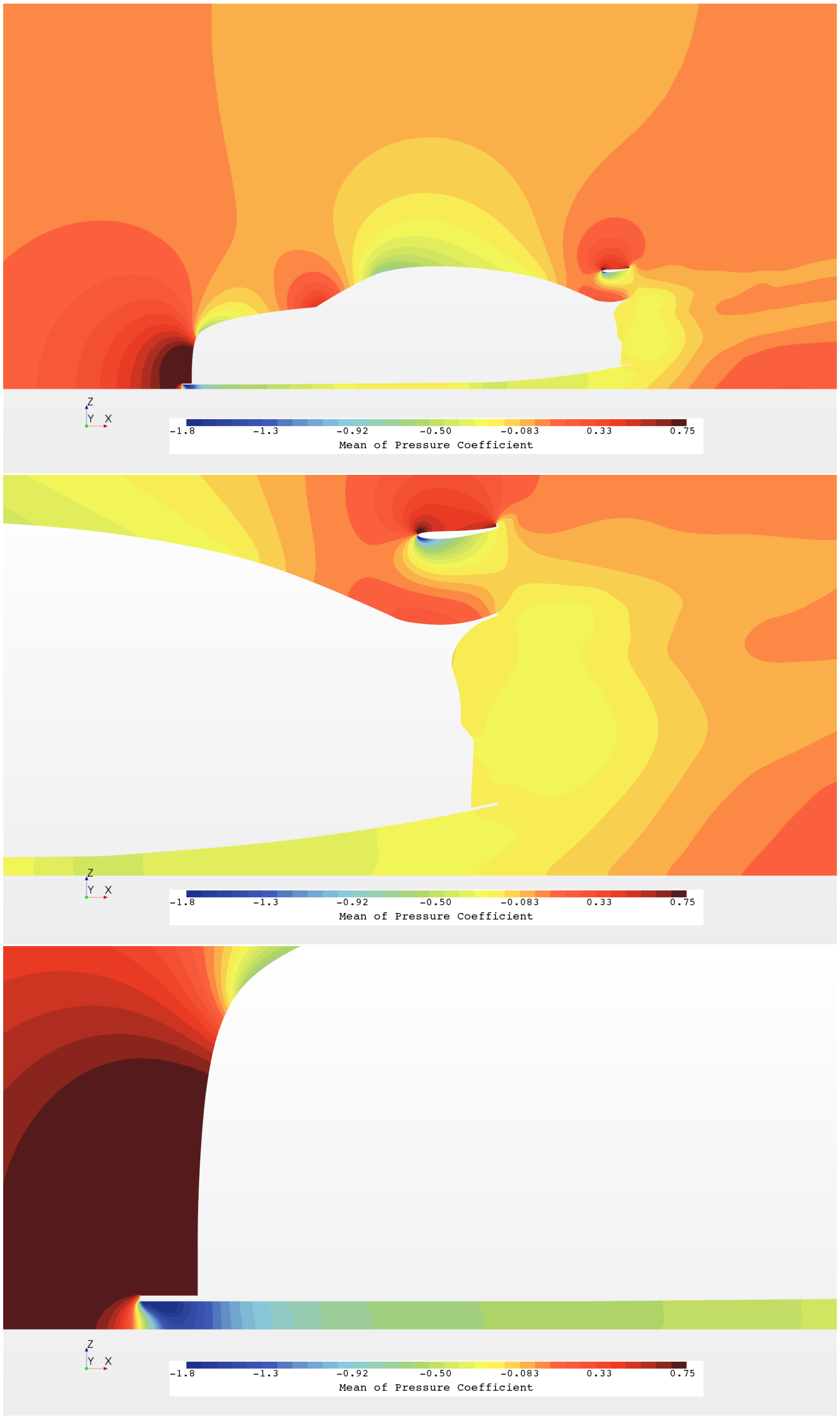

Figure 49: Y=0" C_P slice of the DrivAer-GTR Baseline.

7.3 DrivAer-GTR Data Processing

Over the course of this dissertation, the data processing techniques for analyzing acceleration-deceleration data have steadily improved. During the bluff body investigation of a channel mounted square cylinder, force data was grouped into respective acceleration and deceleration periods and then ensemble averaged. For the DrivAer study, sufficient data was not available, resulting in the need for using least-squares polynomial fitting to determine average forces at the reference velocity. For the DrivAer-GTR study, sufficient data is available, although not an ideal amount, but we will use ensemble averaged forces, least-squares polynomial fits and low-pass filtered methods to determine their sensitivity towards determining an averaged force.

Figure 51 presents the instantaneous drag force versus time for the entire DrivAer-GTR acceleration simulation of 15 periods with the accelerating and decelerating components colored as red and blue respectively. All time dependent forces were segregated into 15 separate periods and their respective acceleration and deceleration phases, allowing for analysis of each period. Note that the simulation was initialized from the non-accelerating transient baseline solution of which already had 4 s of simulated run time, however the first deceleration was omitted from this analysis. Viewing the drag force versus time is not sufficient for determining any trends, thus Figure 52 organizes the instantaneous drag force versus Velocity. Here, the non-accelerating drag force is indicated by the black circle, determined from time-averaged transient data and is extrapolated via the black dotted line with force coefficient data. Without any data processing a clear trend is present that the drag force is not equivalent for majority of tested velocities and only approaches equality when V_{ref} acceleration rates are small. As demonstrated in previous studies in this dissertation, the results here are as expected, acceleration causes the drag force on the body to be greater than non-acceleration and the opposite is true for deceleration. The lift force in Figure 53 does not demonstrate a clear trend due to aerodynamic induced noise on the body, observations of the lift will be drawn later after a clearer trend can be demonstrated. The aerodynamic efficiency of the vehicle (lift over drag) is shown in Figure 54 where an interesting trend is present, during acceleration the vehicle experiences a lower overall efficiency (a larger negative number here indicated more down force for given drag) and during deceleration the vehicle's efficiency increases. We will find later that this is due to both an increase in drag and a reduction of down force during acceleration. The same analysis was carried out on the rear wing, where drag versus velocity can be seen in Figure 55 where the opposite trend in comparison to the overall body is observed. In addition, an asymmetry in the drag between the three cases is present, where the offset to the decelerating forces is greater than the accelerating from non-acceleration. This trend was not expected and requires further investigation and discussion, initial speculation points towards bulk flow features of the vehicle influencing the overall performance of the wing. This speculation is supported by the lift force of the wing in Figure 56 where a reduction in down force is present during the accelerating case and an increase is present in the decelerating case. Further investigation of the ensemble averaged velocity field determined that during deceleration there is an increase in the upward component of the wake behind the vehicle and an downward increase of the velocity outboard of the vehicle in Figure

68 which may drive improved performance of the wing as if it were at a higher angle of attack. Figure 57 demonstrates no clear trend for the wing's aerodynamic efficiency.

To clearly report forces between cases, several techniques were applied to transient period data. First, 15 points of force data were extracted for each case, once for each period when $V_{ref}(t) = 40\ \mathrm{m\,s^{-1}}$, these forces were then averaged for each successive period, as shown in Figure 50 as black circles. Over 15 periods the drag force does appear to converge to a value, however it is clear that both the polynomial and low pass filter methods converge to a common solution in fewer periods. As a second method for determining forces, a least squares polynomial-fit was implemented to each period individually and the drag force from each successive period was averaged as before. Again, this method is also shown in Figure 50 as green squares, and demonstrates considerable improvement to convergence of drag force in comparison to ensemble averaging instantaneous forces. The third method was to apply a low-pass filter, removing all frequencies from force data greater than 20 Hz and then ensemble averaging each period. An example of this for the body drag is shown in Figure 62, which considerably reduces the noise of the force signal. Convergence of the low-pass filter method is shown as purple triangles in Figure 50 and indicates convergence in as little at 8 periods. In addition to low-pass filtering forces, a Fast Fourier Transform (FFT) was implemented to look at energy spectra between the accelerating and decelerating cases. The FFT of drag force is shown in Figure 64 for both accelerating and decelerating periods where notably the energy spectra declines above 250 Hz as expected for a IDDES simulation. Additionally, no discernible differences for drag force were visible in the energy spectra between cases. Interestingly, there is a dif-

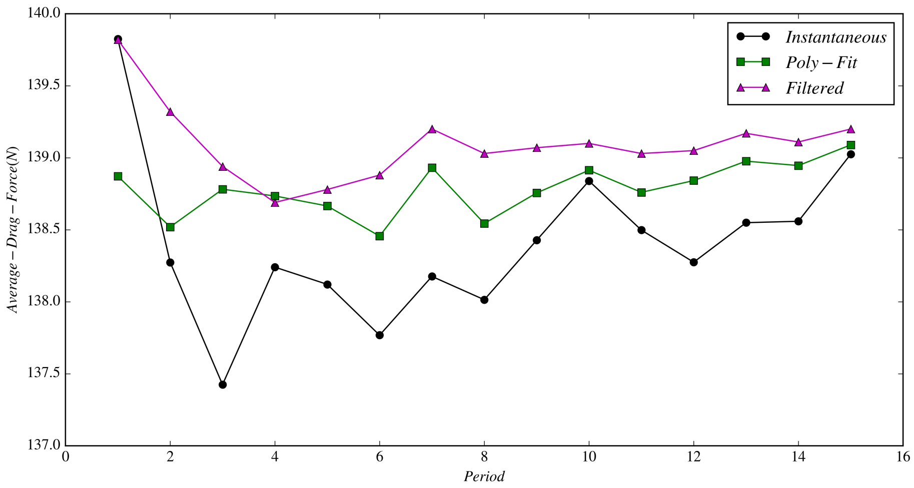

Figure 50: Convergence of drag force (N) versus period count with respect to method.

ference of energy spectra for lift forces present in Figure 65 and Figure 66, but only above 500 Hz, indicating variation from the RANS portion of the simulation near the wall, possibly emanating from a change in vorticity flux previously mentioned in the cylinder investigation. Regardless of data processing technique, the outcome from each varied only slightly, thus the results of each are plotted in poly-fit plots and will not be elaborated on further. Results reported are result of low-pass filtering technique.

Scalar field variables were ensemble averaged by extracting planar cut data for each period, resulting in 30 total data sets to be averaged into their respective acceleration deceleration phase. While 15 periods were sufficient for determining body forces, the same is not true for the convergence of scalar field variables of V_r and ω^*. Large scale flow features are visible, however wake values still contain visible amounts of noise.

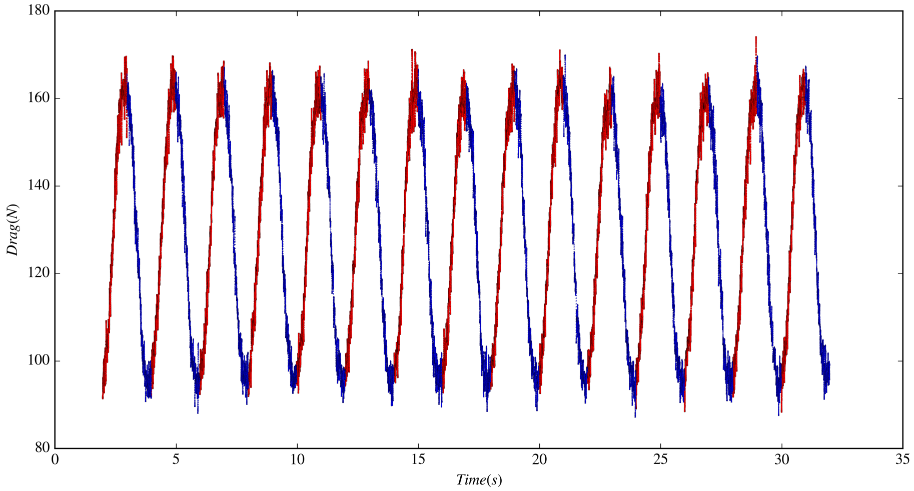

Figure 51: The DrivAer-GTR drag force (N) versus time (s).

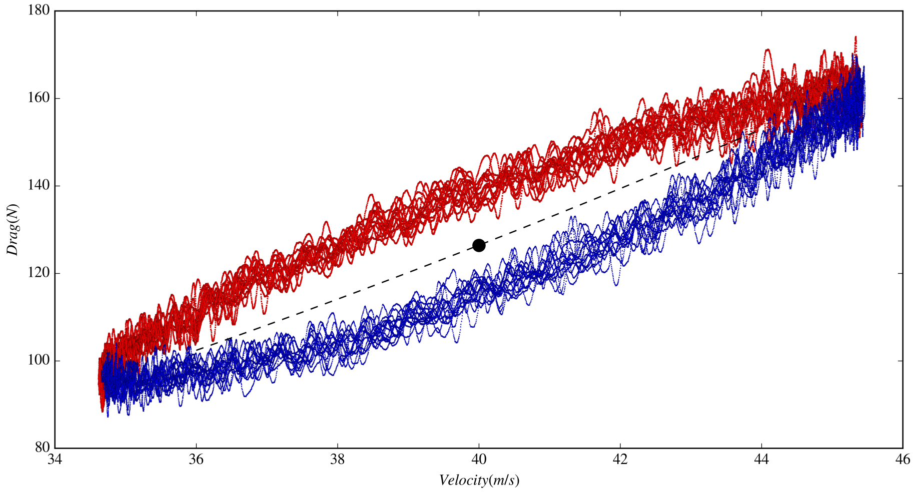

Figure 52: The DrivAer-GTR drag force (N) versus velocity (m/s).

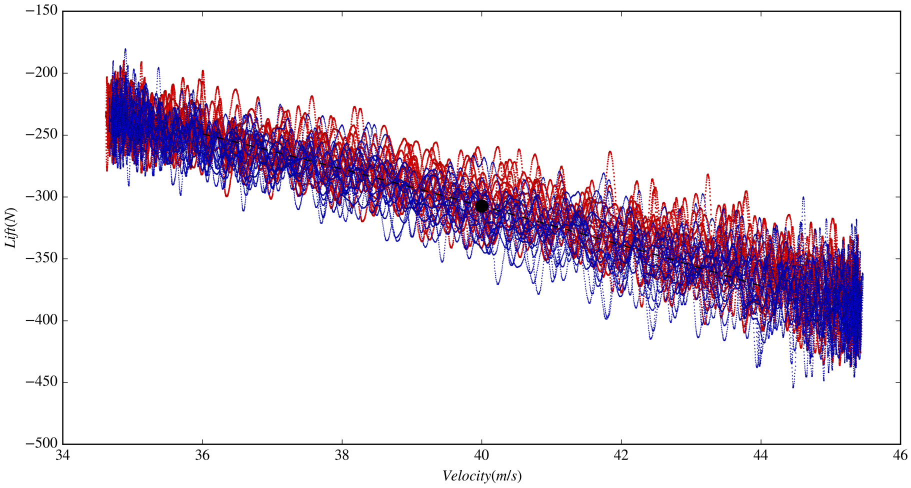

Figure 53: The DrivAer-GTR lift force (N) versus velocity (m/s).

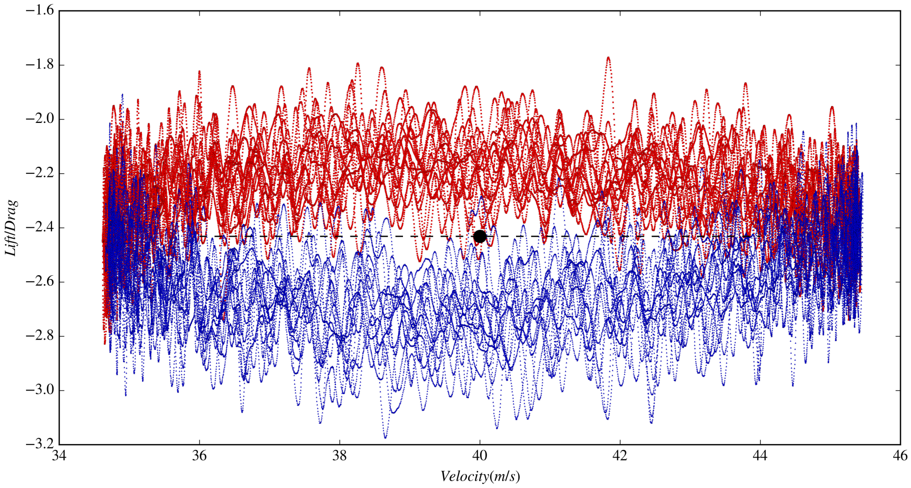

Figure 54: The DrivAer-GTR efficiency (lift/drag) versus velocity (m/s).

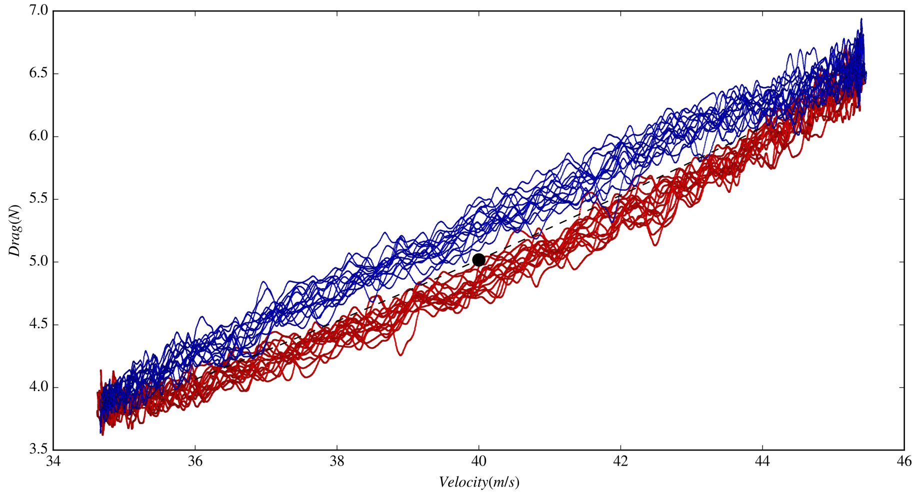

Figure 55: The DrivAer-GTR wing drag force (N) versus velocity (m/s).

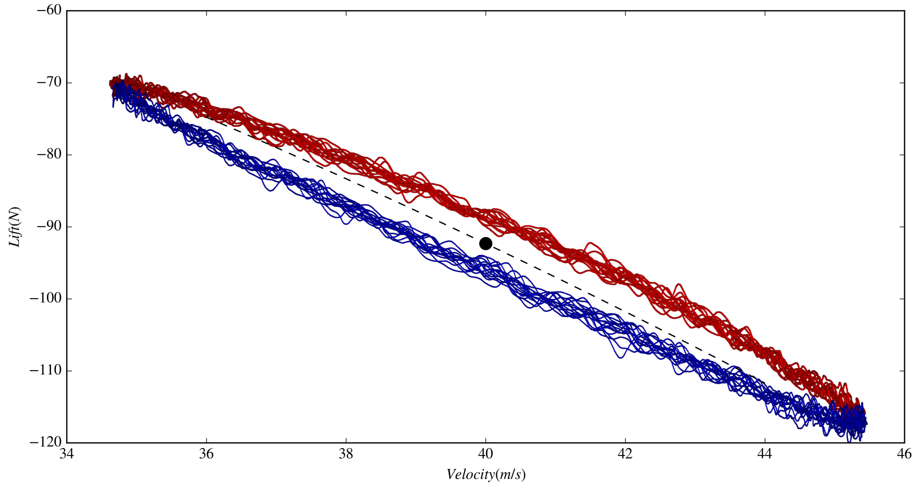

Figure 56: The DrivAer-GTR wing lift force (N) versus velocity (m/s).

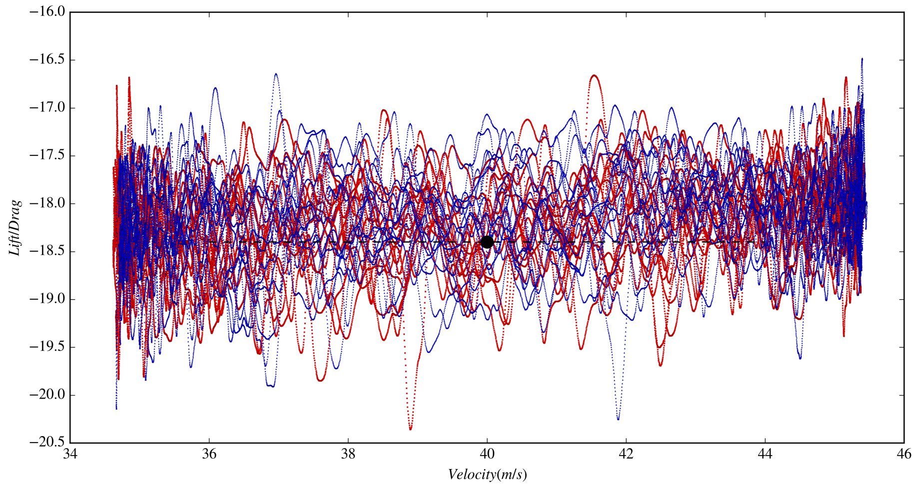

Figure 57: The DrivAer-GTR wing efficiency (lift/drag) versus velocity (m/s).

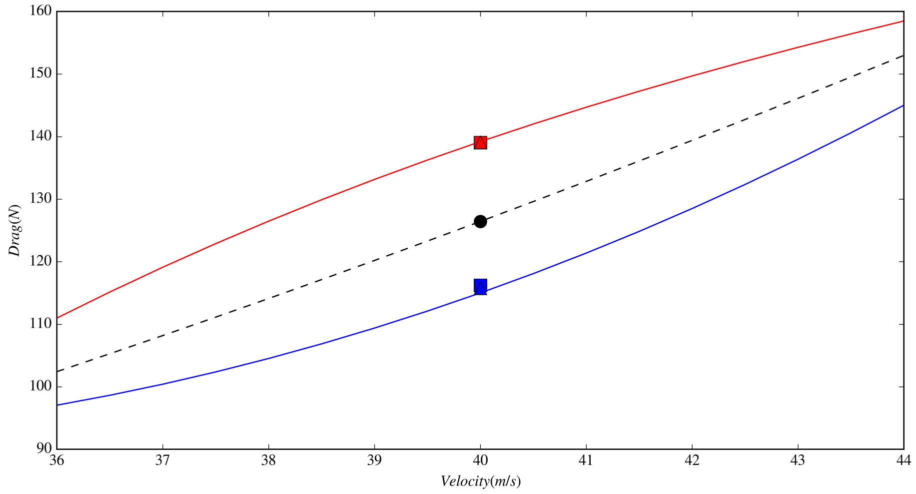

Figure 58: The DrivAer-GTR drag (N) signal represented as polynomial best fit lines versus velocity (m/s).

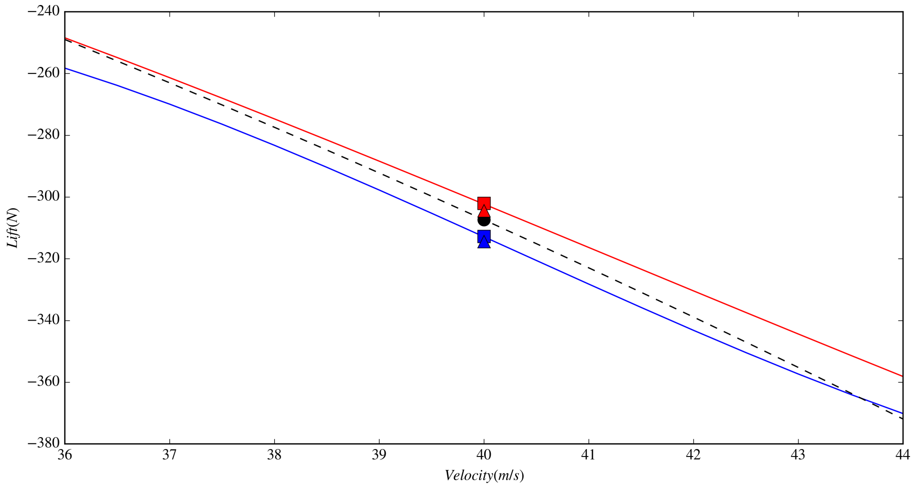

Figure 59: The DrivAer-GTR lift (N) signal represented as polynomial best fit lines versus velocity (m/s).

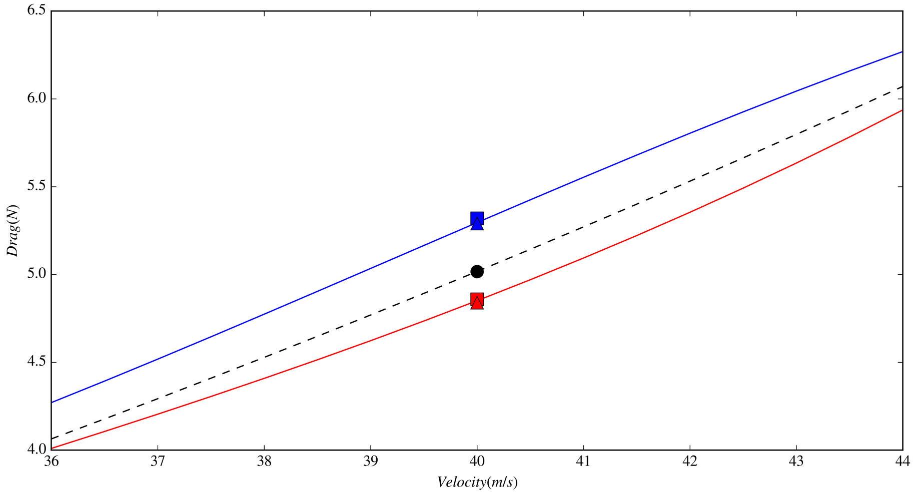

Figure 60: The DrivAer-GTR Wing drag (N) signal represented as polynomial best fit lines versus velocity (m/s).

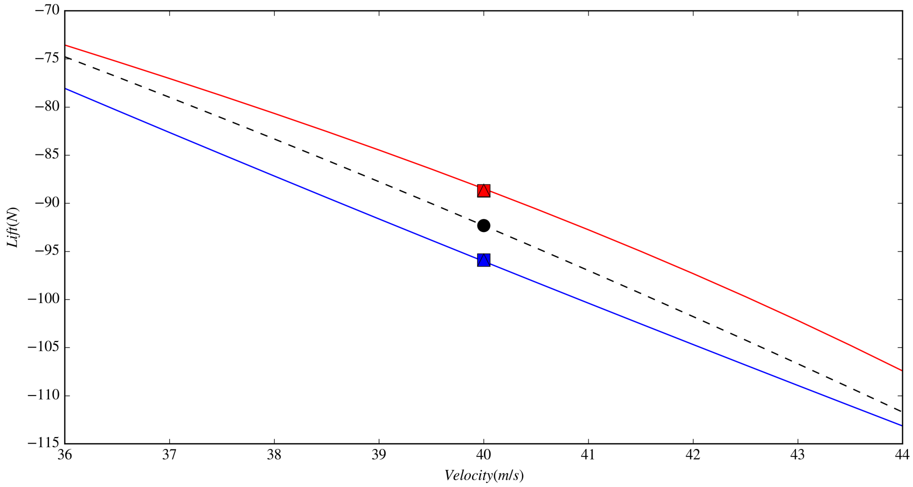

Figure 61: The DrivAer-GTR Wing lift (N) signal represented as polynomial best fit lines versus velocity (m/s).

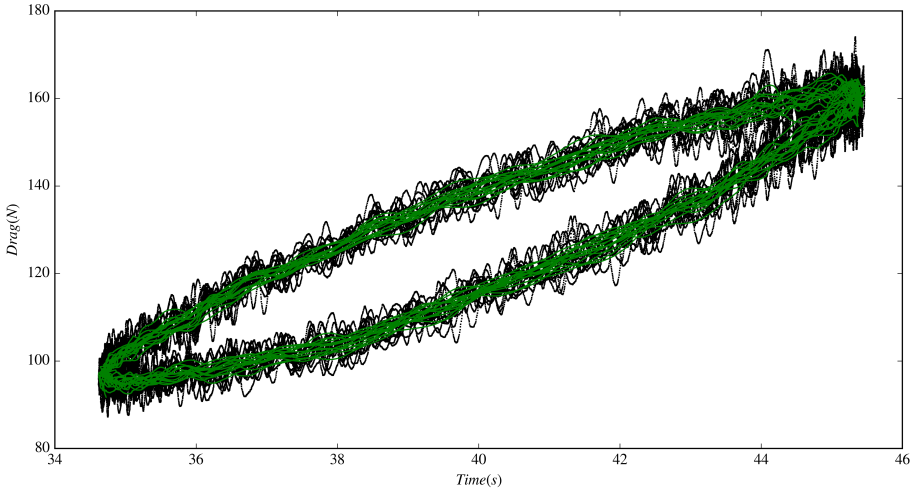

Figure 62: The DrivAer-GTR drag (N) signal with low-pass filtering with raw signal versus velocity (m/s).

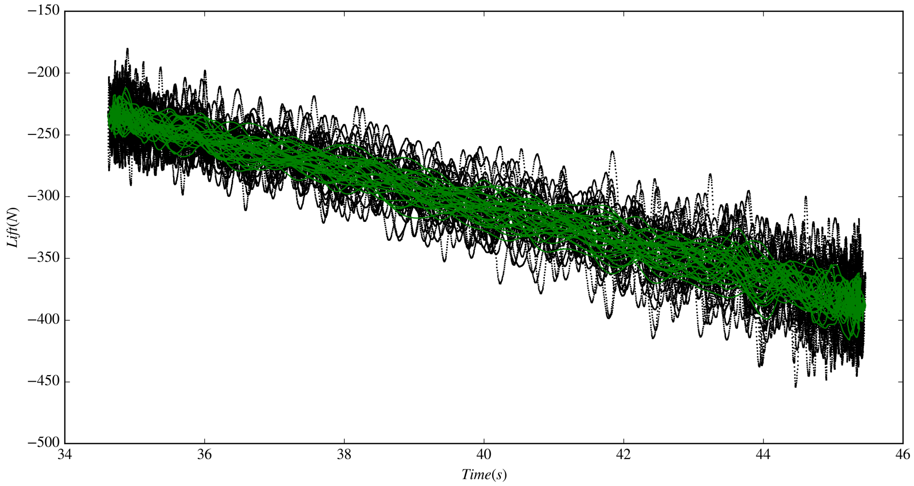

Figure 63: The DrivAer-GTR lift (N) signal with low-pass filtering with raw signal versus velocity (m/s).

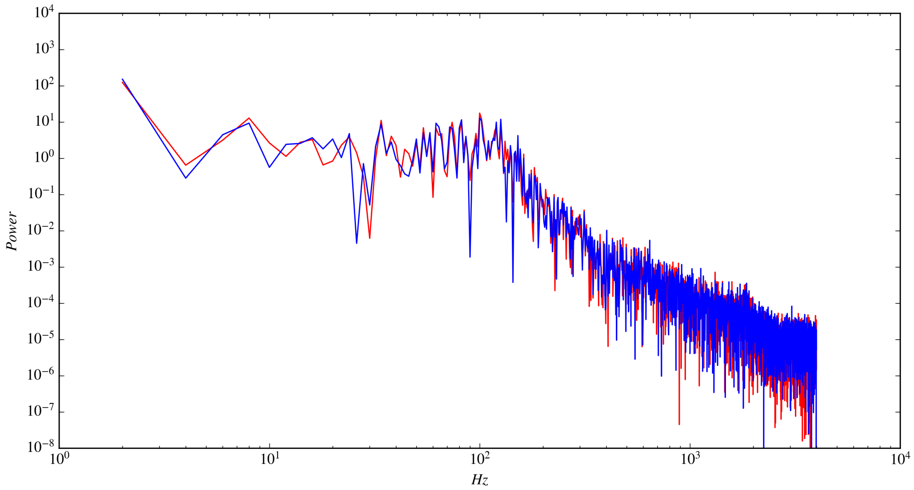

Figure 64: Fast Fourier Transform power spectrum of DrivAer-GTR Drag (N).

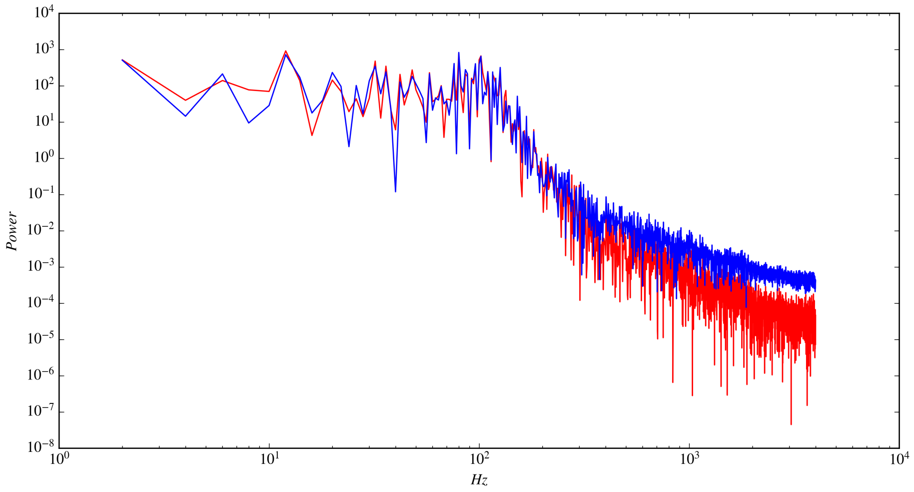

Figure 65: Fast Fourier Transform power spectrum of DrivAer-GTR Lift (N).

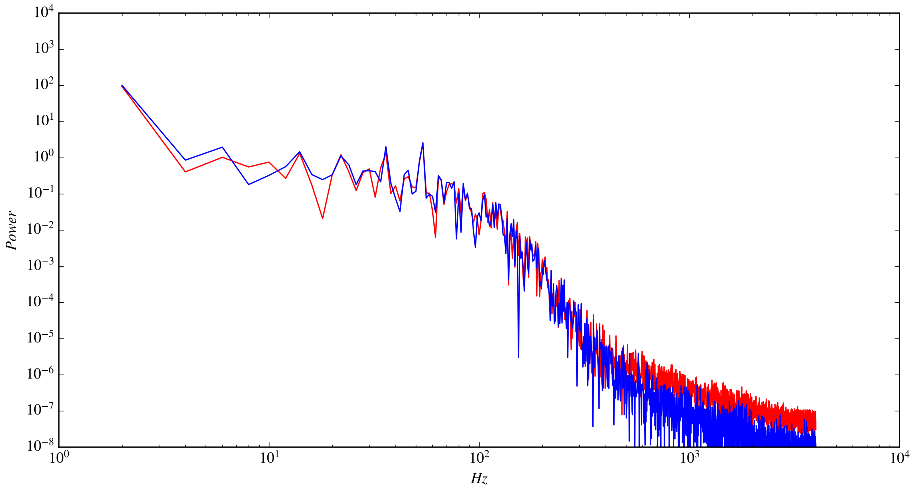

Figure 66: Fast Fourier Transform power spectrum of DrivAer-GTR Wing Lift (N).

7.4 DrivAer-GTR Results

The total run time for 15 accel-decel periods was 408.6 hours (17 days) spanning 29,419 CPU hours and while more periods would be desired to obtain a stronger scalar field ensemble average, data analysis results indicate that acceptable force convergence was achieved. Table 10 summarizes overall forces and lift distribution for decelerating, non-accelerating and accelerating conditions, all taken at equivalent $V_{ref}(t) = 40\,\mathrm{m\,s^{-1}}$. Considerable variations in the front lift percentage were not observed between the three cases. Variations in overall drag force are large in comparison to variations in lift, where the total drag varies ±8.5% from non-accelerating, while the lift only varies ±1.5%. Wing drag experiences the opposite trend in regards to drag force, increasing 5% during deceleration and decreasing 3.7% during acceleration. Both the total vehicle down force and wing down force increase during deceleration, and is determined to be due to changes in flow down the rear glass. During deceleration, there is an increase in vorticity near the wall, delaying separation down the rear glass, effectively increasing the angle of attack on the rear wing. The shift in vorticity can be seen in the delta of A-D in Figure 67 where more vorticity is present above the trunk for the decelerating case. Additionally, the departure angle of the wing wake increases (more upward component) for the decelerating case, also indicating greater wing performance.

7.5 Modeling

An important aspect of the acceleration-deceleration simulation herein is to determine the Inertial coefficient for the DrivAer-GTR with intention to model other

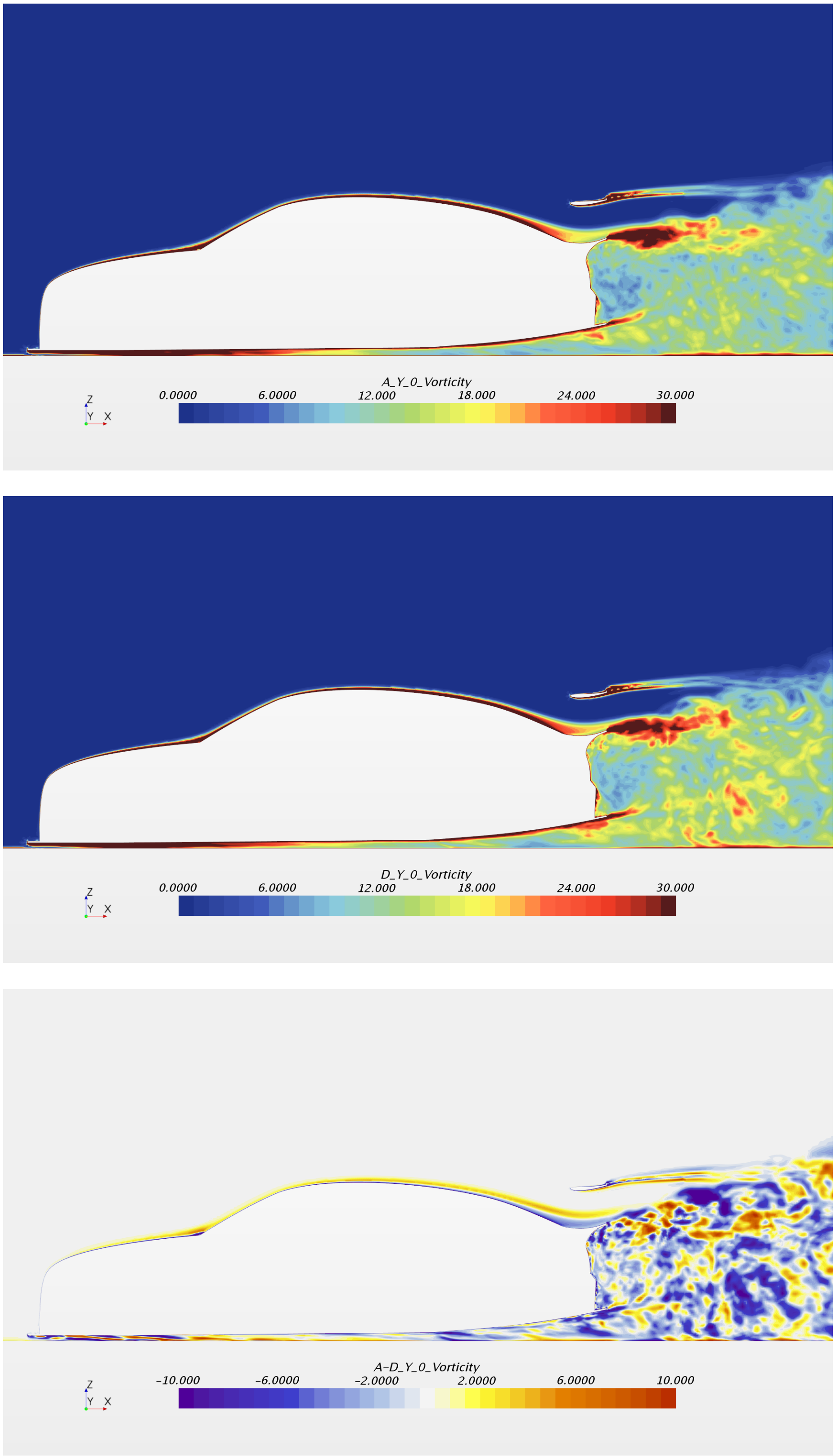

Figure 67: ω^* for deceleration (top), acceleration (middle) and acceleration-deceleration (bottom) on vehicle centerline Y=0.

Table 10: Ensemble averaged body forces based on Low-pass filtered data at $V_{ref} = 40\ \mathrm{m\,s^{-1}}$ for the DrivAer-GTR at $a_x = -1.5G$, $a_x = 0$ and $a_x = 1.5G$.

a_x	Drag (N)	Lift (N)	Wing Drag (N)	Wing Lift (N)
$-1.5G$	114.99	-314.43	5.29	-95.89
0	126.43	-307.38	5.02	-92.31
$1.5G$	139.09	-304.42	4.84	-88.66

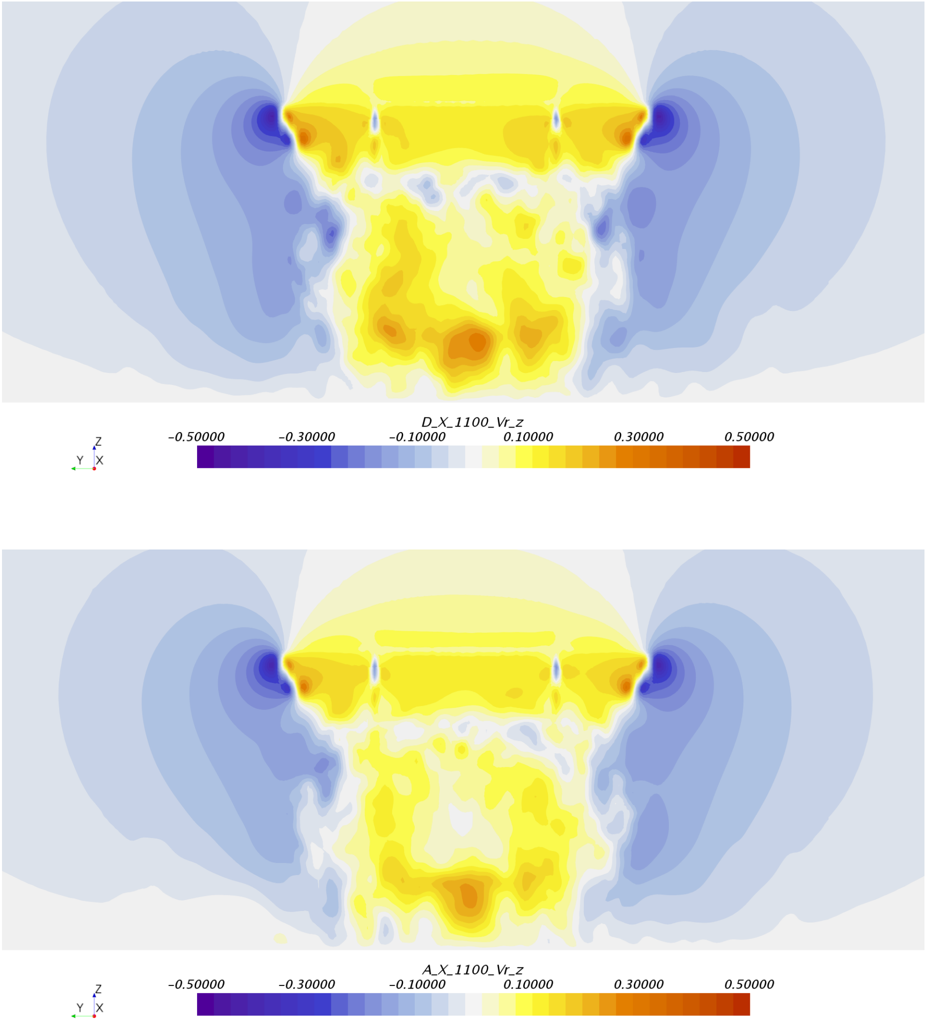

Figure 68: Vr_z for deceleration (top) and acceleration (bottom) directly behind the vehicle at X=1.1 m.

Table 11: Inertial coefficients for the DrivAer-GTR and wing.

a_x	C_{MD}	C_{ML}	$WingC_{MD}$	$WingC_{ML}$
$-1.5G$	1.15	0.61	11.0	137.0
$1.5G$	1.43	0.6	-6.39	137.7

acceleration conditions. Recall that the Morison Equation Equation 2 adds to the non-accelerating drag force, accounting for additional forces due to acceleration. If $C_M = 1$, then the additional force due to acceleration is a resultant of the displaced fluid volume by the body, otherwise the inertial coefficient includes other effects which are due to the shape of the test body and other viscous contributions of the flow. Inertial coefficient results from the current study are shown in Table 11. To calculate the coefficient, Equation 2 was set equal to the ensemble averaged drag and lift force, then all components are known except for the inertial coefficient, simple algebra produces the desired quantity.

For the DrivAer-GTR undergoing $\pm 1.5G$ longitudinal acceleration, the inertial coefficient is nearly constant for total lift and wing lift forces, indicating that there is no asymmetry present in lift forces for the two cases. However, the inertial coefficient for the total and wing drag forces do experience asymmetry. For total drag force, the inertial coefficient varies from 1.15 to 1.43 for acceleration and deceleration indicating that effects beyond displacement of volume are present. Additionally, the rear wing experiences unexpected CM trends, with a negative value during acceleration. This is attributed to the wing's orientation relative to the body, causing flow field variations which drive wing performance such as the incoming flow angle. To check the validity of the Morison Equation for the DrivAer-GTR and the computed

Intertial Coefficients, a polynomial was fit to $V_{ref}(t)$ and then differentiated to obtain $a_x(t)$. Then, along with calculated inertial Coefficients, the Morison Equation was calculated for one acceleration-deceleration period and overlayed with the transient drag signal in Figure 69. Overall, the Morison Equation predicts force response to velocity and acceleration changes with good agreement and can be seen as the solid red and blue dashed and dotted lines. Notably, there are two curves plotted here in addition to raw forces (opaque blue and red markers) and predicted non-accelerating forces (black), where the dotted red line represents the predicted response to the accelerating inertial coefficient, and the blue dotted line resulting from the inertial coefficient. As expected, the accelerating inertial coefficient predicts the acceleration phase with higher accuracy, where the decelerating inertial coefficient predicts the deceleration phase with higher accuracy. Interestingly, the predicted force response begins to vary considerably beyond $\pm 2\,\mathrm{m\,s^{-1}}$ of $V_{ref} = 40\,\mathrm{m\,s^{-1}}$ at the high and low velocities where acceleration rate changes sign, possibly due to another force resulting from jounce, the derivative of acceleration. The predicted response of lift force from total inertial coefficients are presented in Figure 70 where in addition to the lines plotted in the previous drag force prediction, the polynomial least-squares fits are plotted to demonstrate the ensemble averaged trend of the forces for acceleration and deceleration from $\pm 4\,\mathrm{m\,s^{-1}}$ of $V_{ref} = 40\ \mathrm{m\,s^{-1}}$. Considering that the variation in lift force is small between acceleration and deceleration cases, the force response does significantly deviate from predicted values as the acceleration rate changes sign, as seen previously with drag force. As previously mentioned, the rear wing demonstrates inverse drag behavior in comparison to the total drag force, resulting in an increase

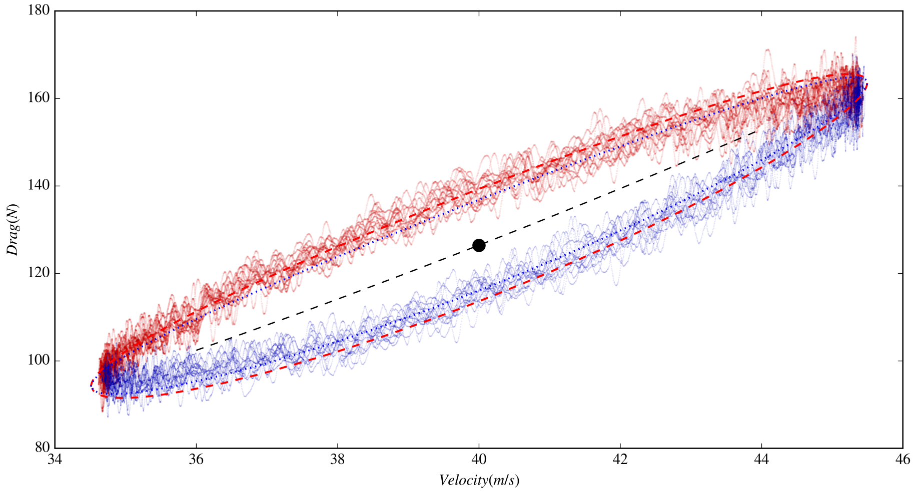

Figure 69: Drag Force (N) with force predicted by the Morison Equation and inputs: $V_{ref}(t)$,$a_x(t)$,CD,CMa,CMd

of drag during deceleration. Overall drag force response is predicted well yet again in Figure 71 with the Morison Equation closest to the reference velocity of $40\,\mathrm{m\,s^{-1}}$ and experiences considerable deviations outside of $\pm 4\,\mathrm{m\,s^{-1}}$. The same is observed for the rear wing lift force response from the Morison Equation in Figure 70, noting that the predicted responses are nearly identical for the wing, due to the inertial coefficients being so close on values.

7.6 DrivAer-GTR Concluding Remarks

In order to investigate acceleration aerodynamics of a high performance road vehicle, the DrivAer fastback model was drastically modified from a vehicle with near zero lift force to a vehicle with a low ground clearance and lift coefficient above -0.900. A rear wing was also added to investigate accelerating effects on high lift creating devices. The resulting DrivAer-GTR model, will be made available as an open-source geometry, aiding motor sport aerodynamic development and CFD methodologies for high lift ground vehicles. Initial hypothesis would lead one to believe that during lon-

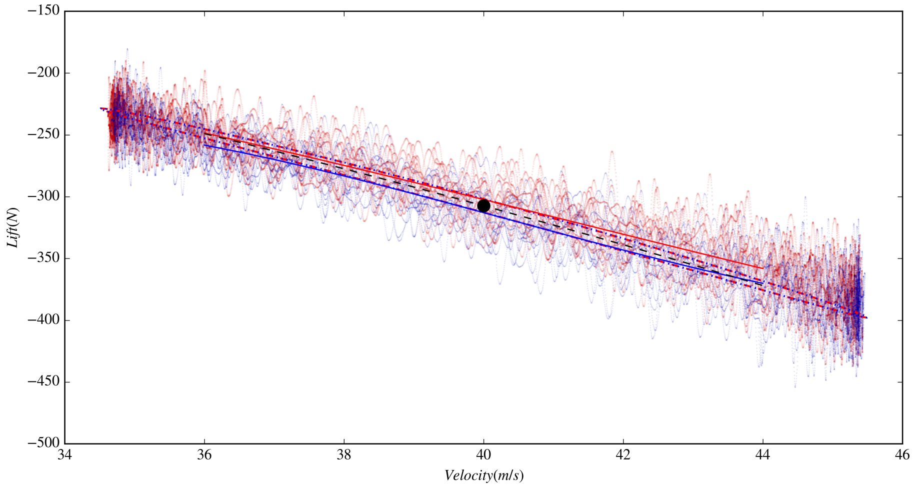

Figure 70: Lift Force (N) with force predicted by the Morison Equation and inputs: $V_{ref}(t)$,$a_x(t)$,CD,CMa,CMd

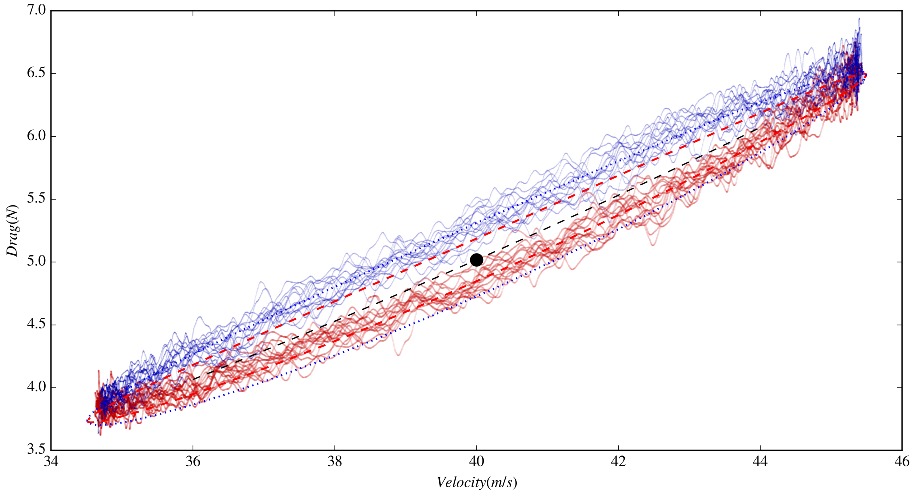

Figure 71: Wing Drag Force (N) with force predicted by the Morison Equation and inputs: $V_{ref}(t)$,$a_x(t)$,CD,CMa,CMd

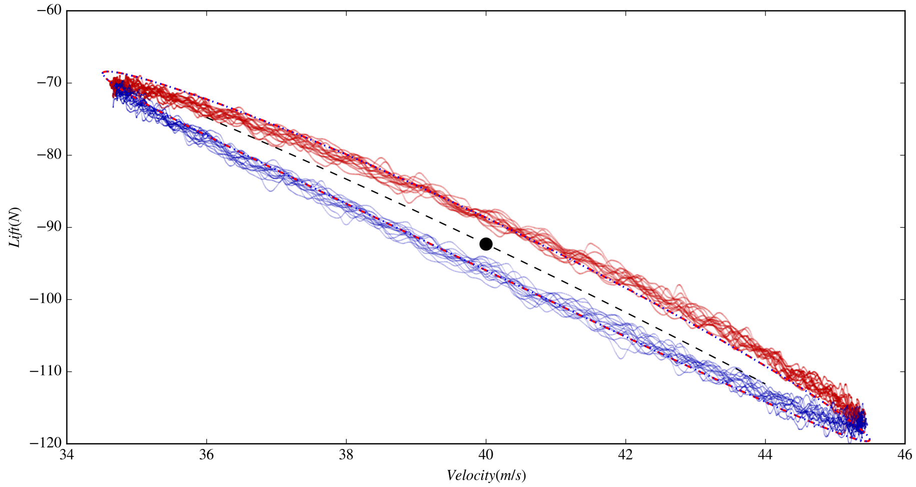

Figure 72: Wing Lift Force (N) with force predicted by the Morison Equation and inputs: $V_{ref}(t)$,$a_x(t)$,CD,CMa,CMd

gitudinal acceleration, only the drag force would be measurably different, leaving lift forces to be well within the error of CFD measurement capabilities. This hypothesis was shown to be correct, resulting in small variations of total lift forces near ±2%, with rear wing lift force variations near ±3%. Calculation of the inertial coefficients via the Morison Equation allow for the calculation of body forces in response to velocity and acceleration inputs. This will potentially aid in the future development of dynamic road vehicle handling models.

CHAPTER 8: APPLICATIONS

The methods and knowledge compiled in this dissertation have many potential applications towards unsteady mean road vehicle aerodynamics. The following subsections outline this potential.

8.1 Consumer Road Vehicles

For the average road vehicle consumer, large accelerations would generally occur during aggressive braking for collision avoidance maneuvering. For driver in the loop collision avoidance, the anti-lock braking controls provide maximum tractive force for deceleration. However for the future of autonomous driving, the information presented in this dissertation could be applied to predictive models, inevitably feeding autonomous systems to minimize damage in an unexpected accident. Another area for potential use of this knowledge would be the modeling of onset and vanishing of wind gusts for lane keeping systems. Also, large shipping vehicles that are susceptible to blow over may benefit from this type of modeling an analysis.

8.2 High Performance Vehicles

For high performance road vehicles where acceleration and deceleration are commonplace, the application of information herein could potentially expand design envelopes into another degree of freedom. This would allow scientists and engineers to also improve aerodynamic performance for the accelerating case as computational resources increase into the foreseeable future. Additionally, this information could be used to optimize land speed records, accounting for additional force required to accelerate to test speeds.

8.3 Dynamic Modeling

An intriguing area for applying knowledge from this dissertation is into dynamic modeling simulations. In general, aerodynamic maps for simulation are a function of five variables: wind speed, yaw angle, pitch angle, roll angle and distance of the body from the road. The information in this dissertation would allow for the immediate implementation of adding an additional degree of freedom to an aerodynamic map: longitudinal acceleration. An engineer would need to ask at first, "how important is this additional degree of freedom to my simulation?" To answer that a back of the envelope analysis should occur...

If the full scale DrivAer-GTR were to have 500 brake horsepower (power available at the crankshaft), then the top speed of the vehicle in the configuration tested herein would be 204 mph ($91.2\,\mathrm{m\,s^{-1}}$) based on the power equation (drag equation multiplied by velocity). To predict the variation of drag force for an aggressive braking maneuver ($-19\ \mathrm{m\,s^{-2}}$) from top speed down to a tight radius corner 55 mph ($25\ \mathrm{m\,s^{-1}}$) and then accelerating ($10\ \mathrm{m\,s^{-2}}$) back to top speed, a hypothetical velocity signal was created. Figure 73 displays the input velocity (blue triangles) which were then fit with a high order polynomial (red line) to be differentiated for the acceleration rate (green line).

Then, using the Morison Equation the velocity and acceleration signals can be

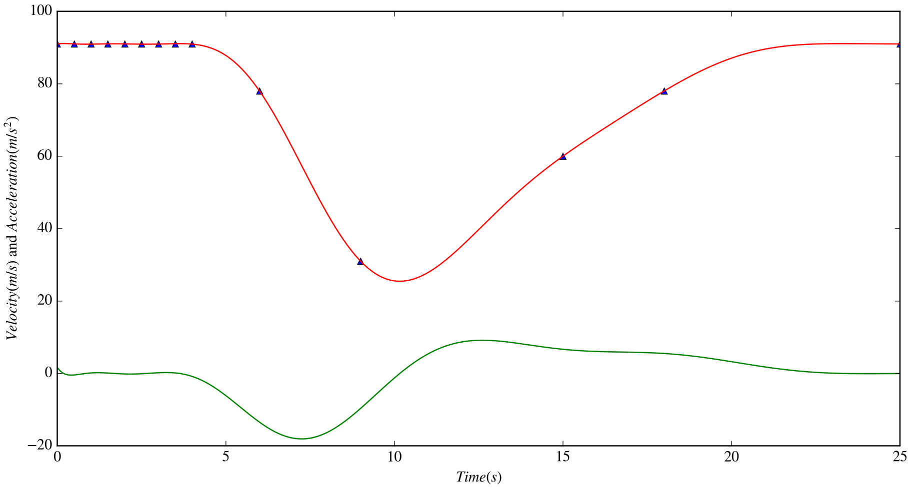

Figure 73: A hypothetical velocty and acceleration trace for a high performance road vehicle at terminal velocity heavily braking for a corner and then accelerating.

applied to predict the drag force for the full scale DrivAer-GTR during the same maneuver and are presented in Figure 74. The black line represents the Morison Equation with the inertial coefficient set to 0, and the red line is the result of the Morison Equation with the inertial coefficient set equal to the average of acceleration and deceleration results of the DrivAer-GTR scale study herein. The point to be absorbed by the reader in this plot is that the overall drag force on the vehicle is dominated by the velocity of the vehicle, not the acceleration rate. However, there are noticeable differences for the drag force at lower velocities, which are better demonstrated as a ratio of force in Figure 75.

The drag force ratio is the ratio of drag force with acceleration contribution to drag force without acceleration contribution. During initial onset of acceleration near max velocity, the overall contribution of acceleration starts small but quickly grows to greater than 20% contribution at 8 s into the hypothetical maneuver during peak acceleration and vehicle speed is near 90 mph (40 $\mathrm{m\,s^{-1}}$). The peak of the ratio of

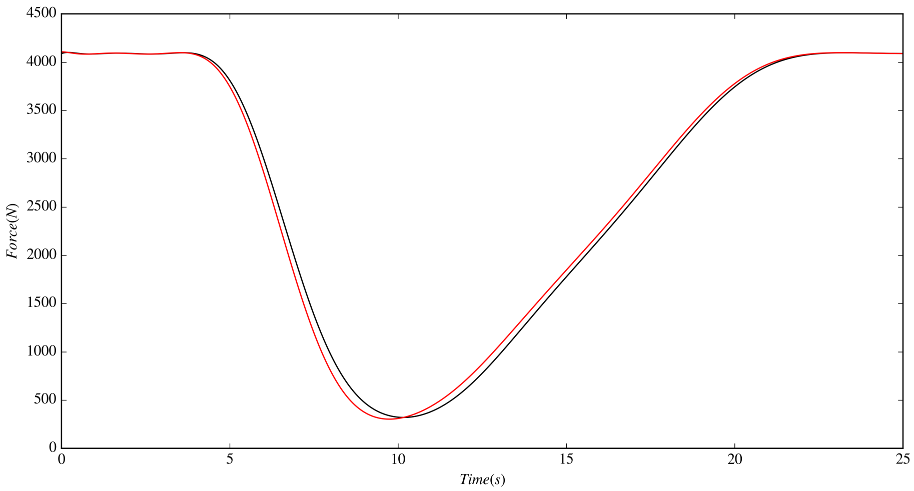

Figure 74: Forces for a hypothetical braking maneuver.Black=no acceleration force included Red=acceleration force included

22% occurs near 9 s near the end of the deceleration when vehicle velocity is 56 mph (25 $\mathrm{m\,s^{-1}}$). Note that during the deceleration of the vehicle, the reduction in drag force due to aerodynamic deceleration contribution would need to be absorbed by the vehicle's brakes to maintain the same vehicle position along the track in comparison to a vehicle that did not experience this contribution. During our hypothetical maneuver, the vehicle eventually makes the corner and then begins to accelerate back to top speed, the maximum ratio determines an increase of drag of 13% at 12 s into the maneuver near peak acceleration of $10\,\mathrm{m\,s^{-2}}$ with a vehicle velocity of 90 mph (40 $\mathrm{m\,s^{-1}}$). Note that during acceleration, this additional force would require additional power from the drivetrain (be it internal combustion engine or electric motor) to maintain the same progress along the course in comparison to a vehicle that did not experience aerodynamic acceleration contributions.

To put the discrepancy of forces into terms of power, Figure 76 compares the delta in power of no contribution due to aerodynamic acceleration minus power with

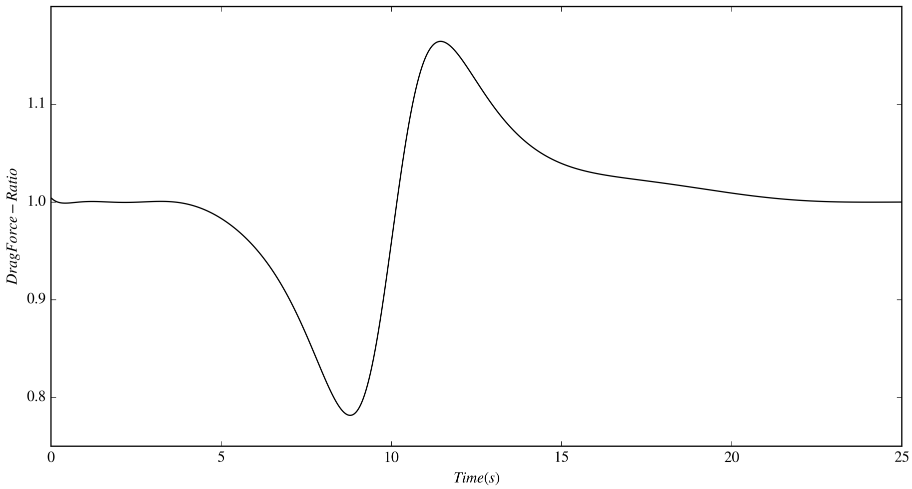

Figure 75: Drag force ratio of including acceleration forces to not included acceleration forces for a hypothetical braking maneuver.

aerodynamic acceleration. Notably, the deceleration portion would require as much as an additional 17 horsepower from the braking system to decelerate at the same rate of a vehicle that had no aerodynamic deceleration contributions to drag force, and during acceleration the powertrain would require an additional 6 horsepower for a sustained period of nearly 5 s. While this may seem as an insignificant additional power requirement for a 500 horsepower engine, consider a 24 hour race such as the 24 hour of LeMans, where there would be 7 instances of the hypothetical maneuver presented here for each lap, and in the 2010 race the winning team completed nearly 400 laps. The power discrepancy presented here due to aerodynamic acceleration and deceleration could potentially alter engineering predictions for brake wear, fuel consumption and predicted distance traveled over the course of an event.

The same can also be applied to the lift force variation due to longitudinal acceleration as displayed in Figure 77, although the variation in lift force is not large of a contribution in comparison to drag, the result is interesting that 4% more down force

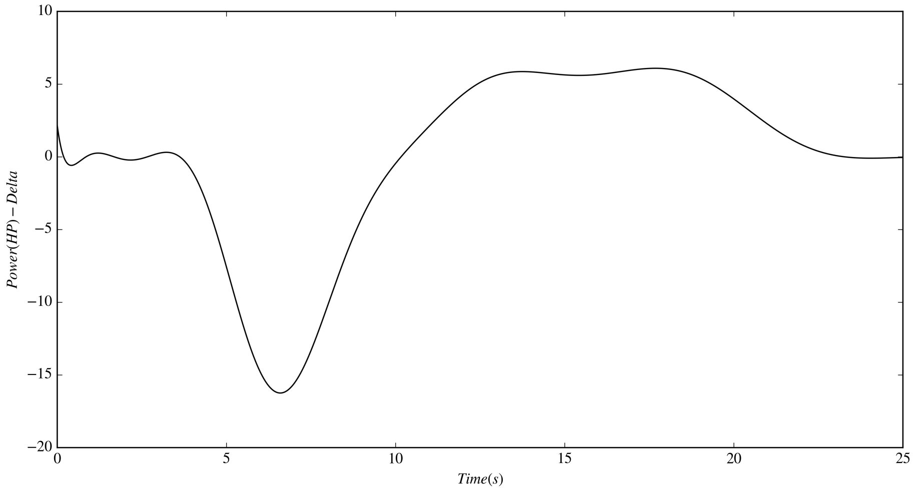

Figure 76: Power delta (Hp) of including acceleration forces to not included acceleration forces for a hypothetical braking maneuver.

is available to generate tractive braking force at the road and roughly 3% less down force is available during acceleration for traction.

Note that this process is not limited to the longitudinal acceleration of road vehicles and could be applied to several other degrees of freedom in the future, such as lateral acceleration during cornering and rolling axis' such as pitch, roll and yaw rates.

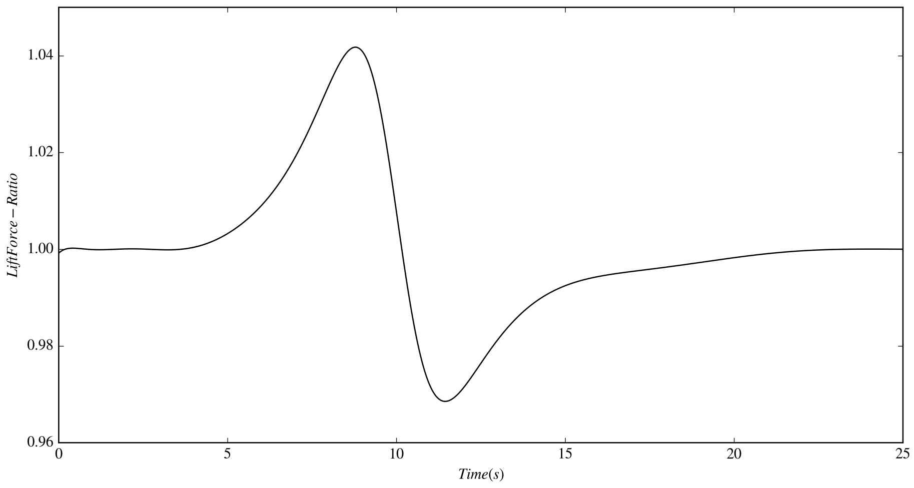

Figure 77: Lift force ratio of including acceleration forces to not included acceleration forces for a hypothetical braking maneuver.

CHAPTER 9: CONCLUSIONS

This dissertation has attempted to answer the question of “is acceleration aerodynamics important for road vehicles?” While this question is quite vague, it is the important first step for road vehicle aerodynamicists before investing time and resources. To answer this question, an entirely new process and mindset had to be created and tested via IDDES CFD simulation, requiring the linkage of many prior literature and journal publications. The applied process of periodically accelerating and decelerating the inlet velocity of a simulated wind tunnel and then ensemble averaging both forces and spatial flow field data allowed for the investigation of the impact of acceleration aerodynamics. Initially, the process was tested on a simple bluff body, a channel mounted cylinder, which could easily be validated against a wealth of experimental and simulation data before performing an acceleration simulation. After the process was scrutinized, it was then applied to a realistic road vehicle geometry, the DrivAer model, and then to a high performance road vehicle which was created for this exercise, the DrivAer-GTR model. Major conclusions from this dissertation have already been summarized in their respective chapters, but are summarized here to finalize a conclusion.

9.1 Bluff Body Acceleration

- As a first step a process was developed for obtaining ensemble averaged force and flow field variables of a channel mounted cylinder undergoing accelerating conditions.

- After processing force data a clear trend emerged that during acceleration the drag force on the cylinder increased 44% and during deceleration decreased 47% in comparison to non-accelerating conditions resulting in inertia coefficients of C_M=1.71 during acceleration and C_M=1.91 during deceleration.

- The C_L^{rms} values also varied during each distinct case, indicating that complex flow phenomenon were present and driving instability of the wake in the accelerating case. This effect was concluded to be from a reduction of vorticity flux during the accelerating case and the longitudinal velocity gradient causing every other shedding vortex to be scattered away from the x-axis, driving instability in the wake.

- The size of the leading edge separation was considerably smaller for the accelerating case, and is thought to be a result of the added body force on the fluid.

- Nearbody streamlines show a distinct variation in the flow field, indicating a potential for design changes that would not be otherwise sought after for steady flows

- This study focused on wake dynamics in an attempt to answer observed force and flow field differences.

9.2 DrivAer Acceleration

- This was a first attempt at a realistic road vehicle geometry, after vetting the process on the channel mounted square cylinder. There was a considerable increase in computational overhead in comparison and the simulation took several weeks to obtain 6 acceleration deceleration periods.

- Due to less than desired data sets, least-squares fitting of second order polynomials were applied to reduce noise from force data and improve predictive accuracy with less available data.

- During acceleration the drag force on the body increased 13.9% and during deceleration 13% and inertial drag coefficients of C_{MD}=2.0 and 2.02 respectively.

- During acceleration the lift force on the body increased 9.7% and during deceleration 5.9% and inertial lift coefficients of C_{ML} were found to be -0.54 and -0.3 respectively.

- An increase in the overall vorticity in the wake was present for the decelerating case along with an increase in rear glass separation.

9.3 DrivAer-GTR Acceleration

- As an attempt at investigating acceleration aerodynamics on a high performance vehicle which was created by the author for close ground proximity variations in lift force.

- During acceleration and deceleration the drag force varied by 10.0% and 9.0% respectively with inertial drag coefficient C_{MD} equal to 1.43 and 1.15.
- During acceleration and deceleration the lift force varies by a much smaller amount of 1% and 2.2% with inertial lift coefficient C_{ML} equal to 0.6 and 0.61.
- During acceleration and deceleration wing drag experienced the opposite trend in comparison to the body, losing drag and lift during acceleration and gaining drag during deceleration.
- A hypothetical straight line braking and accelerating simulation found that there would be a peak 16 horsepower loss of aerodynamic braking during deceleration and additional peak 6 horsepower of aerodynamic drag during acceleration.

9.4 Data Summary and Analysis

After analyzing each individual study in this dissertation, when the inertial coefficients are compiled in a single table (see Table 12 below) further analysis and conclusions can be drawn. Between the three geometries tested, we have a wide range of shapes and flow phenomenon present. The Square Cylinder is a simple bluff body with $C_L = 0$ and a large C_D value of 2.22 and virtually no attached flow beyond the front face. The DrivAer model on the other hand is somewhat streamlined, with a length nearly three times greater than height and width and majority of the wetted surface contains attached flow. Additionally the DrivAer model has a small C_D equal to approximately 0.240 with a body C_L of -0.047 which for all intensive purposes is

Table 12: Inertial drag coefficients (C_{MD}) for Square Cylinder, DrivAer and DrivAer-GTR.

a_x	Square Cylinder	DrivAer	DrivAer-GTR
$a_x > 0$	1.71	2.00	1.43
$a_x < 0$	1.91	2.02	1.15

nearly 0. Our third geometry, the DrivAer-GTR has nearly the same volume as the baseline DrivAer model but is lower to the ground plane and generates considerable drag and body down force with $C_D = 0.378$ and $C_L = -0.919$.

Even with the shape differences between the Square Cylinder and the DrivAer model, their inertial coefficients approach a value of 2, the same value determined by Morison for a circular cylinder. Yet, for the DrivAer-GTR, a geometry with considerable induced drag resulting from down force, the inertial coefficient is significantly smaller with an average value of 1.25. This indicates that there will be less of an effect from longitudinal vehicle acceleration on aerodynamic drag for a vehicle that generates more down force.

Additionally, while the application of the Morison equation to accelerating road vehicles has been an informative exercise, we must consider that its formulation was derived from the periodic wave equation as a function of time, originally only applicable to an inline force. Examples in this dissertation did however replicate the simulated force traces from calculated inertial coefficients with good agreement for both drag and lift. This replication should be verified with non periodic signals in the future beyond this dissertation.

9.5 Concluding Remarks

The simulations performed to simulate longitudinal acceleration of bluff bodies and road vehicles have demonstrated the impact on overall body forces and flow features. To answer the question from my dissertation proposal of: “is acceleration aerodynamics important for road vehicles?”, the short answer is yes. Sure, we have been creating and racing road vehicles for more than one hundred and twenty years with little to no investment in acceleration aerodynamics, but this does not mean that we would not have been better off looking in this area earlier. For ordinary road vehicles, the impact seems to only be applicable during rapid deceleration for collision avoidance, noting that the effect of acceleration aerodynamics reduces aerodynamic braking, requiring more work from the vehicle’s systems. However there may be design methods to abate these effects in the future if they are critical towards reducing injury from automobile collisions.

For high performance and motor sports vehicles, the inertial coefficient may be smaller for high down force vehicles, although the impacts of aerodynamic acceleration are even greater due to consistent exposure to large accelerations. In general, lap time records decrease with development and resources, indicating that acceleration rates will only increase into the future. With that said, the DrivAer-GTR study demonstrated that the rear wing experienced the inverse of expected behavior, indicating that the proximity of the wing to the body and resulting flow field variations due to acceleration could be critical for performance, potentially opening a new area for design improvements for performance vehicles.

Attempting to measure the impact of vehicle acceleration aerodynamics for this dissertation would have been nearly impossible without considerable funding to create a controlled test environment where large accelerations could occur, and certainly would not have been possible during an ordinary dissertation tenure, let alone the tenure of a full time working graduate student. Readily available computational fluid dynamics enabled this dissertation to take place, and the future of CFD technologies and advancement in computational power will only promote investigations to answer even harder and more complex questions. Longitudinal acceleration and deceleration of road vehicles is only two degrees of acceleration freedom, of which there are 6 translational, 6 rotational and 9 which represent the relationship between translation and rotation, 21 in all [67], only after obtaining inertial coefficients for all of these components will there be a complete picture towards road vehicle acceleration aerodynamics.

REFERENCES

[1] S. Ahmed, G. Ramm, et al. Some salient features of the time-averaged ground vehicle wake. *SAE*, 1984.

[2] P. Aschwanden, J. Müller, and U. Knörnschild. Experimental study on the influence of model motion on the aerodynamic performance of a race car. Technical report, SAE Technical Paper, 2006.

[3] P. Aschwanden, J. Müller, G. C. Travaglio, and T. Schöning. The influence of motion aerodynamics on the simulation of vehicle dynamics. *SAE International Journal of Passenger Cars-Mechanical Systems*, 1(2008-01-0657):545–551, 2008.

[4] N. Ashton, A. West, et al. Assessment of rans and des methods for realistic automotive models. *Computers and Fluids*, 2016.

[5] G. K. Batchelor. *An introduction to fluid dynamics.* Cambridge university press, 2000.

[6] P. Bearman and E. Obasaju. A study of forces, circulation and vortex patterns around a circular-cylinder in oscillating flow. *Journal of Fluid Mechanics*, 119:297–321, 1988.

[7] M. S. Bloor. The transition to turbulence in the wake of a circular cylinder. *Journal of Fluid Mechanics*, 19(2):290304, 1964.

[8] J. Boussinesq. Théorie de lécoulement tourbillant. *Mem. Présentés par Divers Savants Acad. Sci. Inst. Fr*, 23(46-50):6–5, 1877.

[9] P. L. G. D. Buat. *Principles D'hydraulique.* F. Didot, Paris, 1786.

[10] B. Cantwell and D. Coles. An experimental study of entrainment and transport in the turbulent near wake of a circular cylinder. *Journal of Fluid Mechanics*, 136:321–374, Nov. 1983.

[11] Y. Cao and T. Tamura. Large-eddy simulations of flow past a square cylinder using structured and unstructured grids. *Computers & Fluids*, 137:36–54, 2016.

[12] I. Celik, M. Klein, M. Freitag, and J. Janicka. Assessment measures for URANS/DES/LES: an overview with applications. *Journal of Turbulence*, (7):N48, 2006.

[13] A. Cogotti. Ground effect of a simplified car model in side-wind and turbulent flow. Technical report, SAE Technical Paper, 1999.

[14] C. Collin, S. Mack, T. Indinger, and J. Mueller. A numerical and experimental evaluation of open jet wind tunnel interferences using the drivaer reference model. *SAE International Journal of Passenger Cars-Mechanical Systems*, 9(2016-01-1597):657–679, 2016.

[15] S. A. Fackrell. *Study of the Added Mass of Cylinders and Spheres*. PhD dissertation, University of Windsor, 2011.

[16] J. N. Fernando, M. Marzanek, C. Bond, and D. E. Rival. On the separation mechanics of accelerating spheres. *Physics of Fluids*, 29(3), 2017.

[17] D. C. Forbes, G. J. Page, et al. A fully coupled, 6 degree-of freedom, aerodynamic and vehicle handling crosswind simulation using the drivaer model. *SAE Int. J. Passeng. Cars*, 2016.

[18] J. Fröhlich, C. P. Mellen, W. Rodi, L. Temmerman, and M. A. Leschziner. Highly resolved large-eddy simulation of separated flow in a channel with streamwise periodic constrictions. *Journal of Fluid Mechanics*, 526:19–66, 2005.

[19] S. Gant. Quality and reliability issues with large-eddy simulation. report rr656. *Health and Safety Executive, UK*, 2008.

[20] J. H. Gerrard. The mechanics of the formation region of vortices behind bluff bodies. *Journal of Fluid Mechanics*, 25(2):401413, 1966.

[21] O. M. Griffin and S. E. Ramberg. The vortex-street wakes of vibrating cylinders. *Journal of Fluid Mechanics*, 66(3):553576, 1974.

[22] M. S. Gritskevich, A. V. Garbaruk, J. Schütze, and F. R. Menter. Development of DDES and IDDES formulations for the k-ω shear stress transport model. *Flow, turbulence and combustion*, 88(3):431–449, 2012.

[23] W. Haase, M. Braza, and A. Revell. *DESider–A European Effort on Hybrid RANS-LES Modelling: Results of the European-Union Funded Project, 2004-2007*, volume 103. Springer Science & Business Media, 2009.

[24] Y. Han, G. Ding, Y. He, J. Wu, and J. Le. Assessment of the IDDES method acting as wall-modeled LES in the simulation of spatially developing supersonic flat plate boundary layers. *Engineering Applications of Computational Fluid Mechanics*, 12(1):89–103, 2017.

[25] A. I. Heft, T. Indinger, and N. A. Adams. Introduction of a new realistic generic car model for aerodynamic investigations. *SAE*, 2012.

[26] N. Jarrin, S. Benhamadouche, D. Laurence, and R. Prosser. A synthetic-eddy-method for generating inflow conditions for large-eddy simulations. *International Journal of Heat and Fluid Flow*, 27:585–593, 2006.

[27] W. Jones and B. Launder. The prediction of laminarization with a two-equation model of turbulence. *International journal of heat and mass transfer*, 15(2):301–314, 1972.

[28] N. Joukowsky. Über die konturen der tragflächen der drachenflieger. *Zeit. für Flugtechnik und Motorluftschiffahrt*, 1:281–284, 1910.

[29] N. Kohei, T. Makoto, et al. Numerical analysis of unsteady aerodynamics of formula car during dynamic cornering motion. In *32nd AIAA Applied Aerodynamics Conference*. AIAA Aviation, June 2014.

[30] A. N. Kolmogorov. Equations of turbulent motion in an incompressible fluid. In *Dokl. Akad. Nauk SSSR*, volume 30, pages 299–303, 1941.

[31] E. Konstantinidis and S. Balabani. Flow structure in the locked-on wake of a circular cylinder in pulsating flow: Effect of forcing amplitude. *International Journal of Heat and Fluid Flow*, 29(6):1567–1576, 2008.

[32] E. Konstantinidis, S. Balabani, and M. Yianneskis. The effect of flow perturbations on the near wake characteristics of a circular cylinder. *Journal of Fluids and Structures*, 18(3):367–386, 2003.

[33] E. Konstantinidis and D. Bouris. Effect of nonharmonic forcing on bluff-body vortex dynamics. *Physical Review E*, 79(4):045303, 2009.

[34] E. Konstantinidis and D. Bouris. Vortex synchronization in the cylinder wake due to harmonic and non-harmonic perturbations. *Journal of Fluid Mechanics*, 804:248–277, 2016.

[35] E. Konstantinidis and C. Liang. Dynamic response of a turbulent cylinder wake to sinusoidal inflow perturbations across the vortex lock-on range. *Physics of Fluids*, 23(7):075102, 2011.

[36] A. Kuczaj, E. Komen, and M. Loginov. Large-Eddy Simulation study of turbulent mixing in a t-junction. *Nuclear Engineering and Design*, 240(9):2116–2122, 2010.

[37] B. Lee. Some effects of turbulence scale on the mean forces on a bluff body. *Journal of Wind Engineering and Industrial Aerodynamics*, 1:361 – 370, 1975.

[38] Y. Lee, J. Rho, K. H. Kim, and D.-H. Lee. Fundamental studies on free stream acceleration effects on drag force in bluff bodies. *Journal of Mechanical Science and Technology*, 25:695–701, 2011.

[39] D. Lilly. The representation of small-scale turbulence in numerical simulation experiments proceedings of the ibm scientific computing symposium on environmental sciences. *Yorktown Heights, NY*, 1967.

[40] D. A. Lyn, S. Einav, W. Rodi, and J. H. Park. A laser-doppler velocimetry study of the ensemble-averaged characteristics of the turbulent near wake of a square cylinder. *Journal of Fluid Mechanics*, 304:285–319, 1995.

[41] D. A. Lyn and W. Rodi. The flapping shear layer formed by flow separation from the forward corner of a square cylinder. *Journal of Fluid Mechanics*, 267:353–376, 1994.

[42] F. Menter. Two-equation eddy-viscosity modeling for engineering applications. *AIAA Journal*, 32(8):1598–1605, 1994.

[43] F. Menter and M. Kuntz. Adaptation of eddy-viscosity turbulence models to unsteady separated flow behind vehicles. In *The aerodynamics of heavy vehicles: trucks, buses, and trains*, pages 339–352. Springer, 2004.

[44] J. Mohrfeld-Halterman and M. Uddin. High fidelity quasi steady-state aerodynamic model effects on race vehicle performance predictions using multi-body simulation. *Vehicle System Dynamics*, 54(7):963–981, 2016.

[45] J. Morison. The force distribution exerted by surface waves on piles. Technical report, California Univ Berkeley Wave Research Lab, 1953.

[46] B. Morton. The generation and decay of vorticity. *Geophysical & Astrophysical Fluid Dynamics*, 28(3-4):277–308, 1984.

[47] H. Nishimura. *Fundamental study of bluff body aerodynamics.* PhD dissertation, Kyoto University, 2001.

[48] R. L. Panton. *Incompressible Flow.* John Wiley and Sons Inc., Hoboken NJ, third edition, 2005.

[49] S. B. Pope. *Turbulent Flows.* Cambridge University Press, New York, first edition, 2000.

[50] L. Prandtl and K. Wieghardt. *Über ein neues Formelsystem für die ausgebildete Turbulenz.* Vandenhoeck & Ruprecht, 1947.

[51] W. Rodi. Comparison of les and rans calculations of the flow around bluff bodies. *Journal of wind engineering and industrial aerodynamics*, 69:55–75, 1997.

[52] W. Rodi, J. H. Ferziger, M. Breuer, and M. Pourquie. Status of large eddy simulation: Results of a workshop. *Journal of Fluids Engineering, Transactions of the ASME*, 119:248–262, 1997.

[53] H. Roohani. *Aerodynamic effects of accelerating object in air.* PhD dissertation, University of the Witwatersand, Johannesburg, 2010.

[54] A. Savitzky and M. Golay. Smoothing and differentiation of data by simplified least squares procedures. *Analytical Chemistry*, 36(8):1627–1639, 1964.

[55] M. Shur, P. Spalart, and A. Travin. A hybrid rans-les approach with delayed-des and wall-modelled les capabilities. *International Journal of Heat and Fluid Flow*, 29(6):1638–1649, 2008.

[56] J. Smagorinsky. General circulation experiments with the primitive equations: I. the basic experiment. *Monthly weather review*, 91(3):99–164, 1963.

[57] R. F. Soares, A. Knowles, S. G. Olives, K. Garry, and J. Holt. On the aerodynamics of an enclosed-wheel racing car: an assessment and proposal of add-on devices for a fourth, high-performance configuration of the drivaer model. Technical report, SAE Technical Paper, 2018.

[58] A. Sohankar, L. Davidson, and C. Norberg. Large eddy simulation of flow past a square cylinder: comparison of different subgrid scale models. *Journal of Fluids Engineering*, 122(1):39–47, 2000.

[59] P. Spalart and S. Allmaras. A one-equation turbulence model for aerodynamic flows. In *30th aerospace sciences meeting and exhibit*, page 439, 1992.

[60] P. R. Spalart. Comments on the feasibility of les for wings, and on hybrid rans/les approach. In *Proceedings of First AFOSR International Conference on DNS/LES, 1997*, 1997.

[61] P. R. Spalart, S. Deck, M. L. Shur, K. D. Squires, M. K. Strelets, and A. Travin. A new version of detached-eddy simulation, resistant to ambiguous grid densities. *Theoretical and computational fluid dynamics*, 20(3):181, 2006.

[62] G. G. Stokes. On the effect of the internal friction of fluids on the motion of pendulums. *Transactions of the Cambridge Philosophical Society*, 9, 1850.

[63] H. Tennekes and J. L. Lumley. *A First Course in Turbulence.* MIT Press, Cambridge, MA, 1994.

[64] F. X. Trias, A. Gorobets, and A. Olivia. Turbulent flow around a square cylinder at reynolds number 22000: a dns study. *Computers and Fluids*, 123, 2015.

[65] D. C. Wilcox. *Turbulence Modeling for CFD.* DCW Industries Inc., La Canada, California, third edition, 2006.

[66] J. Wong, A. Mohebbian, J. Kriegseis, and D. Rival. Rapid flow separation for transient inflow conditions versus accelerating bodies: An investigation into their equivalency. *Journal of Fluids and Structures*, 40:257–268, 2013.

[67] C.-S. Yih. *Fluid Mechanics.* West River Press, Ann Arbor, Michigan, 1977.

[68] Q. Zhang and H. Johari. Effects of acceleration on turbulent jets. *Physics of Fluids*, 8(8):2185–2195, 1996.

APPENDIX A: ADDITIONAL PLOTS

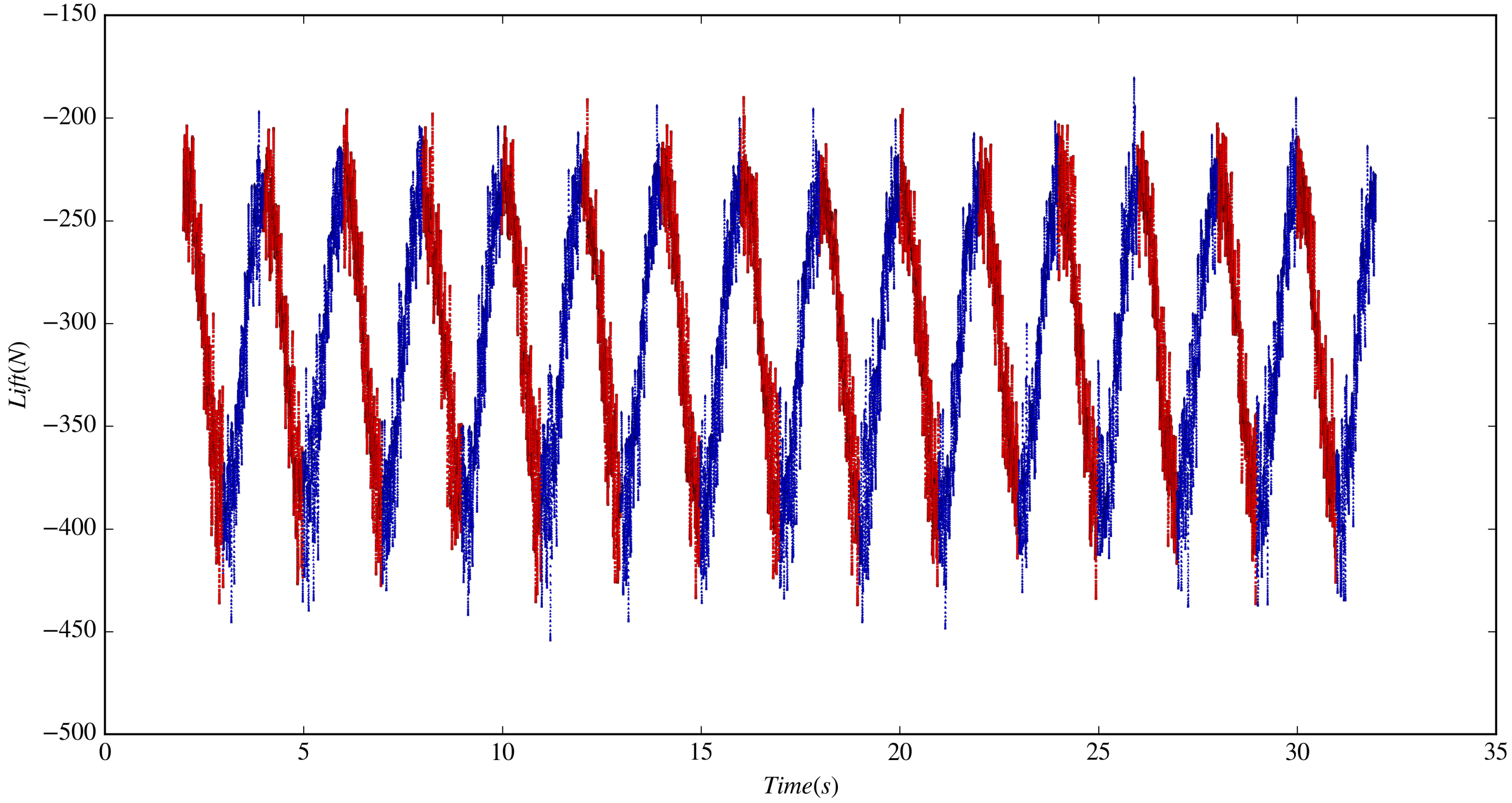

Figure 78: The DrivAer-GTR lift force (N) versus time (s).

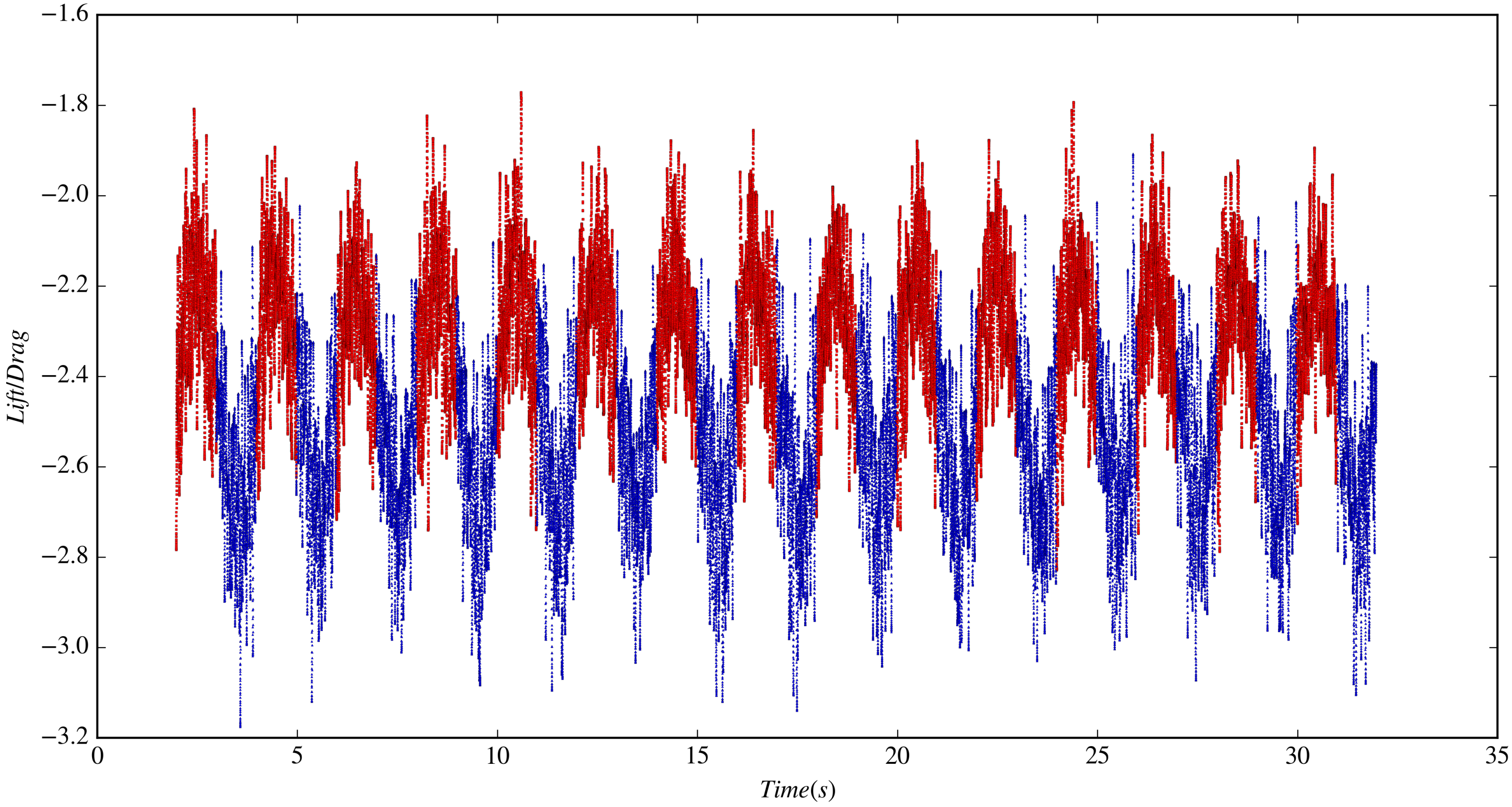

Figure 79: The DrivAer-GTR efficiency (lift/drag) versus time (s).

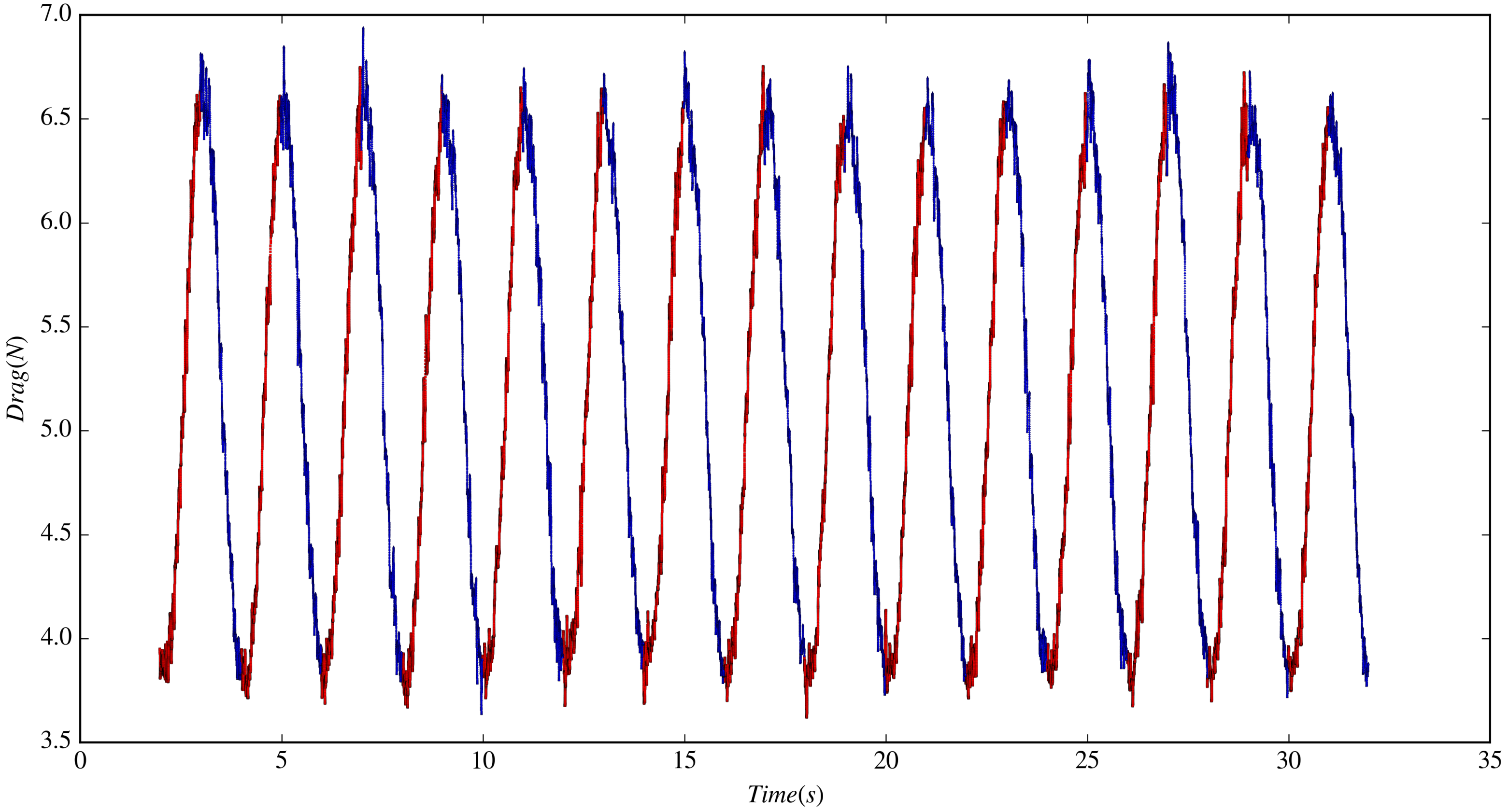

Figure 80: The DrivAer-GTR wing drag force (N) versus time (s).

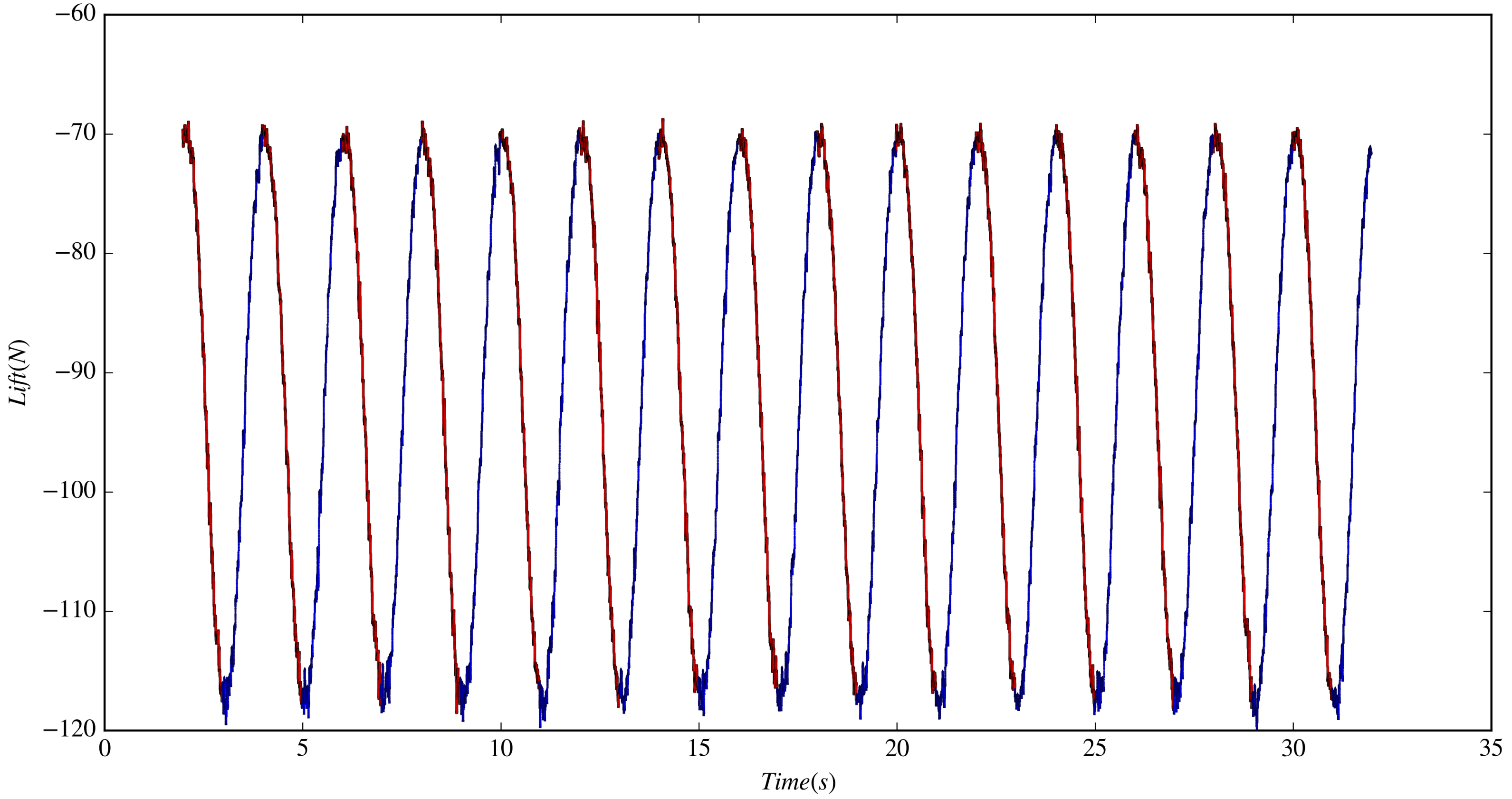

Figure 81: The DrivAer-GTR wing lift force (N) versus time (s).

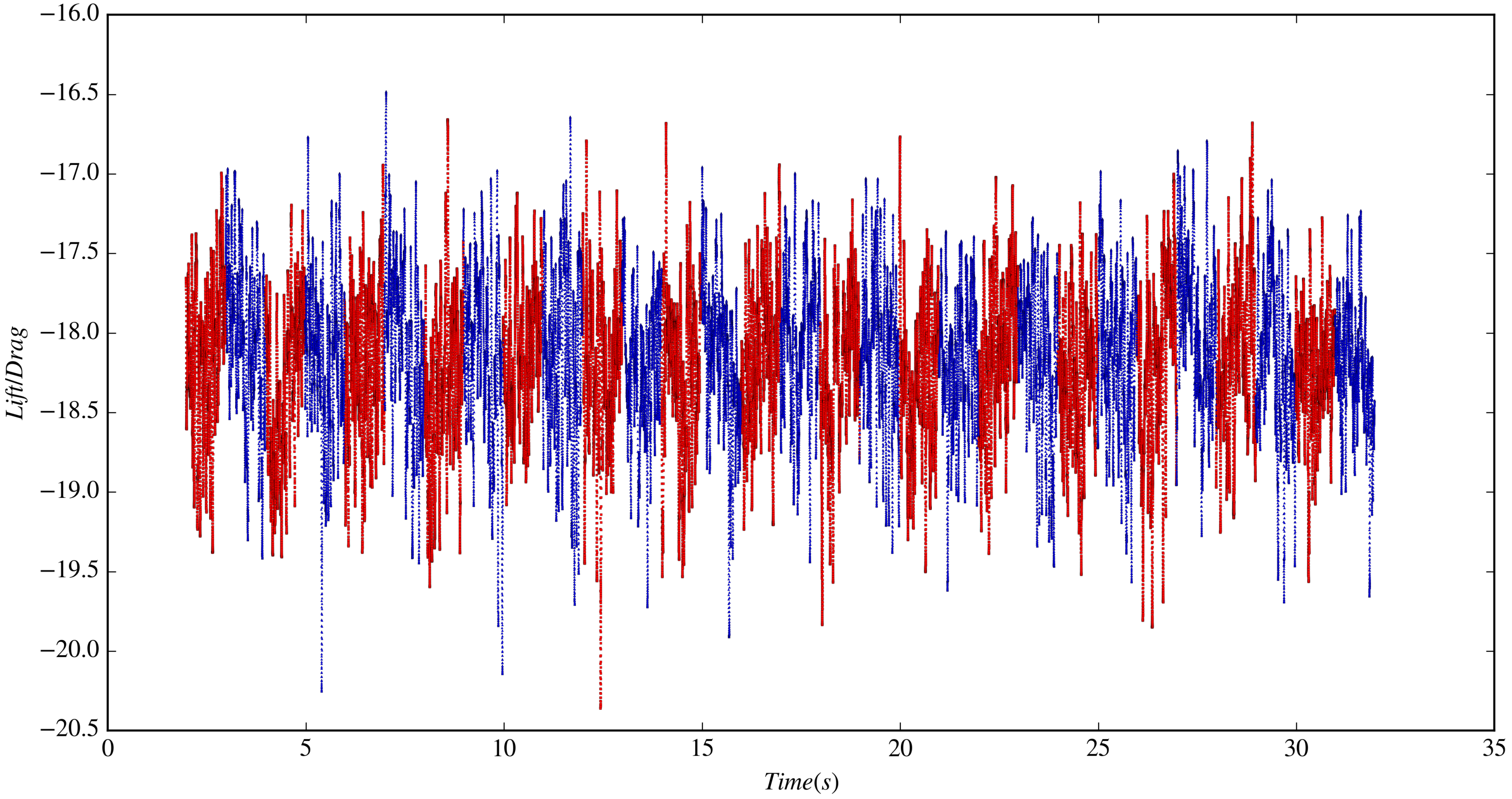

Figure 82: The DrivAer-GTR wing efficiency (lift/drag) versus time (s).

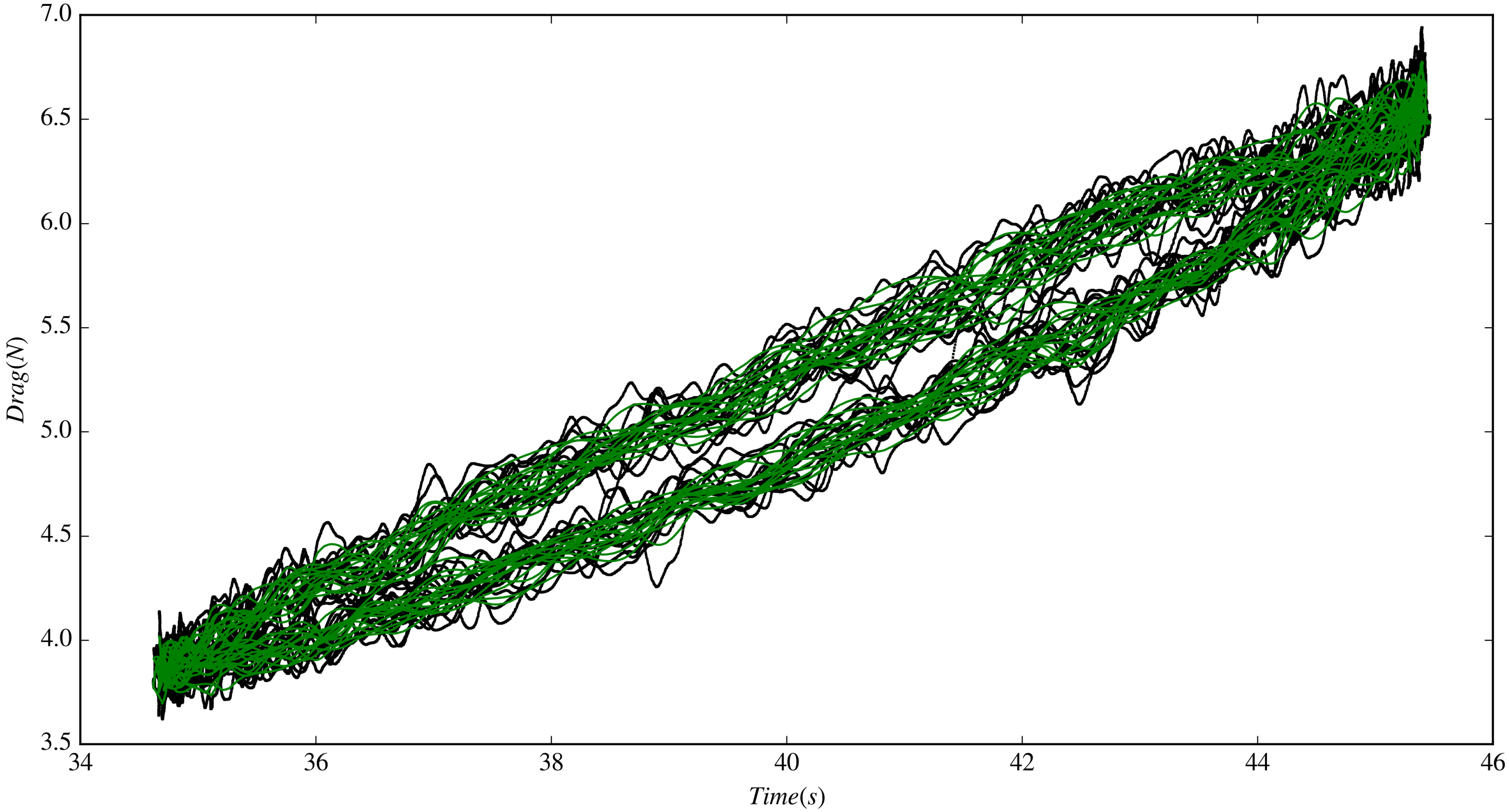

Figure 83: The DrivAer-GTR Wing drag (N) signal with low-pass filtering with raw signal versus velocity (m/s).

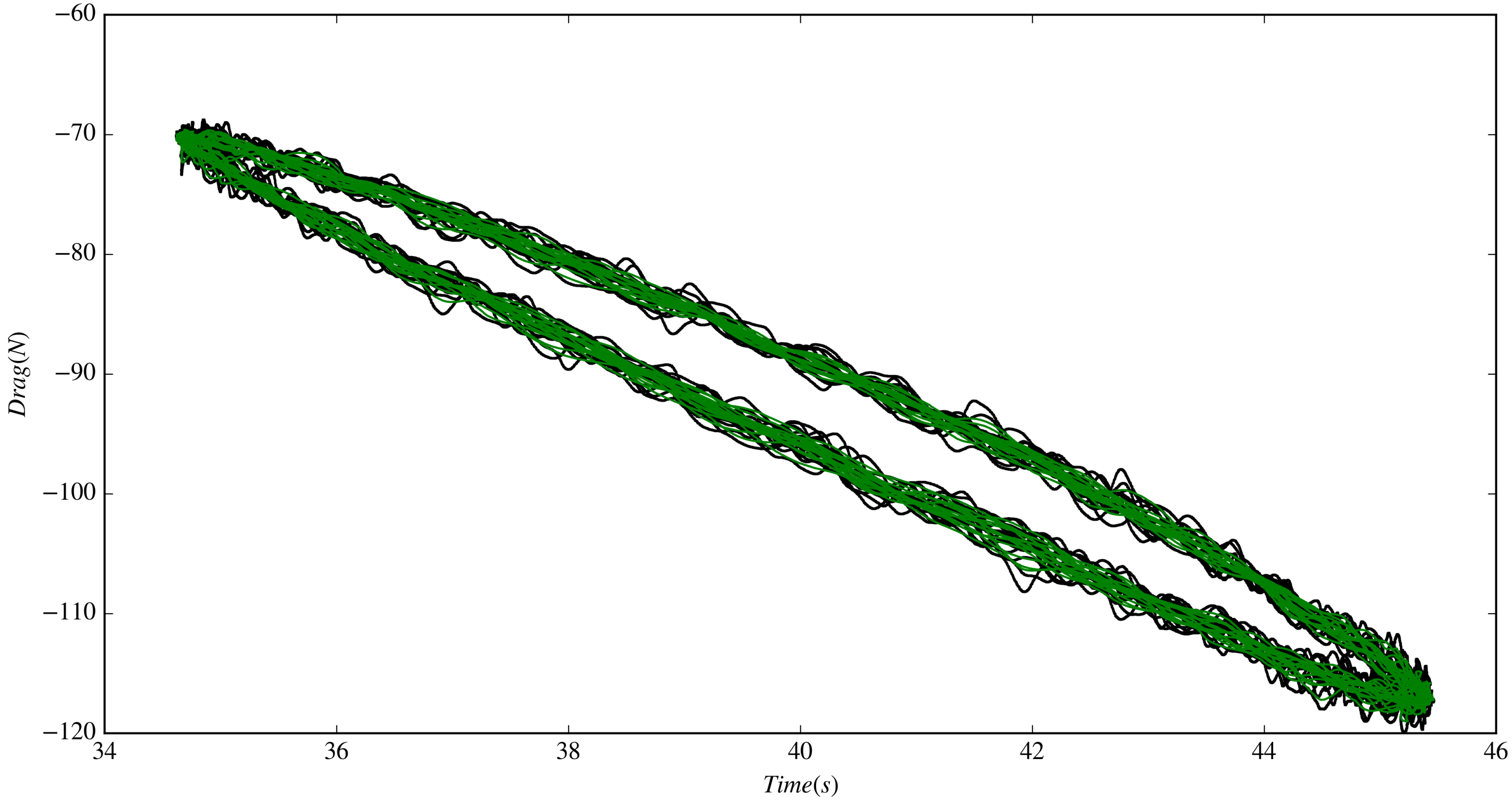

Figure 84: The DrivAer-GTR Wing lift (N) signal with low-pass filtering with raw signal versus velocity (m/s).

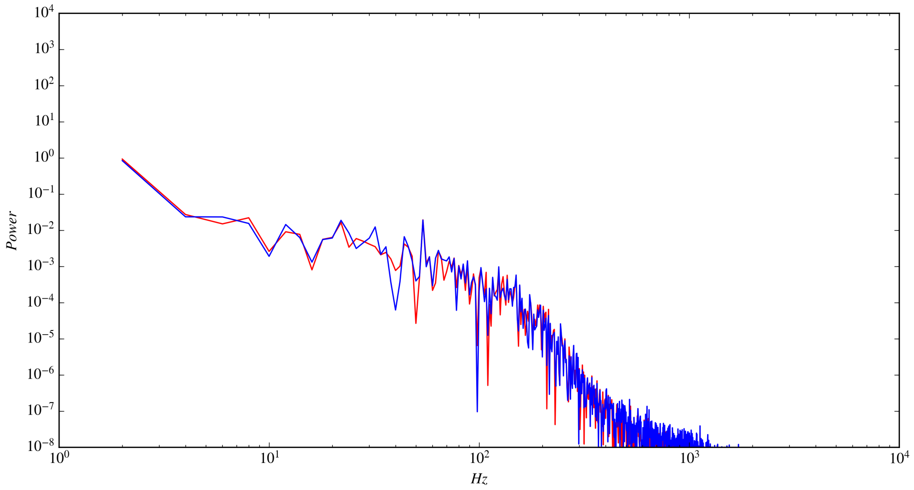

Figure 85: Fast Fourier Transform power spectrum of DrivAer-GTR Wing Drag (N).